A numerical investigation of the crashworthiness of a composite glider cockpit

JJ Pottas

20098270

Dissertation submitted in fulfilment of the requirements for the degree *Magister* in Mechanical Engineering at the Potchefstroom Campus of the North-West University

Supervisor: Dr AS Jonker

April 2015

To Carmin. My beautiful, innocent, adventurous companion and to our newborn son, my namesake.

Preface

This research project was completed with the valued support of several people. I am grateful for their commitment to the study and would like to express my sincere appreciation to them. I thank Dr Attie Jonker, the School of Mechanical Engineering and Jonker Sailplanes who allowed me the opportunity to conduct research on the JS1 - an engineering masterpiece. I am humbled to have been able to study this iconic aircraft, which has earned its place in the history books. My gratitude also extends to Andrew Berndt and Paul Naude, who frequently but patiently provided modelling advice and software support for MSC SimXpert, MSC Nastran and LS-Dyna. I also thank Jaco Loubser for his valuable contribution in reviewing the dissertation. Finally, I wish to express my thanks to Christien Terblanche for language editing the final version of the document.

Abstract

Finite element analysis with explicit time integration is widely used in commercial crash solvers to accurately simulate transient structural problems involving large-deformation and nonlinearity. Technological advances in computer software and hardware have expanded the boundaries of computational expense, allowing designers to analyse increasingly complex structures on desktop computers. This dissertation is a review of the use of finite element analysis for crash simulation, the principles of crashworthy design and a practical application of these methods and principles in the development of a concept energy absorber for a sailplane. Explicit nonlinear finite element analysis was used to do crash simulations of the glass, carbon and aramid fibre cockpit during the development of concept absorbers. The SOL700 solution sequence in MSC Nastran, which invokes the LS-Dyna solver for structural solution, was used. Single finite elements with Hughes-Liu shell formulation were loaded to failure in pure tension and compression and validated against material properties. Further, a simple composite crash box in a mass drop experiment was simulated and compared to experimental results. FEA was used for various crash simulations of the JS1 sailplane cockpit to determine its crashworthiness. Then, variants of a concept energy absorber with cellular aluminium sandwich construction were simulated. Two more variants constructed only of fibre-laminate materials were modelled for comparison. Energy absorption and specific energy absorption were analysed over the first 515 mm of crushing. Simulation results indicate that the existing JS1 cockpit is able to absorb energy through progressive crushing of the frontal structure without collapse of the main cockpit volume. Simulated energy absorption over the first 515 mm was improved from 2232 J for the existing structure, to 9 363 J by the addition of an energy absorber. Specific energy absorption during the simulation was increased from 1063 J/kg to 2035 J/kg.

Keywords:

Composite; Crash simulation; Crashworthiness; Energy absorption; Explicit; Finite element analysis; Honeycomb

Nomenclature

ABID	bidirectional aramid fibre
a_n	vector of nodal accelerations
A_s	area of a finite element
AUD	unidirectional aramid fibre
C	damping matrix
c	speed of sound
CBID	bidirectional carbon fibre
CFL	Courant-Friederichs-Lewy (criterion)
CFRP	carbon fibre reinforced plastic
CG	centre of gravity
CPU	central processing unit
CUD	unidirectional carbon fibre
D_i	length of the diagonal of a finite element
d_n	vector of nodal displacements
E	modulus of elasticity
EASA	European Aviation Safety Agency
FEA	finite element analysis
FE	finite element
F_n	vector of loads
FRP	fibre reinforced plastic
G	shear modulus
g	gravitational acceleration
GBID	bidirectional glass fibre
GMT	glass mat reinforced thermoplastic
GUD	unidirectional glass fibre
GUI	graphical user interface
K	stiffness matrix
L_i	length of a side of a finite element

L_s	characteristic length of an element
LSTC	Livermore Software Technology Corporation
M	mass matrix
m	mass
MKF	multi-layered knitted fabric
P	crash load
PMI	polymethacrylimide
PVC	polyvinyl chloride
S	displacement
SEA	specific energy absorption
SOL700	MSC Nastran explicit nonlinear solver
SSEA	system-specific energy absorption
UHMWPE	ultra high molecular weight polyethylene
v	Poisson's ratio
v_n	vector of nodal velocities
W	energy absorption
W_v	energy absorption per unit volume
α	weighting factor for the shear stress term
Δt	minimum time step of any finite element in a mesh
ε	strain
ρ	density
σ	stress
τ	shear stress
ω	eigenfrequency of a finite element mesh

Table of Contents

List of Tables

List of Figures

Chapter 1 Introduction

1.1 Background

The 2012 Annual Safety Report published by the Soaring Safety Foundation shows that an average of 30.6 gliding accidents occurred per year in the United States from 2008 to 2012. Of these accidents, 1 in 5 were fatal (SSF, 2013:11-12), while the number of active glider pilots stayed virtually unchanged (FAA, 2013). These safety statistics serve as justification for glider crash research in two ways. Firstly, by showing that gliding remains an inherently dangerous and potentially fatal activity. Secondly, perhaps more importantly, it suggests that the vast majority of glider accidents are survivable.

While crash avoidance should remain the primary focus of aircraft safety, design for crashworthiness has become increasingly important. The basic principles of crashworthy design are to maintain a safe volume around the occupants during a crash (EASA, 2009:5) and to limit the acceleration forces transmitted to the occupants (Peng *et al.*, 2011:286).

Costly physical crash tests have historically been used to investigate the crashworthiness of aircraft during the design and certification processes. Such tests are now increasingly being replaced or supplemented by finite element simulations (Blaurock *et al.*, 2013:406). Several sources (Blaurock *et al.*, 2013:406; Fasanella, 2006:1; FAA, 2003:5) suggest that aircraft regulations are also evolving towards including simulation in the certification process.

The subject of this study is the JS1 sailplane manufactured by Jonker Sailplanes. The design of its glass, aramid and carbon fibre-reinforced structure was done with extensive use of linear static finite element analysis (FEA) (Jonker, 2012). Its structural integrity under static load is therefore well understood, but it has yet to be analysed for dynamic crash response.

This research forms part of a broader project by Jonker Sailplanes to type-certify the JS1 in terms of EASA CS-22, the European Certification Specification for Sailplanes. The JS1, shown in *Figure 1*, conforms to the typical layout used in single-seat, high performance sailplanes. The pilot is positioned near the front of the fuselage and the rudder pedals are located in the nose of the aircraft. This layout is unfavourable to crashworthy design due to the limited volume and structure in front of the cockpit that can be used for energy absorption.

Figure 1: **Photograph of the JS1 sailplane showing the forward position of the cockpit.**

However, similar constraints have not prevented Formula One® from achieving vast improvements in crash safety. The rate of death or serious injury per number of crashes has changed from 1 in 8 in the 1960's to 1 in 250 during the 1980's (Savage, 2010:117). In their industry, space is also highly limited. The occupant is in a vulnerable location near the point of impact, lightweight composite materials make up the majority of the structure and vehicles are prone to high speed frontal impact. These limitations have largely been overcome thanks to the use of advanced materials such as carbon fibre composites and design aids like FEA.

In particular, improvements in the efficiency of finite element solvers and increased computational power of personal computers have revolutionised structural design. Analysts who previously would have required access to purpose-built computers can now viably analyse advanced models on their desktop computers. This study will explore the application of finite element analysis in the process to enhance the crashworthiness of a sailplane structure.

1.2 Problem Definition

The cockpit of the JS1 sailplane should protect its occupant from serious injury in the event of a crash. However, its structural integrity under dynamic crash loading has not been studied. Research into the crashworthiness of the current cockpit and ways to potentially improve the crash survivability of an occupant is therefore necessary.

1.3 Objectives

The objectives of the study include the following:

- determining numerically the crash behaviour of the JS1 with loading direction as specified in CS-22.561(b)(2);
- using the obtained data to determine the crashworthiness of the cockpit;
- implementing concept structural improvements based on the initial results;
- determining the crash behaviour of concept structures under the same conditions as the initial test; and
- using the obtained data of the concept structures to determine their comparative crashworthiness.

1.4 Layout

Chapter 2 begins with a review of the principles of crashworthy design. It also presents the details of other relevant research done in the field of crash simulation of composite structures. Next, *Chapter 3* provides insight into the numerical methods used in explicit nonlinear solvers. This knowledge is prerequisite to subsequent parts of the document. *Chapter 4* is dedicated to the development of the finite element models used to produce the results given in *Chapters 5* and *6*. The main part of the dissertation closes, in *Chapter 7,* with a summary of significant findings, conclusions and a discussion of potential future work. This chapter is followed by the list of referenced sources and the appendices which provide details of the research methodology and energy absorber design.

Chapter 2 Literature Study

The following is a review of several relevant studies undertaken in the fields of crashworthiness and crash simulation. The discussion aims to identify pertinent methodologies from other research that are applicable to the objectives of this study. It further sets out to explain the role of simulation in the field of crashworthiness of composite structures.

Section 2.1 begins with an introduction to the principles of crashworthy design. These principles were used initially to determine the crash performance of the existing JS1 structure, and again when structural enhancements were considered. *Section 2.2* is focused on the methods used to develop accurate finite element crash models, which were applied during simulation. Important themes in this section are accurate modelling of composite material behaviour under crash conditions, simulation of dominant failure mechanisms and modelling of dynamic contact.

Section 2.3 considers methods that can be used to ensure the accuracy of crash models in the absence of experimental data. In the case of the JS1, it is not feasible to carry out full-scale physical crash testing and alternative methods had to be used to ensure the fidelity of the numerical model. Lastly, *Section 2.4* contains information about processing results into interpretable data and quantification of crash performance.

2.1 Crashworthy Design

In the design of a crashworthy structure, there are multiple objectives that must be considered simultaneously. According to Abramowicz (2003:92), the occupied volume must remain reasonably undeformed to create a safe capsule for the occupant. Secondly, the surrounding structure must dissipate kinetic energy through progressive deformation so as not to transfer intolerable acceleration loads to the occupants. Furthermore, some structures must fulfil both these roles (Abramowicz, 2003:92).

2.1.1 Maintaining a Safe Occupant Volume

The safety specification for gliders, EASA CS-22, stipulates that the cockpit should constitute a “safety cell” in crash conditions (EASA, 2009: 2-C-6). Röger (2007:2) describes this as a cockpit that does not collapse in an emergency landing and remains a strong cage. The strong cage should extend from the front rudder pedals to the rearmost headrest. Röger further adds that a strong cage design should always be combined with energy absorbing elements that limit the acceleration of the occupant’s body to survivable levels. Energy absorbers are discussed in detail in *Section 2.1.2*.

Segal (1998:13) highlights several structural characteristics of an experimental crashworthy cockpit design that performed exceptionally well in a physical crash test. Similar to Röger's concept, this design features an energy absorbing nose and rigid reinforcements around the occupant. The cage extends rearwards from the forward bulkhead and features a roll bar to protect the pilot if the glider is inverted during a crash. Upper and lower spars are positioned longitudinally along the sides of the cockpit, while a crossbeam and central bulkhead contribute to transverse stiffness. The features of Segal's reinforced cockpit design are shown in *Figure 2* below.

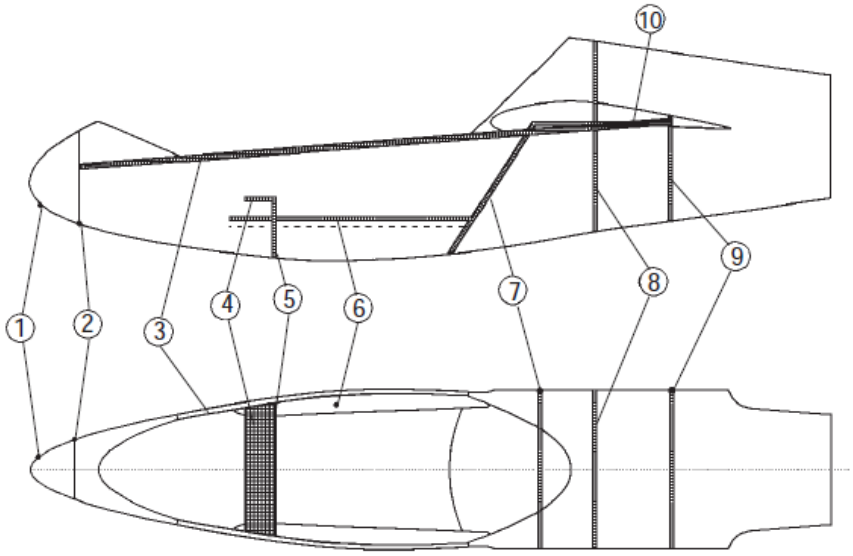

1 *Nose cone*
2 *Forward bulkhead*
3 *Upper spars*
4 *Crossbeam*
5 *Bulkhead*
6 *Lower spars/seat pan support*
7 *Front wing mounting bulkhead*
8 *Roll bar*
9 *Rear wing mounting bulkhead*
10 *Top of undercarriage box*

Figure 2: Reinforced Cockpit Design (Segal, 1998:13)

In Formula One®, the safe volume is called the survival cell and is defined as a continuous closed structure containing the fuel tank and cockpit (FIA, 2013:6). The dimensions for the survival cell are specified to reduce the risk of injury to the driver in a crash and are shown in *Figure 3*.

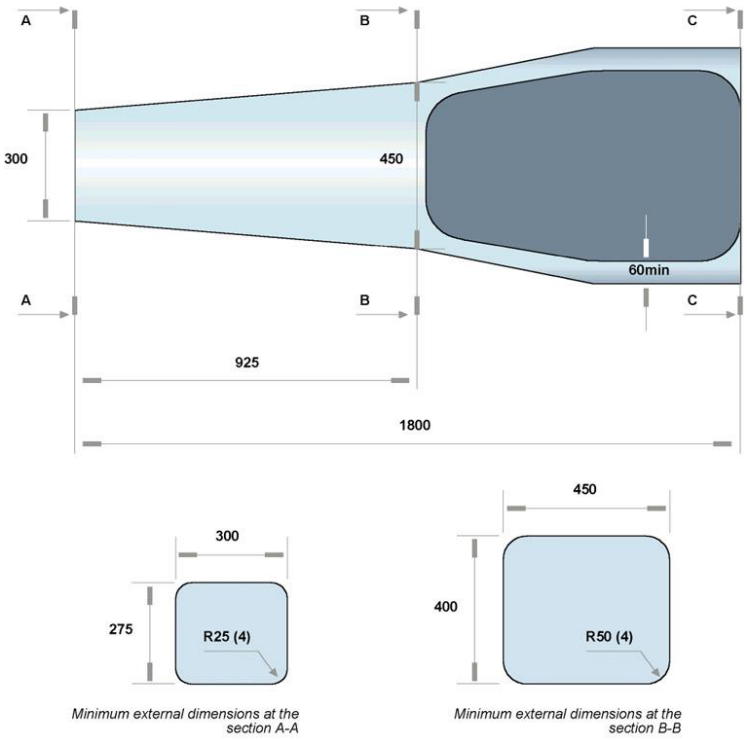

Figure 3: Formula One® Survival Cell Dimensions (FIA, 2013:76)

According to the 2013 Formula One® Technical Regulations, loads of up to 40kN, when applied to specified parts of the structure, may not result in permanent deflection of more than 1 mm (FIA, 2013:64-65). At the front and sides of this structure, separate energy absorbers must be fitted, which are discussed in further detail in *Section 2.1.2*.

2.1.2 Energy Absorbing Structures

Alghamdi (2001:190) defines an energy absorber as “a system that converts, totally or partially, kinetic energy into another form of energy”. In aircraft design such systems are used to limit the acceleration imparted to occupants during impact.

According to Heimbs (2012:3), absorbed energy in any compressive or tensile test of a material or structure, is represented by the area under the force displacement curve. The weight-specific form of this characteristic, known as specific energy absorption (*SEA*) and measured in KJ/kg, is commonly used to compare the performance of energy absorbers in weight-sensitive applications. In order to obtain the largest area under the curve, an ideal energy absorber should exhibit a plateau shaped force displacement curve, which is rarely encountered in real absorbers. In contrast, they tend to show initial load peaks and erratic time histories. One aim of absorber design should be to minimise these oscillations (Heimbs, 2012:3).

Heimbs (2012:3) also comments on the multi-functional role of energy absorbing structures in aircraft. Apart from being able to withstand a specific load case, these structures have to be extremely lightweight, inexpensive, fatigue resistant and maintainable. He further goes on to say that energy absorbing structures in aircraft can be broadly classed into two categories. The first category absorbs energy through ductile deformation of existing aircraft structures, and the second absorbs energy through separate elements whose only function is energy absorption in a crash (Heimbs, 2012:3).

As an example of a multi-functional energy absorber, the 2013 Formula One® technical regulations stipulate that cars must be fitted with a frontal energy absorber with a minimum cross section of 9000 mm^2, at a point not further than 50 mm from its front (FIA, 2013:55). This absorber also fulfils a role as an aerodynamic component. Separate energy absorbers must also be installed on either side of the survival cell to protect the driver in a lateral impact (FIA, 2013:57).

Strict testing of the construction materials (FIA, 2013: 56) and vehicle structure are required for compliance. Tests include frontal, side, rear and steering column impacts, roll-over testing and several static load tests (FIA, 2013:59-66). During frontal impact tests at a velocity of 15m/s, the following criteria must be satisfied (FIA, 2013:59):

- The peak deceleration over the first 150 mm of deformation should not exceed 10g.
- The peak deceleration over the first 60kJ energy absorption should not exceed 20g.
- The average deceleration should not exceed 40g.
- The peak deceleration in the chest of the dummy should not exceed 60g for more than a cumulative 3ms, this being the resultant of data from three axes.

Or

- The peak force over the first 150 mm of deformation should not exceed 75kN.
- The peak force over the first 60kJ energy absorption should not exceed 150kN.
- The average deceleration should not exceed 40g.
- The peak deceleration in the chest of the dummy should not exceed 60g for more than a cumulative 3ms, this being the resultant of data from three axes.

2.1.2.1 Materials for energy absorption

Heimbs (2012:3) summarises the materials commonly used in aircraft energy absorbing systems, either singly or in combination, into the following three groups:

- Metals such as aluminium, titanium and steel that absorb energy by plastic deformation.
- Fibre-reinforced composites such as carbon fibre-reinforced plastics (CFRP), which absorb energy through matrix cracking, delamination, fibre fracture and fragmentation.
- High-performance synthetic fibres such as UHMWPE (Dyneema or Spectra), which have specific strengths up to 15 times that of steel. These can be applied in dry or resin-impregnated form.

The author further explains that cellular structures made of these materials are often used for their low weight and near-ideal absorption due to near-constant crushing load. The following are examples of cellular energy absorbers:

Honeycomb

Hexagonal honeycomb structures made of Nomex, aluminium or thermoplastics are the state-of-the-art cellular energy absorbers. *Figure 4* below shows a stress-strain curve for a Nomex honeycomb structure and the comparative specific energy absorption characteristics of various honeycomb structures.

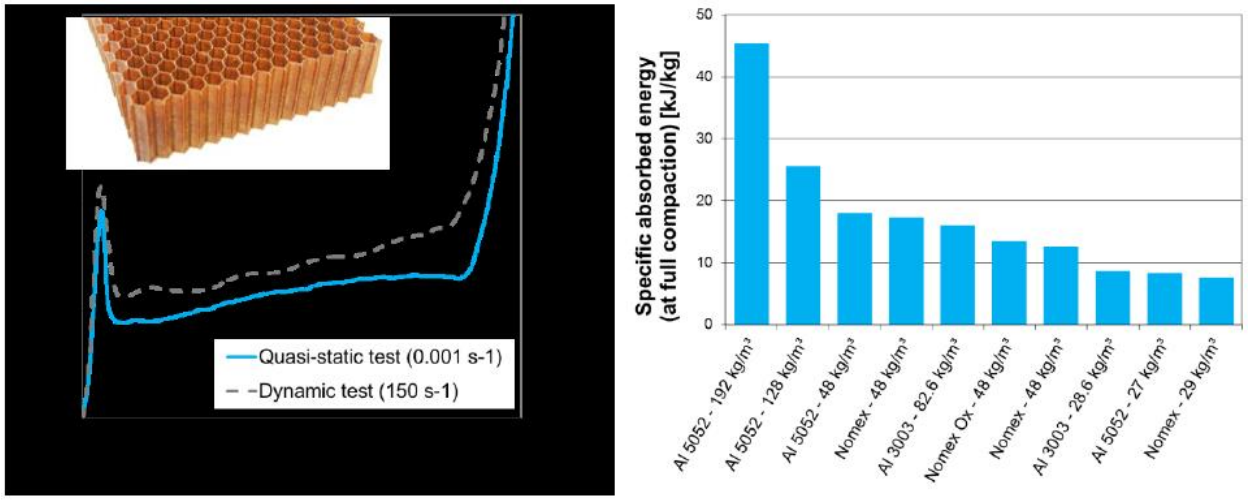

Figure 4: **Typical stress-strain curve of Nomex honeycomb (48 kg/m³) and comparison of specific absorbed energy at full compaction of different honeycomb structures (Heimbs, 2012:4).**

Foams

Polymeric and metallic foams are also commonly used for their energy absorbing characteristics. Examples are Rohacell made of polymethacrylimide (PMI) and Divinycell made

of polyvinyl chloride (PVC). *Figure 5* shows the stress-strain curve for a typical PMI foam and the comparative specific energy absorption characteristics of various polymeric foams.

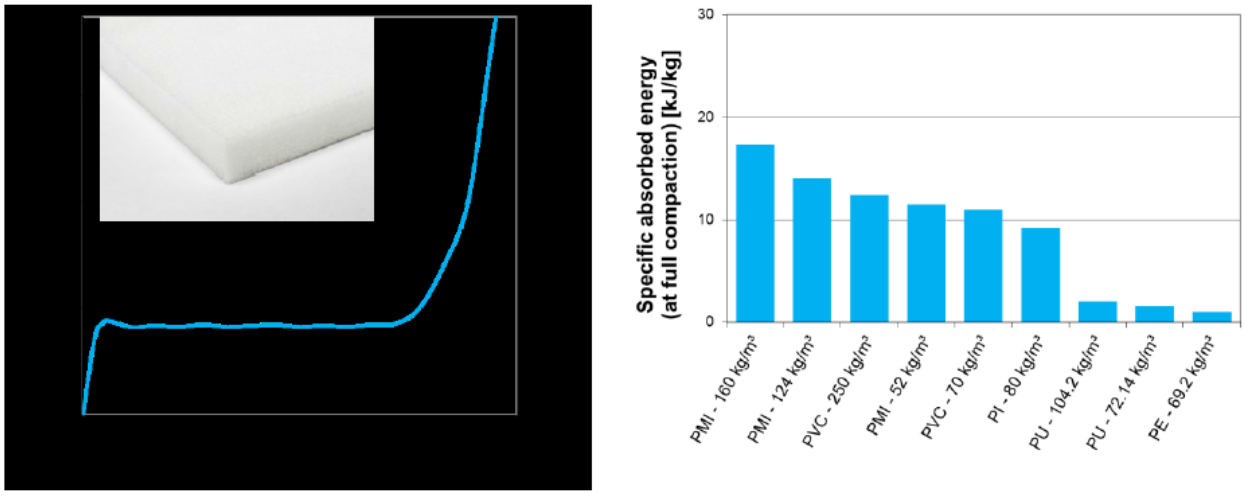

Figure 5: **Typical stress-strain curve of PMI foam and comparison of specific absorbed energy at full compaction of different polymeric foams (Heimbs, 2012:4)**

This comparison shows that aluminium honeycomb materials offer superior energy absorption characteristics compared to other honeycombs and foams. Due to their construction, however, honeycombs can be highly anisotropic (Kröger & Zarei, 2008:203) and are thus better suited to resisting loads that are applied only in their main material axis. Foams, on the other hand, exhibit inferior weight-specific properties, but are potentially better suited to loads applied in multiple axis directions due to their isotropy.

2.1.2.2 Energy absorber design

According to Anghileri *et al.* (2004:433), the modern trend is to design high performance energy absorbers using composite materials for their design flexibility, high specific strength and specific stiffness. Savage (2010:117) goes on to say that carbon fibre reinforced composites offer the highest specific stiffness of any commonly available engineering material.

As opposed to metallic structures that predominantly absorb energy through plastic deformation (Abramowicz, 2003: Alghamdi, 2001, Heimbs, 2012), composite structures absorb energy through complex micromechanical failure mechanisms. The most important mechanisms are matrix cracking, debonding between fibre and matrix, microbuckling, delamination and fibre

breakage (Zhou, 1995:267). More can be read about the accurate finite element simulation of these mechanisms in *Section 2.2*.

Belingardi *et al.* (2012) studied the energy absorption characteristics of simple tubular and complex CFRP energy absorbers. For the tubular components, a simple mass-drop test was done. The acceleration response and impact velocity were measured using an accelerometer and photocell. To ensure stable and progressive crushing, the top edges of the specimens were chamfered. This allowed crushing to initiate at the highly stressed region at the tip of the chamfer.

For the complex component, Belingardi *et al.* manufactured and compared two different design variants. The component was to be used as a frontal crash energy absorber in a Formula SAE race car. It consisted of a pyramidal structure, which ensured stable failure during crushing. A trigger mechanism was included in the design by progressive thinning towards the front end in three distinct zones shown in *Figure 6*. The blue zone is 100 mm long, the green zone 70 mm and the red zone 30 mm. In the first variant, the thickness tapered from 1.4 mm in the blue zone to 0.8 mm in the red zone. In the second variant, the thickness tapered from 2.4 mm in the blue zone to 1.7 mm in the red zone.

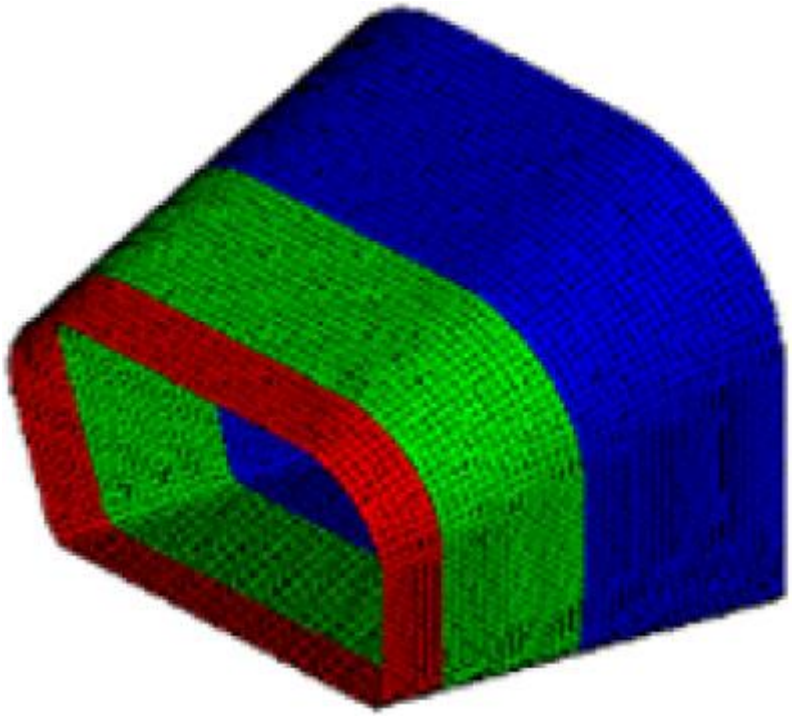

Figure 6: Composite Impact Attenuator (Belingardi *et al.*, 2012:425).

The two components were manufactured and tested under quasi-static axial load. Load was measured using a load-cell. The force results are plotted against displacement in *Figure 7* below.

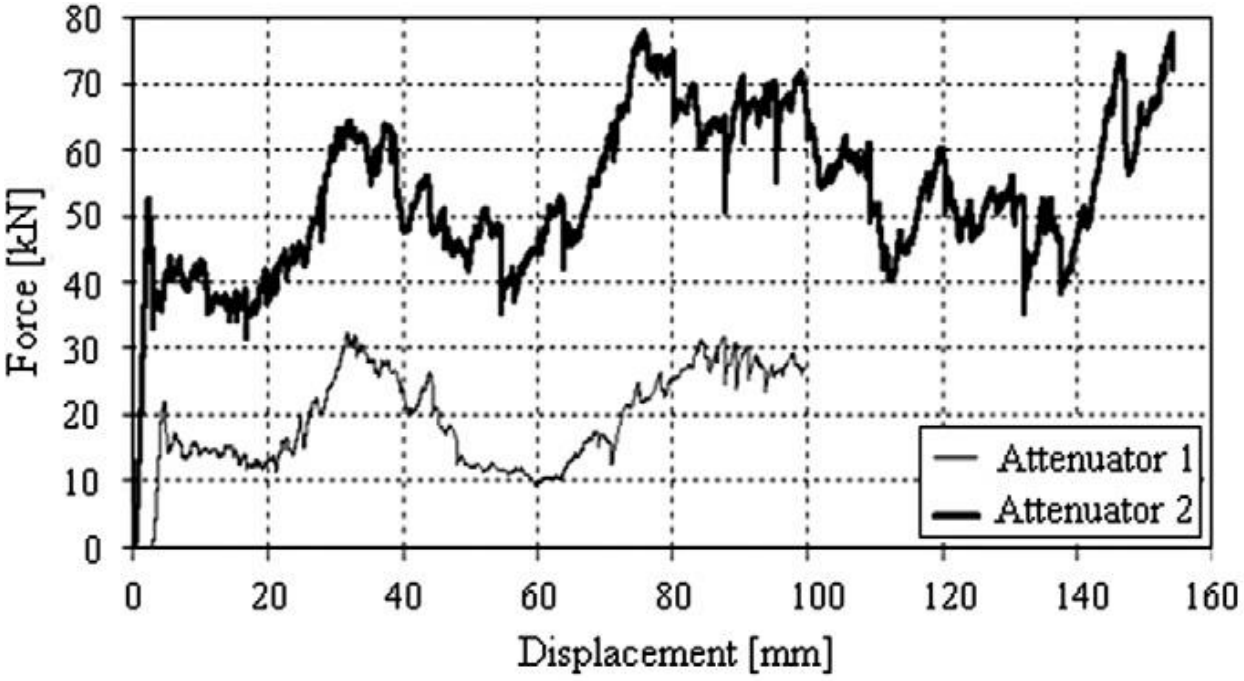

Figure 7: Quasi-static test: comparison of force vs. displacement diagram of two attenuators (Belingardi *et al., 2012:428)*.

As expected, the force transferred by the second, thicker component is roughly double that of the first. This data does not provide much insight into the components' performance under dynamic crash load. It does, however, show that the trigger mechanism was able to cause stable and progressive crushing for both designs with slight load peaks at the interfaces between varying thicknesses. It can further be deduced that simply increasing the thickness of a component to increase energy absorption may produce undesirably large forces, and therefore accelerations. It is clear that the design of an energy absorber should be a multi-objective optimisation with set parameters of energy absorption and allowable displacement while minimising peak forces. This will result in the ideal absorber with plateau-shaped energy absorption curve earlier described by Heimbs.

For the purpose of improving the crash performance of the JS1, combinations of the techniques discussed by Heimbs and Belingardi *et al.* were assessed. Due to the limitations in space and weight, a high performance energy absorber was required. Since honeycomb structures are highly direction sensitive in terms of energy absorption (Kröger & Zarei, 2008:203; Heimbs,

2008:10-12), foams are expected to be better suited to applications such as the JS1 where crash load direction may vary.

2.2 Development of Finite Element Crash Models

Structural finite element solvers can be broadly divided into two categories - those with implicit, and those with explicit time integration schemes. The differences are explained in *Chapter 3,* together with the reasons why explicit solvers are commonly used for crash simulation. They can further be subdivided into specialised linear and nonlinear solvers. The type required to solve a specific problem depends on the physics of that problem.

A crash is typically a combination of various nonlinear phenomena. Examples are the nonlinear stiffness behaviour of materials during large deformation, the associated geometric nonlinearity, propagation of stress waves through material and dynamic vibrational response, to name a few. For these reasons, the leading structural simulation software packages use explicit nonlinear solvers for crash analysis. Examples of software using explicit nonlinear solvers are ANSYS, LS-Dyna and MSC.SimXpert (ANSYS, 2011; LSTC, 2013; MSC, 2011).

2.2.1 Comparison of Crash Solvers

Peng *et al.* (2011) conducted an overview of several crash simulation codes. This work includes an assessment of the current state-of-the-art in numerical crash simulation. KRASH, MSC.Dytran and LS-Dyna are discussed below.

According to Peng *et al.* (2011:287) and Fasanella *et al.* (2001:2), the solver known as KRASH is the result of a US Army-sponsored development by Lockheed-California Company. KRASH is a kinematic code employing a semi-empirical approach using lumped masses, beams and nonlinear springs to model a structure. Although KRASH models are relatively simple, they are dependent on test data to define the springs that determine the crushing behaviour of the structure. These models are also small and computationally inexpensive, but require careful engineering judgement in the definition of spring properties (Peng *et al.,* 2011:287).

Peng *et al.* (2011) also considered MSC.Dytran. This is a three-dimensional, explicit solver for large deformation and fluid-structure interaction problems. The code combines the use of a Langrangian solver for structural aspects of the problem and an Eulerian solver to model fluid aspects. MSC.Dytran has been commercially available since 1992 and has been proven on various ballistic, airbag, blast, collision and crashworthiness problems (Peng *et al.,* 2011:287).

LS-Dyna is a general purpose solver with origins in highly nonlinear transient dynamic finite element analysis with explicit time integration (LSTC, 2012). According to Peng *et al.* (2011:287), the solver includes self-contact, surface-to-surface contact and node-to-surface contact definitions, among others. The current version of the program includes more than a hundred constitutive models and 10 equations-of-state, giving it the capability to simulate a wide variety of material behaviour. LSTC also has its own pre- and post-processing software, known as LS-Prepost.

The LS-Dyna solver is often invoked in other finite element software for its advanced capabilities in explicit dynamic, and specifically crash analysis. Plugge (2005:1) states that LSTC and MSC.Software have entered into a long-term partnership agreement to integrate technology for the benefit of the scientific community. MSC.Nastran and MSC.SimXpert both use the SOL700 sequence, which is the result of this partnership. SOL700 in turn invokes LS-Dyna for explicit dynamic analysis (Plugge, 2005:1).

Due to the superiority of LS-Dyna for crash analysis, the advanced GUI of the MSC packages and the interoperability of the two software families, MSC.SimXpert was used for the JS1 crash simulation. When reference is made to LS-Dyna in subsequent sections of the literature study, its mutual interoperability with MSC.SimXpert and MSC.Nastran is implied.

2.2.2 The Finite Element Mesh

2.2.2.1 Modelling Delamination Failure of Composites

In a study of composite crash boxes, Albertsen *et al.* (2008:247-256) modelled thin-walled structures using material model 54 in LS-Dyna. This model has two failure criterion options. The first option is the Tsai-Wu criterion, which is a quadratic stress-based global failure prediction equation. This option is not suited to crash simulation of composite materials where modelling of post-failure degradation is required (Albertsen *et al.*, 2008:248).

The second option is the Chang-Chang criterion, which is a modified version of the Hashin criterion (Albertsen *et al.*, 2008:248). In this case the tensile fibre failure, compressive fibre failure, tensile matrix failure and compressive matrix failure are separated. Chang-Chang changed this criterion to include nonlinear shear elasticity behaviour and a post-failure degradation rule.

According to Albertsen *et al.* (2008), the post-failure degradation rule will eliminate transverse modulus and minor Poisson's ratio once fibre breakage or matrix shear failure occurs, but will keep longitudinal and shear modulus following a Weibull distribution. If the first failure is matrix

tensile or compressive failure, the same applies, but the longitudinal shear modulus will remain unchanged.

When this failure criterion was used by Albertsen *et al*. (2008) in combination with multi-element-layers capable of simulating delamination failure, the correlation between the experimental and numerical results was exceptionally close. On the other hand, when these elements were simplified to single-element-layer, the energy absorption in the numerical model was significantly underestimated.

In the figures below, crash load and energy absorption recorded during the mass drop tests are plotted against displacement. The experimental and simulated results are plotted together to show the degree of correlation. In *Figure 8*, results obtained from the simulation using the single-element-layer method are compared. Results from the multi-element-layered model are shown in *Figure 9.*

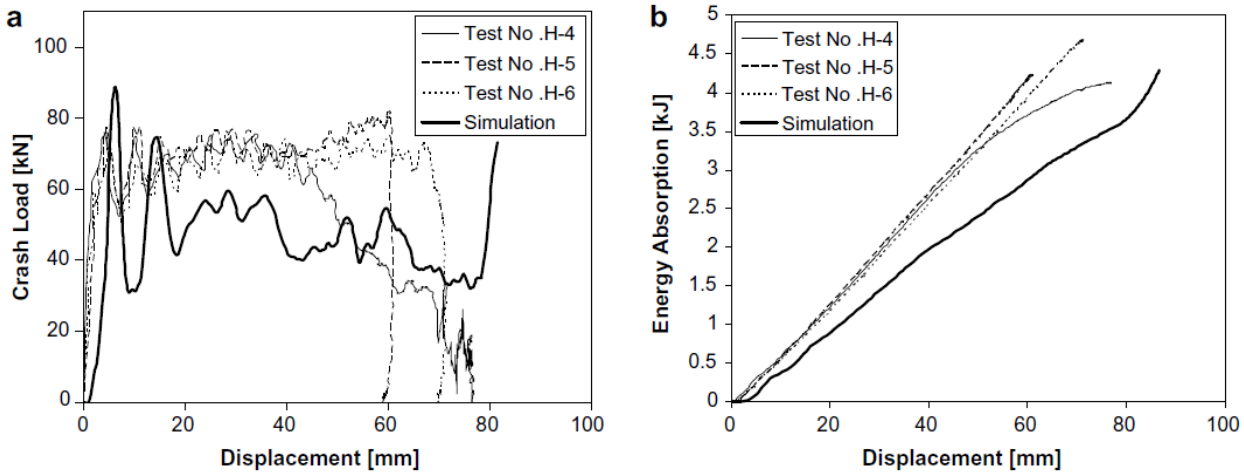

Figure 8: **Comparison between experimental and numerical (single layer method) curves of (a) crash load displacement curve (b) energy absorption displacement curve of hexagonal composite tubes (Albertsen *et al*., 2008:254).**

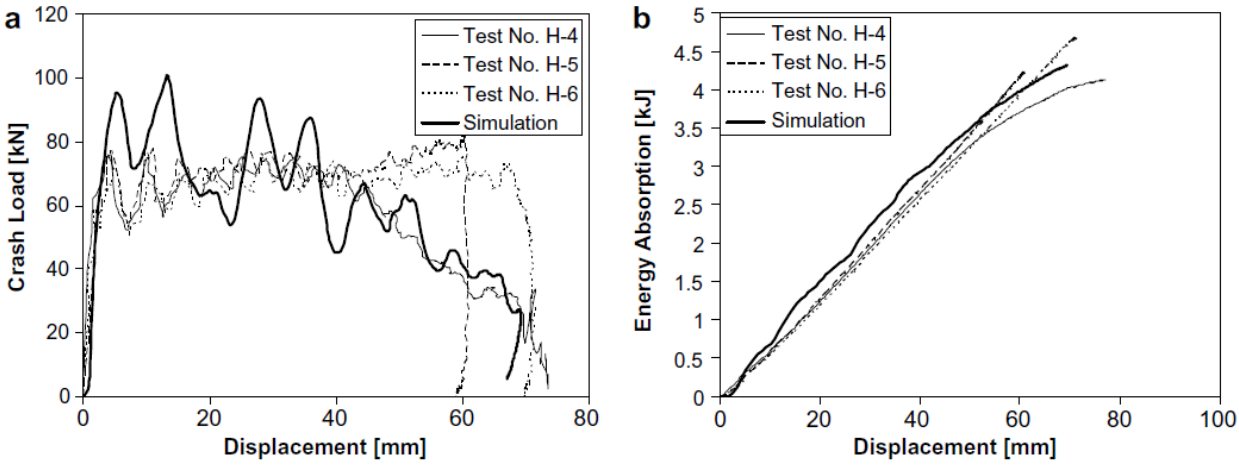

Figure 9: **Comparison between experimental and numerical (multi-layers method) curves of (a) crash load displacement curve (b) energy absorption displacement curve of hexagonal composite tubes (Albertsen *et al.*, 2008:254)**

This study showed that energy absorption was underestimated by 22.3% when multiple laminate layers were simplified into a single element layer. This is attributed to the inability to simulate delamination failure, which accounts for a significant portion of energy absorption. Comparatively, the results in *Figure 9* show that exceptional accuracy can be achieved with advanced multi-layered models.

A further noteworthy technique was used in the study by Albertsen *et al.* (2008). The corners joining the flat vertical surfaces of the crash boxes were modelled using a 0.5 mm offset that was filled with a deformable spot weld with reduced strength. This enabled the accurate simulation of splitting at the corners.

Figure 10 below shows a section view of a square crash box model with a 0.5 mm corner offset that was filled with a weakened deformable spot weld. The model was built to demonstrate the complexity of multi-element-layered meshes.

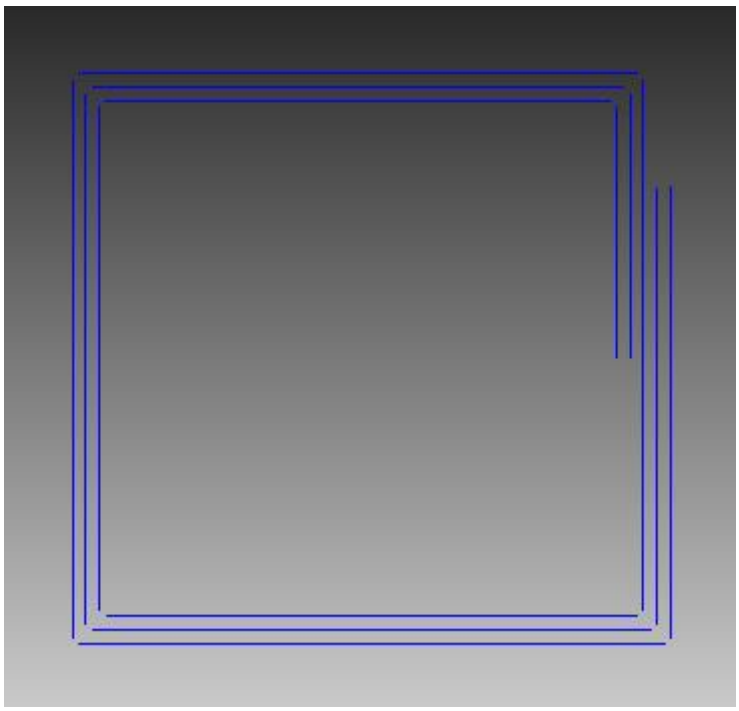

Figure 10: Section view of a multi-element-layered square crash specimen with 0.5 mm corner offsets.

As opposed to the study by Albertsen *et al*. (2008), which simulated a geometrically simple structure, it is not feasible to model a complex structure such as the JS1 fuselage using the multi-element-layered approach. This will result in an overly complex model that will be computationally expensive. However, it has been shown in another study (Byar *et al.,* 2011:1814) that energy absorption can be simulated accurately using the single-element-layer approach by adjusting specific parameters in the LS-Dyna material model number 54. This approach is discussed in detail at the end of *Section 2.2.3,* which covers material models.

2.2.3 Material Models

The work of Ebert *et al.* (2009:1422-1426) further emphasises the importance of accurate material modelling when simulating impact in composite materials. In their study of the strain rate dependant material properties and failure behaviour of Multi-Layered Knitted Fabric (MKF) reinforced epoxy materials, it can be seen that tensile strength and fracture strain vary significantly at different strain rates. Similar results were obtained by Heimbs *et al.* (2007:2836).

Ebert *et al.* conducted high speed tensile tests to determine the in-plane material behaviour of specimens at various velocities. Loading velocities ranging from 0.1 mm/s to 10 m/s were

applied to similar specimens. The results show that tensile strength can increase significantly with increasing strain rate. It is also shown that the strain at failure increased with increasing strain rate. It can therefore be said that the energy absorption properties of the material are highly dependent on the strain rate. *Figure 11* and *Figure 12* below show the results of this study. GF indicates glass fibre, AR indicates aramid fibre and PE indicates polyethylene fibre.

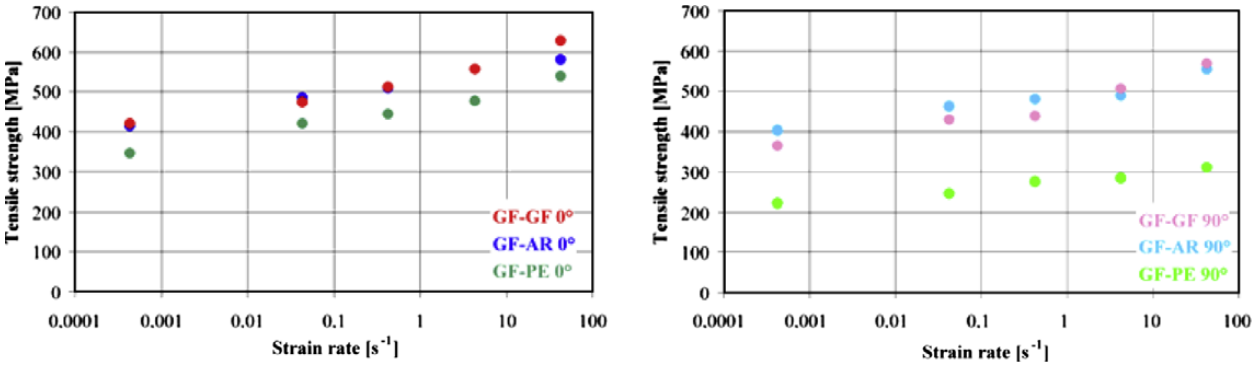

Figure 11: **Strain rate dependent tensile strengths of hybrid MKF composites in warp (0°) and weft (90°) direction (Ebert *et al.*, 2009:1425).**

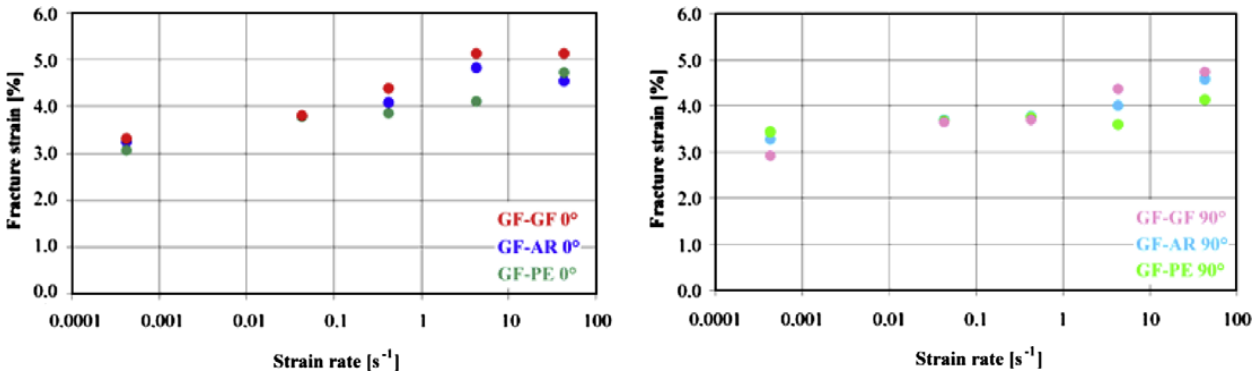

Figure 12: **Strain rate dependent strains at failure of textile reinforced composites (Ebert *et al.*, 2009:1425).**

Fritzsche *et al.* (2008:337) conducted a study of the crash response of a glass mat reinforced thermoplastic (GMT) crash box. They noted that fibre-reinforced plastic (FRP) materials behave very differently to metals once their yield strength is exceeded. As opposed to metals, FRP materials soften during plastic deformation due to accumulation of failure. In an effort to develop a model that could accurately simulate these unique failure mechanisms, they divided their approach into four focus areas. These are modelling of strain localisation, integration of material inhomogeneity, strain rate modelling and the requirements for geometric modelling.

Fritzsche *et al.* (2008:339) selected the “Fracture Energy Regularisation” method to counteract strain localisation when modelling crack development. In this approach the crack is modelled by a line of elements that are deleted as the crack progresses. The approach was selected due to its simplicity and low computational cost (Fritzsche *et al.,* 2008:339).

Fritzsche *et al.* (2008:343) also studied the strain rate dependence of GMT materials. Significant increases in ultimate strength and strain with increased strain rate were considered. Since the material model MAT_LAMINATED_COMPOSITE_FABRIC is not capable of simulating strain rate dependence, the mean strain rate was estimated and the corresponding material properties were implemented in the model (Fritzsche *et al.*, 2008:343).

Lastly, Fritzsche *et al.* (2008:343) discussed the importance of a detailed geometric model and commented that the failure modes in thin-walled structures depend heavily on fine geometric details. They used the abovementioned techniques to model a crash test of a box-shaped thin-walled structure using LS-Dyna material model MAT_058. The same test was then physically conducted and results compared. In the simulation and test, a sledge fitted with an accelerometer was crashed into the crash specimen to determine crash response (Fritzsche *et al.*, 2008).

Figure 13 below shows the various degrees of accuracy that were achieved by Fritzsche *et al.* by comparing physical test data and simulation results of models using various combinations of the abovementioned techniques. It can be seen that the model with no adjustments vastly underestimated peak accelerations during crushing. Since the acceleration is linearly related to force and therefore energy absorption, it can be deduced that energy absorption was underestimated also. On the other hand, *Figure 13* shows that the simulation with all techniques implemented, achieved accelerations that are nominally within 10% of the experimental results.

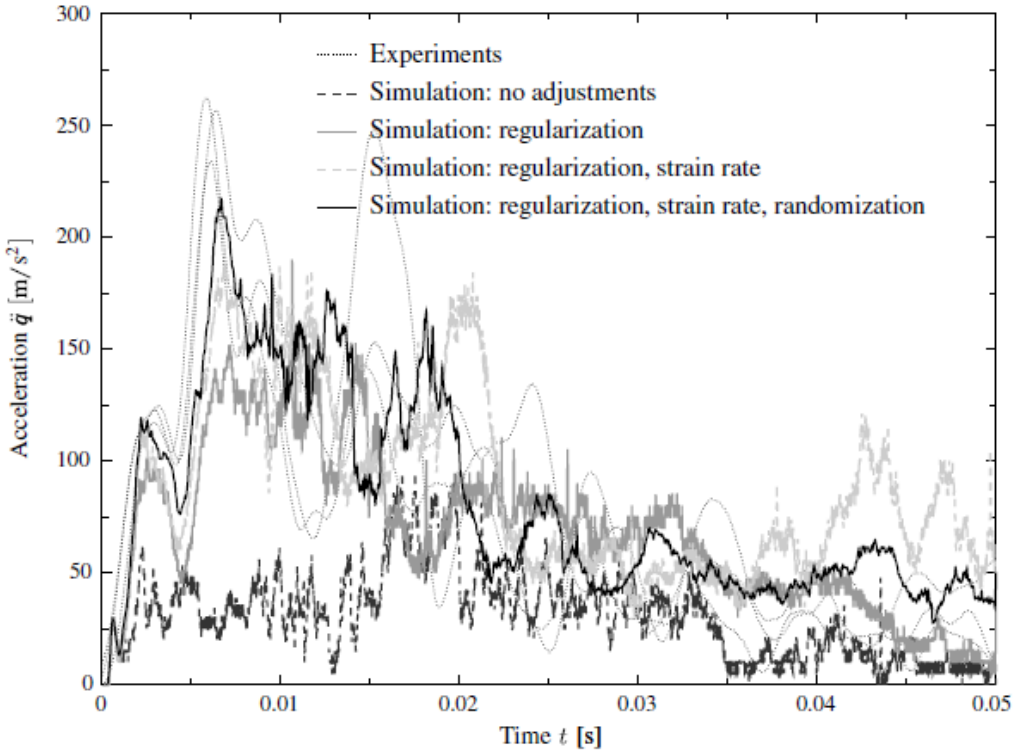

Figure 13: Sledge acceleration vs. time in crash simulation; adaptation of the simulation model (Fritzsche *et al.*, 2008:346).

The results published by Fritzsche *et al.* and Ebert *et al.* show the importance of strain rate sensitivity when modelling impact. However, strain rate sensitivity can only be accurately modelled when the strain rate dependant material properties are known. This data is not available for the construction materials of the JS1. Since the work of Fritzsche *et al.* and Ebert *et al.* further shows an increase in ultimate strength and strain at higher strain rates, it can be deduced that properties obtained from quasi-static tests will result in lower energy absorption than those obtained at higher strain rates. It will therefore be conservative to assume, for the purpose of simulation, that the materials used in the JS1 do not exhibit strain rate dependency. The assumption will always result in underestimation of energy absorption rather than overestimation.

2.2.3.1 Material model for advanced composite failure simulation

As discussed in *Section 2.1.2.2*, the energy absorption characteristics of a laminated composite material are dependent on various interlaminar and intralaminar mechanisms (Zhou, 1995:267). In a study of the simulation of laminated composites using LS-Dyna material model number 54, Byar *et al.* (2011:1814) showed that this model can be used in single-element-layer format to generate a simulation that closely approximates experimental data. As opposed to the work of

Albertsen *et al.* (2008) in *Section 2.2.2.1*, which suggests that multiple element layers are required to produce accurate results, this method offers a computationally efficient alternative.

Byar *et al*. (2011) achieved simulated results for *SEA,* which were within 4.4% of experimental results. *Figure 14* below shows the degree of agreement between experimental and simulated load-displacement curves of a corrugated crush specimen with sinusoidal cross-section.

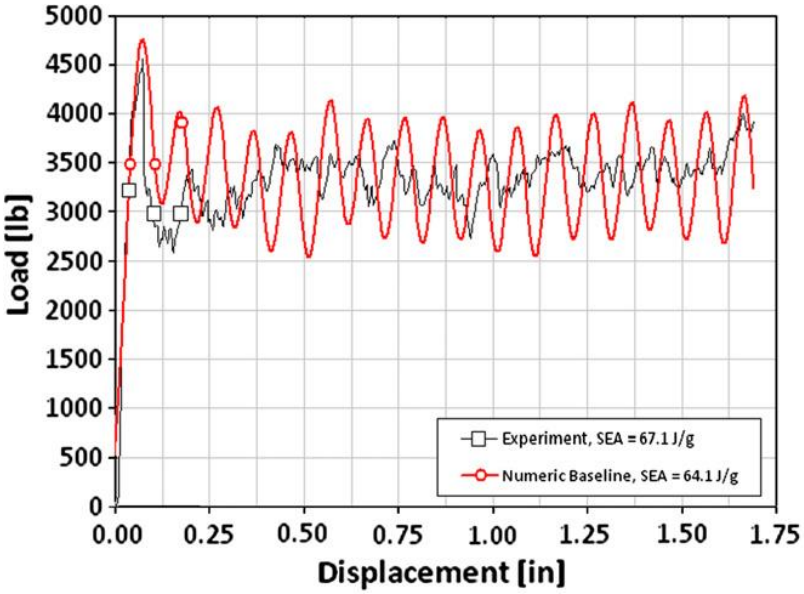

Figure 14: Experimental and simulated load displacement curves for crushing behaviour of a corrugated laminate specimen (Byar *et al.,* 2011:1814)

This study further suggests that material model input parameters are best adjusted by trial and error (Byar *et al.,* 2011:1810). This is due to some parameters being purely numerical expedients used to achieve specific material behaviour rather than physical properties, which can be determined experimentally. The research by Byar *et al.* included a full parametric study of LS-Dyna MAT54 inputs and their effect on simulated results. The inputs required to define a material in MAT54 are given in *Table 1*.

Byar *et al.* (2011) considered two categories of input parameters – those which can be determined experimentally, and those which cannot. Examples of the former are stiffness, ultimate strength and Poisson's ratio. The latter are discussed in the following paragraphs and have no physical meaning, but are used to numerically define failure behaviour in the material model. Since the changes in the first group of parameters yielded predictable results, the remainder of this section focuses on the correct adjustment of the second group.

Byar *et al.* (2011:1819) showed that the SOFT parameter was the single most influential input and was able to shift *SEA* by as much as 30% above and below the baseline value. This parameter is described as the crush front strength-reducing factor and is used to influence the strength of elements at the impact front in order to simulate stable crushing behaviour. A parametric study of this input was done for the allowable range of 0 to 1. The results are shown in *Figure 15* below.

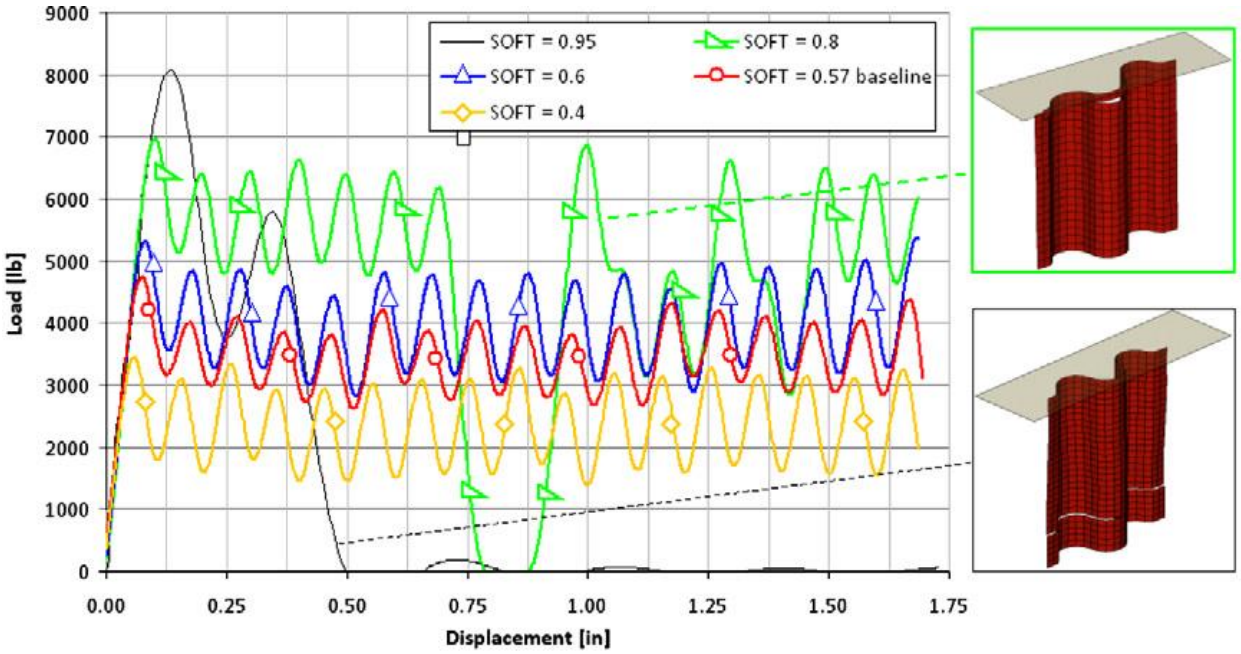

Figure 15: The effect of variation of the SOFT parameter in LS-Dyna material model 54 on crash load (Byar *et al.,* 2011:1819)

It is clear from their results that a higher value for SOFT will produce a higher crushing load and a lower value will produce the opposite effect. Similarly, it will increase or decrease energy absorption. Byar *et al.* (2011:1819) also recorded that a value of 0.95 for SOFT resulted in buckling of the entire structure, rather than stable progressive crushing. It was stated that the SOFT parameter can be interpreted in the physical world as a damage zone where local delamination and cracking occurs at the crash front (Byar *et al.,* 2011:1819).

ALPH is described as a weighting factor for the nonlinear term in the shear stress equation. A total insensitivity to variation in ALPH was observed by Byar *et al.* (2011:1817). This parameter affects the third order term of the shear failure equation (*Equation 1*), shown below, used in MAT54.

$$2\varepsilon_{12} = \frac{1}{G_{12}}\tau_{12} + \alpha{\tau_{12}}^3 \quad [1]$$

BETA, described as the shear factor in fibre tension, was also found to have no noticeable effect on the outcome of the simulation as long as it was within the allowable range specified in the LS-Dyna User's Manual (Byar *et al,.* 2011:1817). This observation, together with an insensitivity to variation in maximum fibre tensile stress and strain parameters, suggests that fibre tensile failure is not a dominant damage mechanism in this type of crushing.

FBRT and YCFAC are strength reduction factors for fibre tensile and compressive strength after matrix failure. Byar *et al.* (2011:1819) found that variations between 0 and 1 in FBRT, and 0 to 7.4 in YCFAC showed minimal effect on the simulation. These parameters are modifiers for fibre strength of elements that have already experienced some damage, but have not yet failed completely.

TFAIL is a means to set a minimum allowable time step for the explicit solver. Elements are deleted once their time step decreases to below the value specified in TFAIL. Byar *et al.* (2011:1819) warn that large values for TFAIL (i.e. 0.001) should be avoided, since it will lead to premature element deletion. They also note that the time step is calculated by LS-Dyna to satisfy the Courant stability criterion. See *Chapter 3* for an explanation of this criterion.

Ultimately, Byar *et al.* created *Table 1* with recommended ranges for inputs for the LS-Dyna material model 54 based on the results of their parametric study.

MAT54 input parameter definitions.

Variable	Definition	Suggested value
MID	Material identification number	Any arbitrary integer
RO	Mass per unit volume*	ρ From material properties
EA	Young's modulus in longitudinal direction	E_1, from material properties
EB	Young's modulus in transverse direction	E_2, from material properties
PRBA	Minor Poisson's ratio, $v_{ba} = v_{21}$	Calculated using v_{12}, E_1 and E_2
PRCA	Minor Poisson's ratio, $v_{ca} = v_{31}$	Not used
PRCB	Minor Poisson's ratio, $v_{cb} = v_{32}$	Not used
GAB	Shear modulus, G_{ab}	G_{12}, from material properties
GBC	Shear modulus, G_{bc}	Assumed equal to G_{ab}
GCA	Shear modulus, G_{ca}	Assumed equal to G_{ab}
KF	Bulk modulus of matrial	Not used
AOPT	Material axes option parameter	AOPT = 3
A1 A2 A3	Vector components to define material axes for aopt = 2	Not used
MANGLE	Material angle in degrees used when aopt = 3	90°
V1 V2 V3	Vector components to define the material axes for aopt = 3	Unit vector in z direction: $v1 = 0$, $v2 = 0$, $v3 = 1$
DFAILT	Max strain for fiber tension	Calculated using E_1 and F_1^{tu}
DFAILC	Max strain for fiber compression	Calculated using E_1 and F_1^{cu}
D1 D2 D3	Vector components to define the material axes for aopt = 2	Not used
DFAILM	Max strain for matrix straining in tension and compression	Greater than or equal to the maximum value of (YT/EB) or (YC/EB)
DFAILS	Max shear strain	$0 < \text{DFAILS} \leqslant 0.1$
EFS	Effective failure strain	EFS = 0
TFAIL	Time step size criteria for element deletion	Must be very small but nonzero
ALPH	Shear stress non-linear term	$1E\text{-}3 \leqslant \text{ALPH} \leqslant 1$
SOFT	Crush front strength reducing parameter	Must be calibrated by trial and error
FBRT	Softening factor for fiber tensile strength after matrix failure	$0 \leqslant \text{FBRT} \leqslant 1$
YCFAC	Softening factor for fiber compressive strength after matrix failure	$0 \leqslant \text{YCFAC} \leqslant (\text{XC/YC})$
BETA	Weighing factor for shear term in tensile fiber mode	Any value: $0 \leqslant \text{BETA} \leqslant 1$
XC	Longitudinal compressive strength	F_1^{cu}, from material properties
XT	Longitudinal tensile strength	F_1^{tu}, from material properties
YC	Transverse compressive strength	F_2^{cu}, from material properties
YT	Transverse tensile strength	F_2^{tu}, from material properties
SC	Shear strength	F_{12}^{tu}, from material properties
CRIT	Failure criterion used (MAT54 Chang-Chang, MAT55 Tsai-Wu)	Assign value of 54 or 55

* For English units, must be divided by a gravity factor to convert from pound-weight to pound-mass.

Table 1: Recommended ranges for settings in LS-Dyna material model 54 (Byar *et al.,* 2011:1815)

A similar parametric study was done by Feraboli *et al.* (2010), where a single square element was analysed. Different composite properties were applied to the element, which was then loaded axially in tension and compression to study the effects of changes to various MAT54 parameters. Stress, strain and energy results were subsequently compared to expected results to determine the effect of each parameter.

In order to ensure the correct behaviour of each material model that was used in the JS1 simulation, this single element approach was applied as an accuracy control measure. This improves confidence in the results of the full crash model by confirming that the elements which make up the JS1 model will behave correctly under load. The knowledge gained from the study by Byar *et al.* (2011), discussed earlier in this section, was applied to correct any unpredicted behaviour. *Figure 16* shows the element used by Feraboli *et al.* (2010), which will be replicated to study the material models to be used in the JS1 crash simulation.

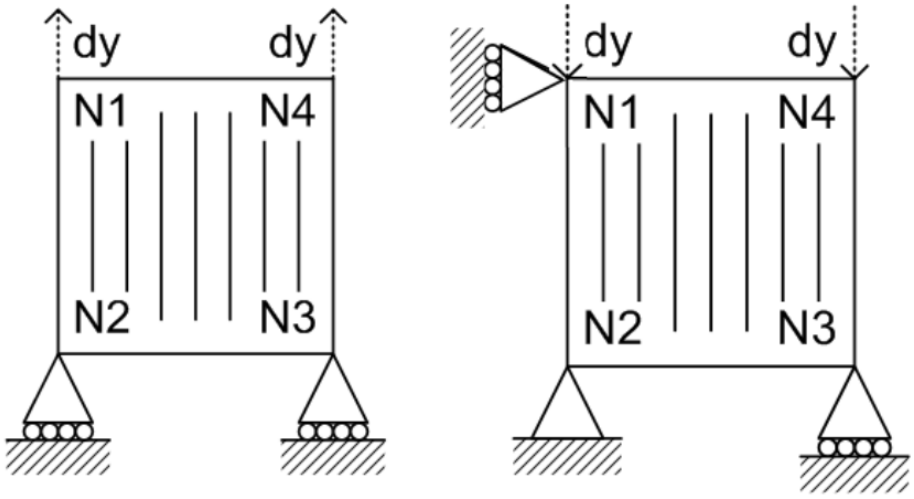

Figure 16: Single elements used for tension (left) and compression (right) in parametric study of LS-Dyna material model 54 (Feraboli *et al., 2010:20*).

2.3 Model Fidelity

2.3.1 Model Quality Checks

Fasanella and Jackson (2002) recorded their experience from several crash simulations validated by physical tests at the NASA Langley Research Center. This study provides valuable information about how to develop and execute crash simulations, and how to perform the required quality checks.

Fasanella and Jackson (2002:2) state that knowledge of physics, material science and nonlinear behaviour is a prerequisite for crash simulation. This enables the analyst to perform quality checks on the data fed into the model as inputs, as well as the results generated by the model. In ideal situations, it is best to validate simulation results against physical test data. When such data is not available, the analyst can use other methods to check the accuracy of the results, such as observation of the system and component energies in the simulation for anomalies (Fasanella & Jackson, 2002:8).

Fasanella and Jackson (2002:14-15) also recommend the following checks prior to simulation to ensure model fidelity. The analyst should compare the total mass, mass distribution and mass of individual parts to those of the actual components. Checks must also be done to ensure that the center-of-gravity (CG) of the model is in the correct position. Furthermore, if any experimental data, such as measurements of deflection under static load, are available, those experiments should be simulated and their results compared. These tests can assist in determining whether characteristics such as the overall stiffness of the model are acceptable (Fasanella & Jackson, 2002:15).

2.4 Analysis of Results

2.4.1 Post-processing of Results

The results of finite element crash simulations, such as the acceleration time-history of a particular node in the model, are often noisy and unsuitable for analysis unless smoothed. Fasanella and Jackson (2002:15) state that such high-frequency content should be filtered. Careful engineering judgement can also be used to add mass to nodes from which acceleration responses will be extracted. This is particularly important when simulation data will be compared to physical test data obtained from an accelerometer mounted at a point on the structure (Fasanella & Jackson, 2002:15).

To show the effects of filter frequency and nodal mass in the finite element mesh, *Figures 17-19* below give the filtered acceleration time histories of two nodes in a crash model. Note the different cut-off frequency in each case. Node 3572 has no added nodal mass, while node 3596 has 122.8 lbs of concentrated mass.

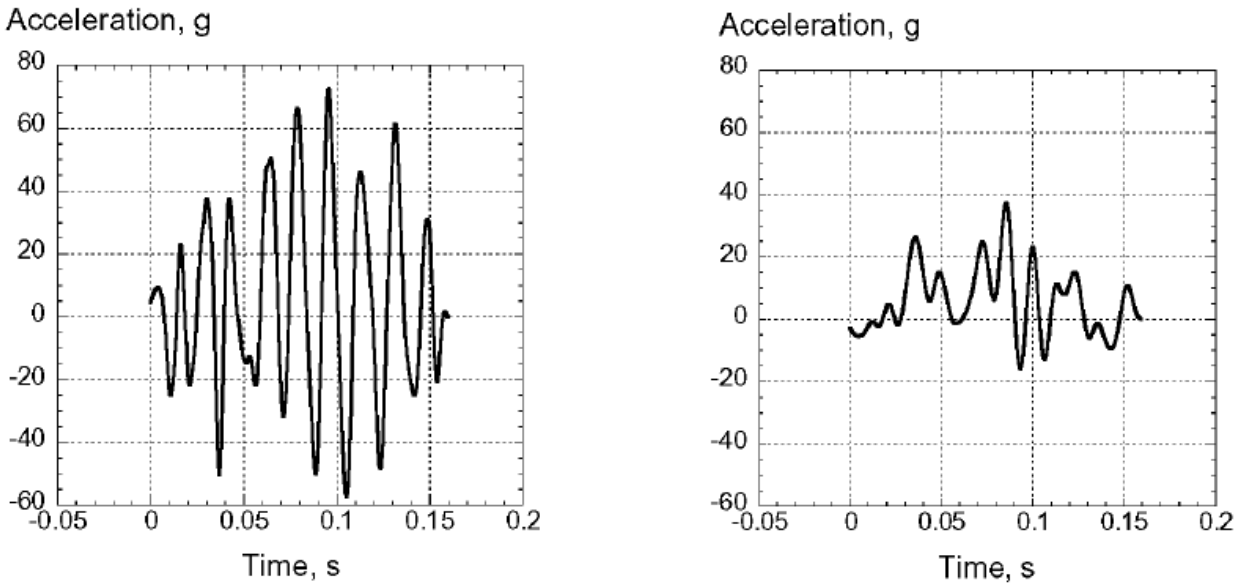

Figure 17: **200Hz filtered acceleration responses of node 3572 (left) and node 3596 (right) (Fasanella & Jackson, 2002:16).**

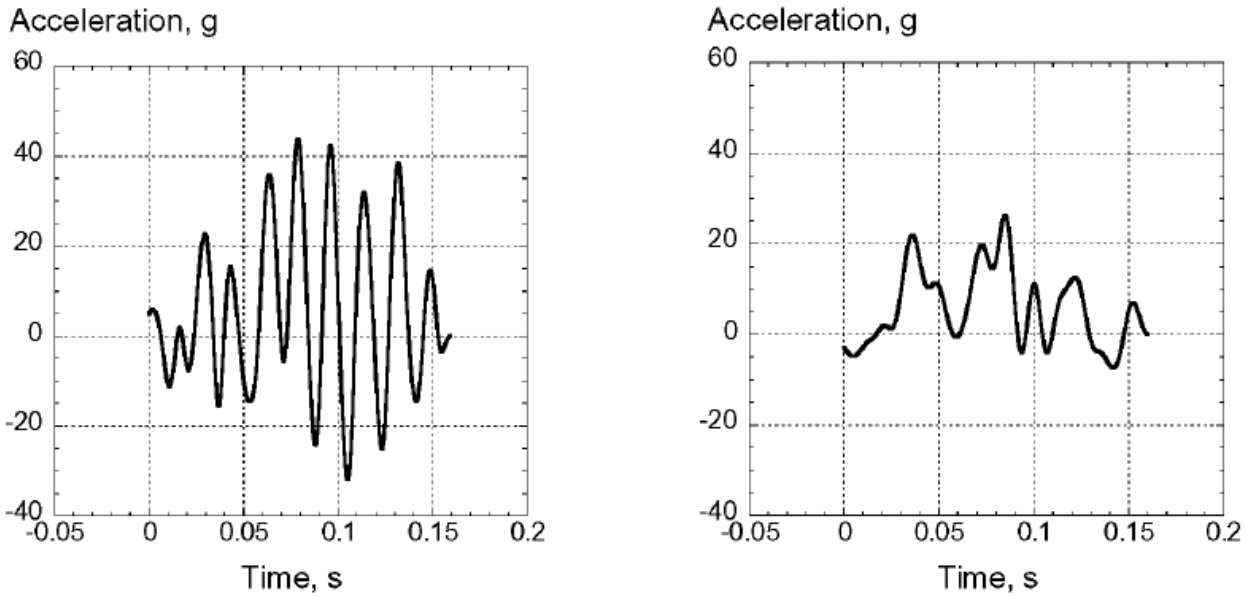

Figure 18: **125Hz filtered acceleration responses of node 3572 (left) and node 3596 (right) (Fasanella & Jackson, 2002:16).**

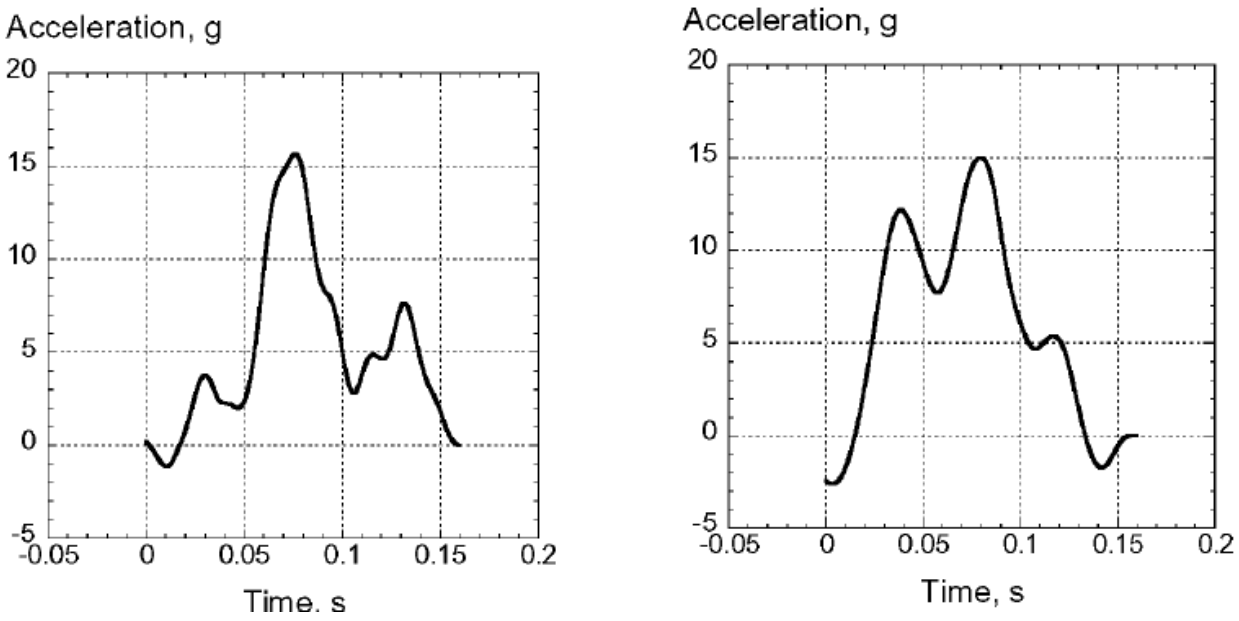

Figure 19: 40Hz filtered acceleration responses of node 3572 (left) and node 3596 (right) (Fasanella & Jackson, 2002:16).

Note the noisy time histories resulting from 200Hz and 125Hz filtration. Note also the difference in noise and amplitude due to the difference in mass of the two nodes. In this case, the time history filtered at 40Hz reveals the underlying crash pulse.

2.5 Chapter Conclusion

The information reviewed in this chapter indicates that each of the objectives of the study can indeed be achieved on a numerical basis. In summary, the findings are as follows.

Two general principles dictate the design of crashworthy structures. The first and most important one is to maintain a safe volume around the occupant. This concept appears in several sources (Abramowicz, 2003; Röger, 2007; Segal, 1998; EASA, 2009; FIA, 2013) and is generally achieved by stiffening and strengthening the structure surrounding the occupant to prevent collapse during impact.

The second principle is to limit the acceleration loads imparted to occupants during a crash by energy absorption. As noted in a study by Heimbs (2012), this can be achieved by placing energy absorbing structural elements around the safe volume to convert kinetic energy into other forms of energy through deformation. Since energy absorption in crushing is represented by the area under the force displacement curve, the design of an energy absorber should aim to

achieve a plateau-shaped curve. This will result in minimised peak acceleration while maximising energy absorption.

The materials that are typically used in the construction of energy absorbers were identified. These include metals such as aluminium and titanium, composites such as CFRP and synthetic fibres such as Dyneema. These materials are widely used in various combinations and configurations such as laminates, honeycombs and foams. Due to their design flexibility and excellent weight-specific mechanical properties, composite materials dominate modern energy absorber design. Considering that the existing structure of the JS1 consists of fibre-laminate composites, this group of materials was used as a base in the concept development of the enhanced JS1 structure.

For the purpose of simulation, four commercially available finite element software packages were considered, namely KRASH, MSC.Dytran, LS-Dyna and MSC.SimXpert. In a review of their capabilities, MSC.Simxpert was selected as the preferred solver for the JS1 crashworthiness study. This is due to its advanced GUI, which is specifically suited to crash modelling, and due to the availability of the SOL700 sequence, which invokes LS-Dyna for explicit dynamic analysis.

Next, in *Section 2.1.2.2*, it was found that the failure mechanisms in composite materials are significantly different from those in other materials. Composites absorb energy through various micromechanical mechanisms such as matrix cracking, debonding between fibre and matrix, microbuckling, delamination and fibre breakage. These mechanisms pose a unique challenge in terms of numerical definition of material behaviour for finite element analysis. Nonetheless, options have been found in literature to accurately simulate composite crushing behaviour.

Albertsen *et al.* (2008) successfully modelled each layer in a composite structure as a layer of finite elements. The layers were then bonded using a tied surface-to-surface contact definition. Even though this method produced highly accurate results, it will not be selected for the JS1 simulation due to its computational expense.

A less computationally expensive method was used by Byar *et al.* (2011), who adjusted material model parameters to account for the underestimation in energy absorption achieved when using a single element layer.

Ebert *et al.* (2009) and Fritzsche *et al.* (2008) noted the effect of strain rate on material properties. Ebert *et al.* (2009) specifically showed that ultimate strength and strain increased with strain rate. Fritzsche *et al.* (2008) compensated for a lack in strain rate modelling capability in their chosen material model, by estimating strength and strain properties at a mean strain

rate. For the purpose of the JS1 simulation, the conservative assumption was that materials do not exhibit strain rate sensitivity. The properties determined by quasi-static testing of the materials are assumed to represent the material properties at all strain rates. This approach is considered to be conservative since it will result in underestimation of energy absorption, rather than overestimation.

Single element simulations of tension and compression in the 0° and 90° direction were used by Feraboli *et al.* (2010) in a parametric study of the input parameters of MAT54. By studying the failure of the element under different conditions, the effects of changes in parameters became known. As a validation of the modelling technique, these tests were replicated for each of the materials defined in the JS1 model to verify the intended failure behaviour.

Chapter 3 Theoretical Background

This chapter is an introduction to the mathematical principles used in explicit solvers. Knowledge of explicit methods is prerequisite to subsequent chapters in order to understand the reasoning behind certain aspects of the JS1 crash simulation. The chapter begins with a brief look at the strengths and weaknesses of implicit and explicit methods. The focus then moves onto those explicit methods applicable to this study. An explanation of the Courant-Friederichs-Lewy criterion is given, after which the chapter concludes with an overview of the effect of this criterion in simulations where large deformation is present.

3.1 Solution Time Integration

Software packages such as LS-Dyna and SimXpert use explicit solvers for crash simulation (LSTC, 2013; MSC, 2011). Unlike implicit solvers they do not require decomposition of the model's stiffness matrix at each time step, making them more efficient in certain applications.

Although implicit methods can be used to solve transient problems, they are computationally expensive (LSTC, 2013:57-2). These methods calculate the global stiffness matrix, which is inverted and applied to the nodal out-of-balance force to produce a displacement increment. The time step length is determined by the user and the solution will be unconditionally stable for any selected time step (MSC, 2011:20). The disadvantage is the computational cost to continuously manipulate the stiffness matrix, resulting in fewer but more expensive time steps (LSTC, 2013:57-2).

Solvers with explicit time integration, on the other hand, summate internal and external forces at each node point and divide by nodal mass to calculate nodal acceleration. The analysis advances in time by integrating the acceleration. The disadvantage to this method is that the maximum time step is limited by the Courant, Friederichs and Lewy (CFL) stability condition, which considers sound speed across the smallest element in the model (See 3.2). This typically results in many time steps at lower computational expense per step (LSTC, 2013:57-1). A basic mathematical description of the method is given below.

The equation of motion for a spatially discretised structure is:

$$Ma_n + Cv_n + Kd_n = F_n^{ext} \quad [2]$$

where

$M = mass\ matrix.$

$C = damping\ matrix.$

$K = stiffness\ matrix.$

$a_n = vector\ of\ nodal\ accelerations.$

$v_n = vector\ of\ nodal\ velocities.$

$d_n = vector\ of\ nodal\ displacements.$

$F_n^{ext} = vector\ of\ externally\ applied\ loads.$

$Cv_n + Kd_n = F_n^{int} = vector\ of\ internal\ loads.$

This can be rewritten as:

$$Ma_n = F_n^{ext} - F_n^{int} \quad [3]$$

$$= F_n^{residual} \quad [4]$$

so that

$$a_n = M^{-1}F_n^{residual} \quad [5]$$

In explicit finite element codes, the mass matrix is lumped, giving a diagonal matrix that will result in a trivial inversion. This matrix consists of a set of independent equations for each degree of freedom. For example:

$$a_{ni} = \frac{F_{ni}^{residual}}{M_i} \quad [6]$$

In order to advance in time, a central difference approximation of acceleration at time n is made based on velocities defined at time $n + \frac{1}{2}$ and $n - \frac{1}{2}$. This is called the leapfrog scheme and can be represented graphically as follows:

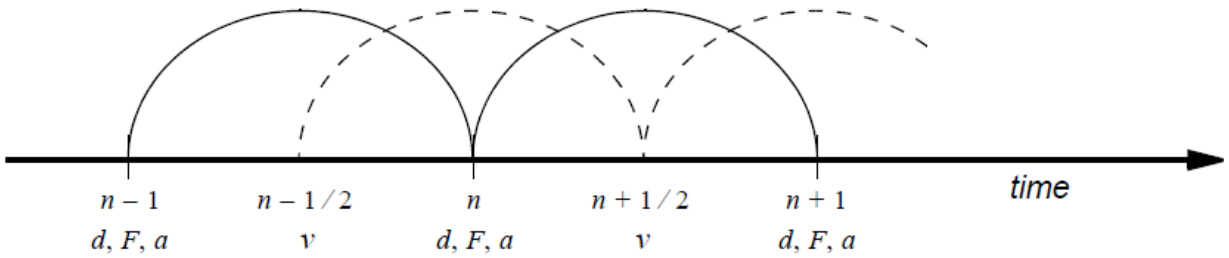

Figure 20: Graphical representation of leapfrog scheme (MSC, 2011:19).

Velocity at $n+\frac{1}{2}$ is calculated as follows:

$$v_{n+\frac{1}{2}} = v_{n-\frac{1}{2}} + \frac{a_n(\Delta t_{n+\frac{1}{2}} + \Delta t_{n-\frac{1}{2}})}{2} \quad [7]$$

The nodal displacement is therefore:

$$d_{n+1} = d_n + v_{n+\frac{1}{2}} \Delta t_{n+\frac{1}{2}} \quad [8]$$

3.2 The Courant-Friederichs-Lewy Stability Criterion

In order to ensure stability, the time step for an undamped problem should be

$$\Delta_t \leq \frac{2}{\omega_{max}} \quad [9]$$

where ω_{max} is the maximum eigenfrequency of the finite element mesh. It can be shown that

$$\omega_{max} \leq \omega^e_{max} \quad [10]$$

where ω^e_{max} is the maximum eigenfrequency of any element in the mesh. The CFL criterion is a physical interpretation of this limit (Cocchetti *et al.*, 2013:39).

During a solution, the solver loops through all elements in the model to update the stresses and residual force vector. It also calculates a new time step based on the smallest time step of any element in the model.

$$\Delta t^{n+1} = a \cdot \min\{\Delta t_1, \Delta t_2, \Delta t_3, \dots, \Delta t_N\} \quad [11]$$

Where N is the number of elements in the model and a is a scale factor to ensure stability, typically set to 0.9.

Using the CFL criterion, the time step for a shell element is calculated by

$$\Delta t_e = \frac{L_s}{c} \quad [12]$$

where L_s is the characteristic length of the element and c is the speed of sound given by

$$c = \sqrt{\frac{E}{\rho(1-v^2)}} \quad [13]$$

and E is material stiffness, ρ is density, and v is Poisson's ratio.

In LS-Dyna, three options exist for the calculation of characteristic length.

Option 1:

$$L_s = \frac{(1+\beta)A_s}{\max(L_1, L_2, L_3, (1-\beta)L_4)} \quad [14]$$

where $\beta = 0$ for quadrilateral and $\beta = 1$ for triangular elements, A_s is the area and $L_i (i = 1, \dots, 4)$ are the lengths of the sides of the elements.

Option 2:

$$L_s = \frac{(1+\beta)A_s}{\max(D_1, D_2)} \quad [15]$$

where $D_i (i = 1,2)$ are the lengths of the diagonals of the element.

Option 3:

$$L_s = max\left[\frac{(1+\beta)A_s}{\max(L_1, L_2, L_3, (1-\beta)L_4)}, \min(L_1, L_2, L_3, L_4 + \beta 10^{20}\right] \quad [16]$$

will result in the largest time step (MSC, 2011:146).

Option 1 is the default option for shell elements, while option 2 is used when a more conservative or shorter characteristic length is desired. Option 2 can be used if the analyst is concerned about the stability of the solution when the characteristic length is calculated using option 1. However, choosing option 2 will result in higher computational expense and will

therefore not be used in this simulation. The use of option 3 is reserved for special cases where triangular shell elements with short altitudes are used. Based on this assessment, option 1 will be the preferred option for this study.

3.3 Time Step and Large Deformation

A further consideration when modelling problems where large structural deformation is likely to occur, is the change in time step as the mesh deforms. When the shape of an element changes, its characteristic length will change, and therefore its stable time step (MSC, 2011:295). This can dramatically increase CPU time due to decreased time step.

Some solvers, including SOL700, have a built-in capability to counteract changes in time step by adding numerical mass to elements. The user defines a minimum limit for the time step and the solver adds mass to elements to increase their time step if they reach the limit (MSC, 2011:127). This method is not recommended for problems where inertial effects are critical to the accuracy of the solution, such as crash simulations, and therefore will not be used in this study.

Another automated function for time step control is available in SOL700. In some material models, like MATD019 and MATD054, the user can activate a shell element deletion criterion that will delete elements that become so distorted that their time step decreases to below a specified limit (MSC, 2011:294). It is based on the assumption that severely distorted elements carry minimal load. Sound engineering judgement should be used in the application of this function.

The MSC Nastran 2012 Explicit Nonlinear User's Guide (MSC, 2011:118) advises that the user should monitor the time step regularly. If the time step decreases to the order of 1×10^{-8} s, the simulation should be terminated and the cause for the decreased time step investigated. The element that has the smallest time step at a particular time in the solution is identified in the solver output files.

3.4 Chapter Conclusion

It is clear from the investigations in this chapter that explicit solvers are generally preferred for crash simulation. The mathematical theory indicates that Δ_t plays a particularly important role in computational expense of an explicit solution. Furthermore, it was explained that Δ_t is limited in size by the CFL criterion. This criterion is related to the characteristic length of an element,

which in turn is a function of the dimensions of the element. The criterion also considers the speed of sound through an element as a function of its stiffness, density and Poisson's ratio.

Considering these aspects, the JS1 model will be computationally expensive compared to a metallic vehicle structure, for example. This statement is firstly related to its geometric complexity, which will require a fine mesh and result in a small characteristic length. Secondly, its construction materials with high weight-specific stiffness will result in a high speed of sound, which will decrease the size of Δ_t. Since the material properties cannot be changed, the mesh will be made as coarse as possible without compromising accuracy.

Methods to counteract time step related problems were discussed in the final section of the chapter. It was shown that solvers have various methods of dealing with time step deterioration. The first and most common method is the addition of numerical mass. This method is, however, not advised for simulations where inertial effects are present due to the resulting inaccuracy. Another method is to set a minimum limit for time step, which determines that an element will be deleted if its time step becomes less than the limit. Analysts are cautioned against the indiscriminate use of this method due to the potential effects on model accuracy. In the JS1 model, the second method will be applied conservatively, if needed.

Chapter 4 Model Preparation

The literature study has shown that finite element analysis, and more specifically explicit nonlinear FEA, is the preferred technique for crash simulation in similar research. Therefore, this technique will constitute the bulk of the framework of the research method. This chapter contains details about the preparation of the various finite element models used in the research. Details of the process followed to develop the research methodology are given in *Appendix A.*

For this study, tested properties of the JS1's construction materials and geometry of the fuselage were used as a foundation for the FE model. All other major aspects of the crash simulation were modelled after methods that have been successfully used in other research to achieve accurate results. Wherever a preferred method was impossible or impractical to implement, an assumption was made to counteract the expected inaccuracy. According to Fasanella and Jackson (2002), accurate simulations are achievable in the absence of crash test data by exercising the correct control over inputs and evaluating outputs.

4.1 MATD054 Material Definitions

Six composite materials are used in the construction of the JS1 cockpit. Each material consists of unidirectional or bidirectional fibre reinforcement, suspended in an epoxy matrix. The mechanical properties of these materials obtained from tests conducted by Naude (2008), are shown in *Table 2.*

Material	E_{11} (MPa)	E_{22} (MPa)	G_{12} (MPa)	v	σ_{11T} (MPa)	σ_{22T} (MPa)	σ_{11C} (MPa)	σ_{22C} (MPa)	τ_{12} (MPa)
Carbon UD	96000	8000	3000	0.2	890	50	500	170	48
Carbon BID	55000	55000	4000	0.08	525	525	400	400	25
Aramid UD	60000	5000	1500	0.34	600	50	232	50	40
Aramid BID	38000	38000	2200	0.15	400	400	120	120	50
Glass UD	32000	8000	3200	0.25	480	50	300	50	40
Glass BID	22500	22500	4200	0.28	223	223	180	180	60

Table 2: Mechanical properties of the construction materials used in the JS1 cockpit and surrounding structure (Naude, 2008:6).

where E_{11} is the modulus of elasticity in the 0° direction,

E_{22} is the modulus of elasticity in the 90° direction,

G_{12} is the shear modulus,

v is Poisson's ratio,

σ_{11T} is the ultimate stress in tension in the 0° direction,

σ_{11C} is the ultimate stress in compression in the 0° direction,

σ_{22T} is the ultimate stress in tension in the 90° direction,

σ_{22C} is the ultimate stress in compression in the 90° direction,

τ_{12} is the ultimate shear stress.

MATD054 is a Nastran model based on LS-Dyna material type 54. Examples of its successful use in similar research are discussed extensively in *Sections 2.2.2* and *2.2.3.* It has been selected for this study based on the accuracy demonstrated in these examples. The inputs required to define a material in MATD054 are listed in *Chapter 2* in *Table 1.* Some of the inputs used in the crash model were obtained directly from *Table 2* and are listed with their corresponding mechanical properties in *Table 3* below.

MATD054 input	**Mechanical property**
EA	E_{11}
EB	E_{22}
PRBA	v
GAB	G_{12}
XT	S_{11T}
XC	S_{11C}
YT	S_{22T}
YC	S_{22C}
SC	S_{12}

Table 3: Material model inputs and their corresponding mechanical properties.

Other inputs were calculated from the mechanical properties using the formulae recommended by Byar *et al.* (2011).

Firstly, DFAILT, described as the maximum strain for fibre tension, was calculated as follows:

$$DFAILT = e_{11T} = \frac{S_{11T}}{E_{11}} \quad [17]$$

DFAILC, or maximum strain for fibre compression, was similarly calculated as follows:

$$DFAILC = e_{11C} = \frac{S_{11C}}{E_{11}} \quad [18]$$

DFAILM, described as maximum matrix strain in tension or compression, was calculated as follows:

$$DFAILM = \max(e_{22T}, e_{22C}) \quad [19]$$

where strain in tension in the 90° direction is

$$e_{22T} = \frac{S_{22T}}{E_{22}} \quad [20]$$

and strain in compression in the 90° direction is

$$e_{22C} = \frac{S_{22C}}{E22} \quad [21]$$

DFAILS, or maximum shear strain, was calculated as:

$$DFAILS = \frac{S_{12}}{G_{12}} \quad [22]$$

All values were calculated as discussed above, except TFAIL, which was selected by trial and error during the initial fuselage crash simulations. TFAIL is a user-defined limit in MATD054 that determines the minimum time step of an element before it will be deleted. Its purpose is to prevent the infinite decay of Δt if, for some reason, an element deforms significantly without satisfying another failure criterion. Δt is the minimum time step of any element in the mesh. If the user selects a value for TFAIL that is in the same order of magnitude, but slightly smaller than Δt, the solver will prematurely delete elements as soon as they start to deform. This can result in underestimated energy absorption. On the other hand, if TFAIL is set to zero, Δt may decrease infinitely unless the element fails due to another criterion. In such cases, the

advancement of the solution in time becomes infinitesimal so that it must be manually terminated.

Feraboli *et al.* (2010) provide rough guidance on the selection of TFAIL. Their recommended range is $0 < TFAIL \leq \frac{\Delta t}{10}$. Therefore, for the purpose of this study, a minimum value for TFAIL of $\frac{\Delta t}{100}$ was selected. The method used by the solver to calculate time step (refer to *Chapter 3)* and the amount of element distortion required for Δt be reduced by two orders of magnitude were considered when this value was selected.

All calculated and selected values, together with those obtained directly from *Table 1* and *Table 2* are shown in *Table 4.*

Input parameter	Carbon UD	Carbon BID	Aramid UD	Aramid BID	Glass UD	Glass BID
EA*(kN/mm^2)*	96	55	60	38	32	22.5
EB*(kN/mm^2)*	8	55	5	38	8	22.5
PRBA	0.2	0.08	0.34	0.15	0.25	0.28
GAB*(kN/mm^2)*	3	4	1.5	2.2	3.2	4.2
GBC*(kN/mm^2)*	3	4	1.5	2.2	3.2	4.2
GCA*(kN/mm^2)*	3	4	1.5	2.2	3.2	4.2
DFAILM	0.02125	0.009545	0.01	0.010526	0.00625	0.009911
DFAILS	0.016	0.00625	0.026667	0.022727	0.0125	0.014286
TFAIL*(ms)*	1e-6	1e-6	1e-6	1e-6	1e-6	1e-6
ALPH	0.2	0.2	0.2	0.2	0.2	0.2
SOFT	1	1	1	1	1	1
FBRT	0.5	0.5	0.5	0.5	0.5	0.5
YCFAC	1.2	1.2	1.2	1.2	1.2	1.2
DFAILT	0.009271	0.009545	0.01	0.010526	0.015	0.009911
DFAILC	-0.00521	-0.00727	-0.00387	-0.00316	-0.00938	-0.008
EFS	0	0	0	0	0	0
XC*(kN/mm^2)*	0.5	0.4	0.232	0.12	0.3	0.18

XT *(kN/mm^2)*	0.89	0.525	0.6	0.4	0.48	0.223
YC *(kN/mm^2)*	0.17	0.4	0.05	0.12	0.05	0.18
YT *(kN/mm^2)*	0.05	0.525	0.05	0.4	0.05	0.223
SC *(kN/mm^2)*	0.048	0.025	0.04	0.05	0.04	0.06
CRIT	54	54	54	54	54	54

Table 4: MATD054 input parameters used in the JS1 crash model.

Each column in this table represents a full material definition in MATD054. These material definitions were used throughout the study in the single element simulations and in the full crash models.

4.2 Single Element Models

In order to ensure that accurate results would be obtained from the cockpit simulations later in the study, single elements were analysed for each of the material models. The single finite elements were subjected to tensile and compressive strain to failure in the 0° and 90° directions. These experiments formed part of the model accuracy control process, which is described in *Appendix A*. Their purpose was to ensure that the materials behaved and failed as intended when the material models were defined. This was done by comparing the simulated results to the experimental results measured by Naude (2008). Any incorrect behaviour was identified and corrected by adjusting the parameters within the ranges recommended by Byar *et al*. (2011).

The finite element model is shown in *Figure 21*. Its sides were 50 mm long and 50 mm wide. Nodes 1 and 2 were constrained using pinned constraints in the Z- and X-axis directions. This allowed the nodes to translate only in the Y-axis direction so that pure axial load in tension and compression was achieved. A single-layered composite shell property was applied to the element. Each of the six material models were applied to the property in consecutive simulations and strained in compression and tension to failure in the 0° and 90° directions.

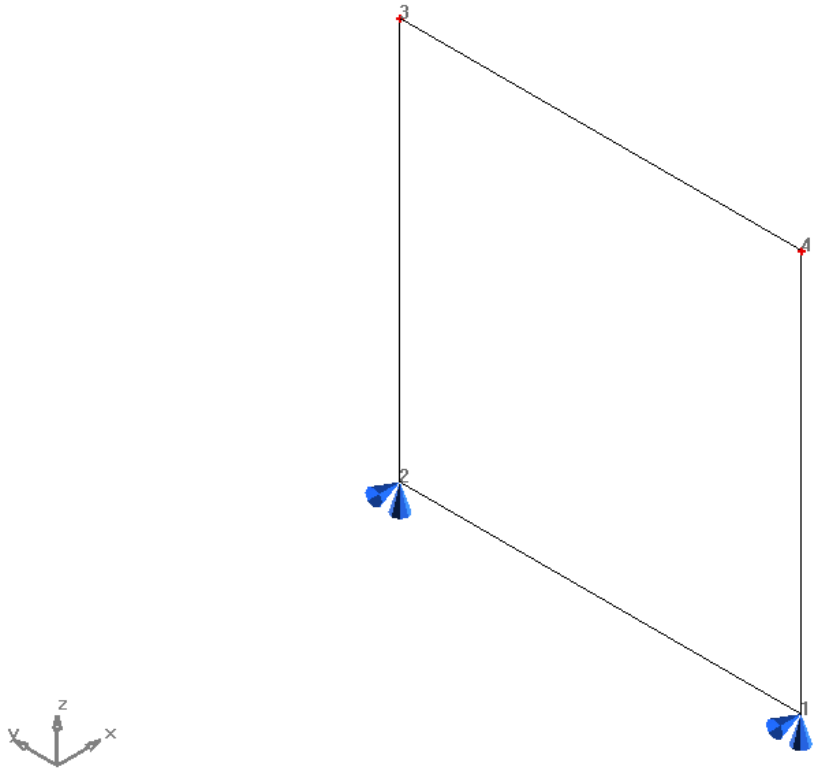

Figure 21: Finite element used to validate failure behaviour of material models defined for the JS1 crash simulation.

Positive strain was achieved by applying a small, but constant velocity to nodes 3 and 4 in the positive Z-axis direction, while negative strain was achieved by applying a similar velocity in the opposite direction. A velocity of 0.005 mm/ms was used so that quasi-static strain was simulated. This velocity was found to be irrelevant when the first test was repeated at 1 mm/ms, yielding the same result. This highlighted the inability of MATD054 to simulate strain rate sensitivity. Apart from the strain rate test, a total of 24 simulations were done for six materials using the single element model. The results are given in *Section 5.1.*

4.3 Crash Models

A finite element model of the JS1 cockpit was created for the initial crash simulations. This model also formed the base of the enhanced models, which are discussed in *Section 4.3.2* and *Appendix B*. The model was based on the mesh and material layout from an earlier linear static analysis of the JS1 done by Jonker (2012).

4.3.1 Initial Crash Model

Jonker modelled the fuselage in MSC Patran for analysis with the SOL101 solution sequence. The model consisted of 66 906 elements in 1825 parts; each part with a unique PCOMP layered composite property. These properties defined the thickness, stacking sequence, material orientation and material model of each of the lamina. An example of one of the PCOMP properties is given in *Figure 22* below.

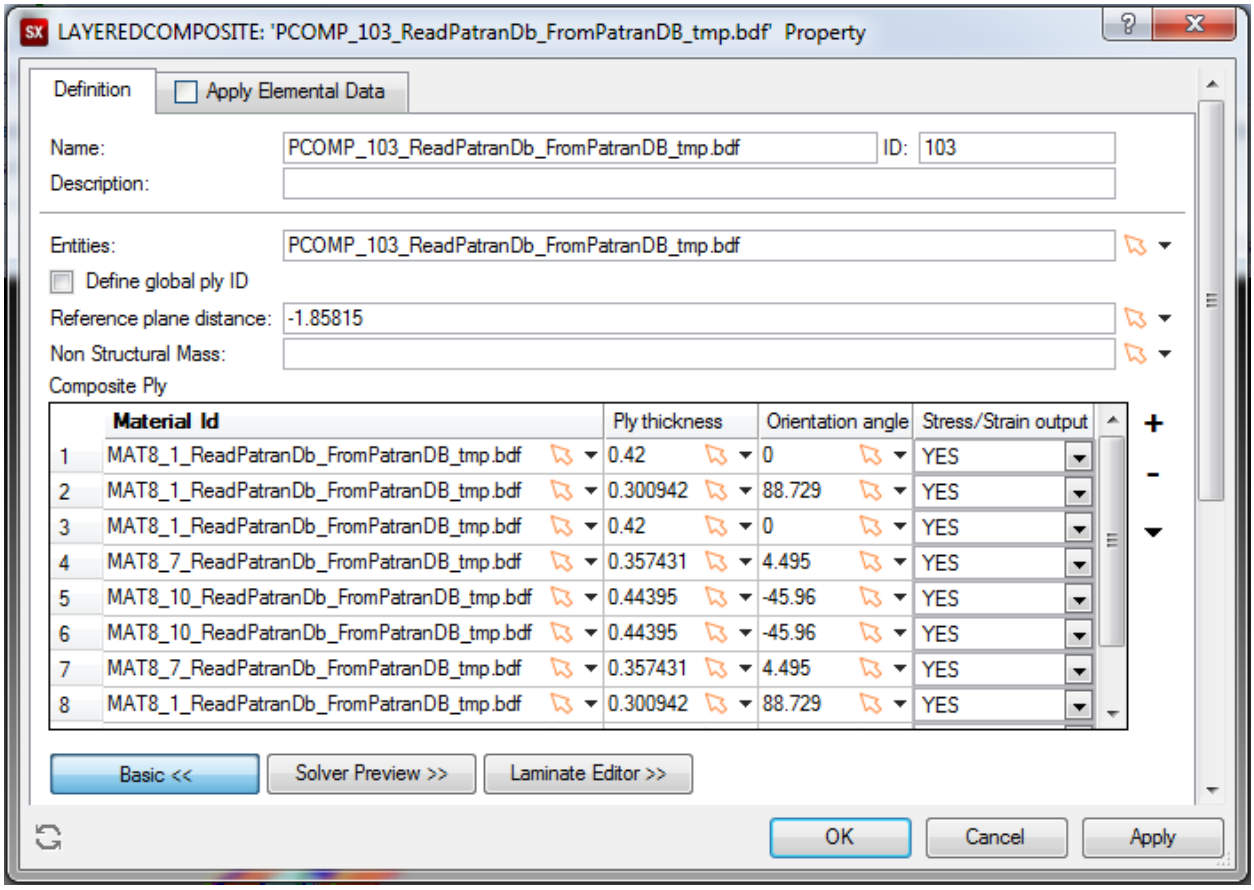

Figure 22: An example of a PCOMP layered composite property from Jonker's fuselage model.

Because the model was built for linear static analysis, some parts of the mesh were too fine for crash simulation. As discussed in *Chapter 3,* the element size has a direct influence on solution time, and generally a finer mesh results in longer solution times. The mesh was coarsened in areas where crushing was expected to occur to make it more computationally efficient for explicit analysis. This activity was able to reduce the initial solution time of 386 hours for a typical crash of 20 ms, to 36 hours. This was done in several stages by initiating the crash analysis, then identifying elements that caused time step deterioration and modifying them. The

coarsening feature in MSC SimXpert was also selectively used on parts with fine elements. It often resulted in poor mesh quality and was only used when manual techniques could not achieve the desired coarseness.

Since Jonker modelled the complete fuselage, the mesh was further modified for crash simulation to contain only the front 2.4m of the structure. To account for the remaining mass of the sailplane, 0-dimensional masses were placed at the centre of gravity. The model was constrained in such a way that results would be independent of moment of inertia (refer to subsequent paragraphs for details). The mesh used in the crash model is shown in *Figure 23.*

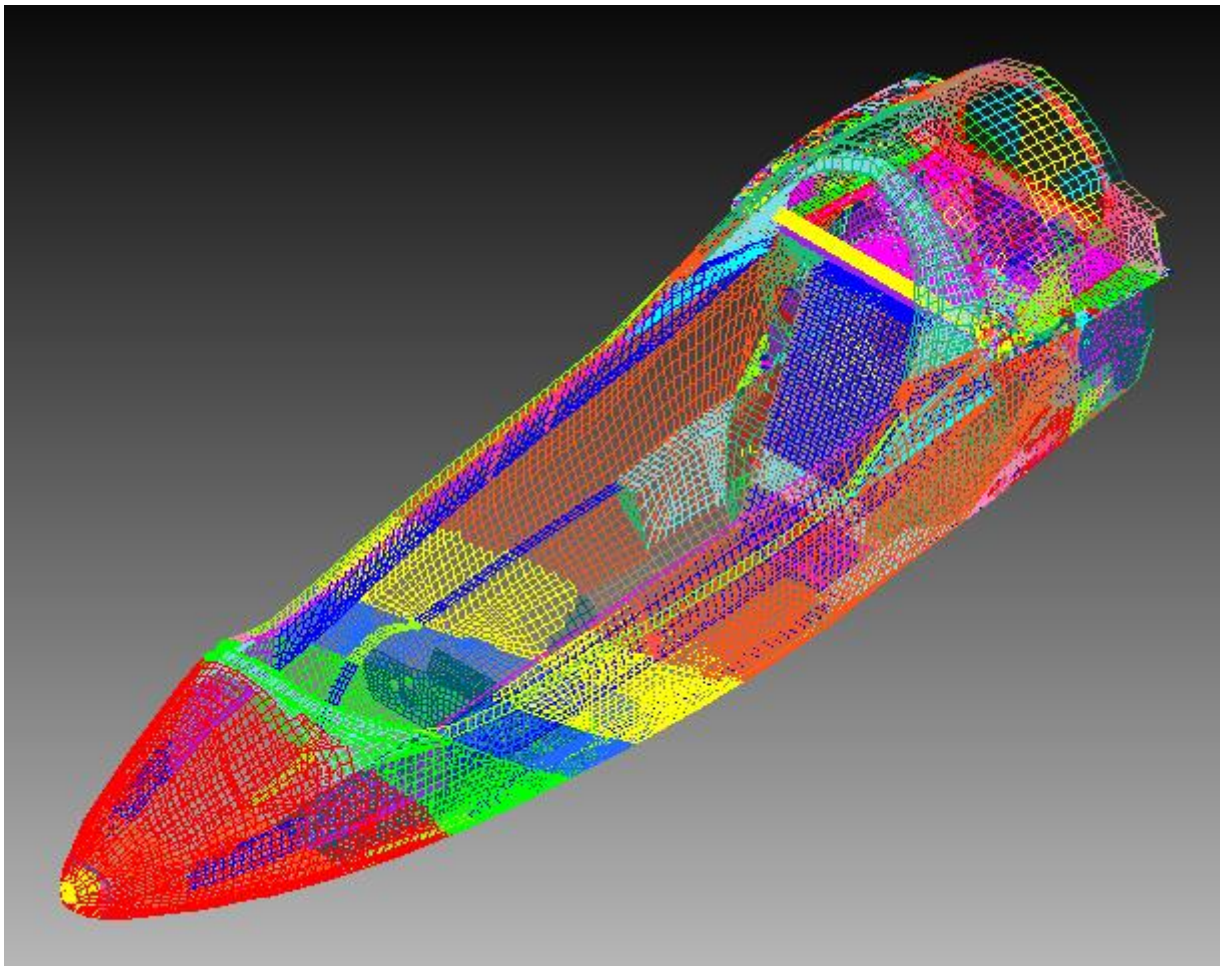

Figure 23: Finite element mesh of the JS1 cockpit used in initial crash simulations.

A total of 879 PCOMP properties were used to apply the material models to the various parts of the structure. The MAT8 orthotropic material models used by Jonker were substituted with the MATD054 models described in *4.1* and *4.2*. MATD054 was chosen for the crash simulations for its superior capability to model crushing behaviour as noted by Albertsen *et al.* (2008), Feraboli *et al.* (2010) and Byar *et al.* (2011).

Movement was simulated by applying a TIC3 initial transient condition to all nodes in the model. A translational velocity in the negative X-axis direction was applied so that the structure moved towards the rigid wall at the desired velocity. TIC3 was an initial condition applied at the start of the simulation, after which the structure was free to accelerate due to external forces. The initial velocity could be changed as needed when low or high velocity simulations were done.

A pinned constraint was applied to the nodes behind the bulkhead, separating the cockpit from the rest of the structure. The constraint forced those nodes to translate only in the X-axis direction, as would be observed in a physical crash test if the structure was attached to a rail-bound carriage. This control measure was implemented to prevent the structure from rotating upwards due to the reaction force of the wall, which was angled at 45° to the horizontal.

Figure 24a shows the movement of an unconstrained JS1 cockpit crashing into a wall sloped at 45°. Note how the cockpit began to rotate upwards in the final image in the timeline. This reaction is undesirable when comparing structures with dissimilar stiffness or inertial properties, since the rotation will influence energy absorption. On the other hand, *Figure 24b* shows results from the same model with nodes constrained as described above. In this case, energy absorption occurs only through crushing of the materials, producing force displacement results which are independent of moment of inertia. Furthermore, if desired, the conditions can be reproduced repeatedly in a physical crash test using the same controls. For that reason, this constraint was used in all the JS1 initial and enhanced models.

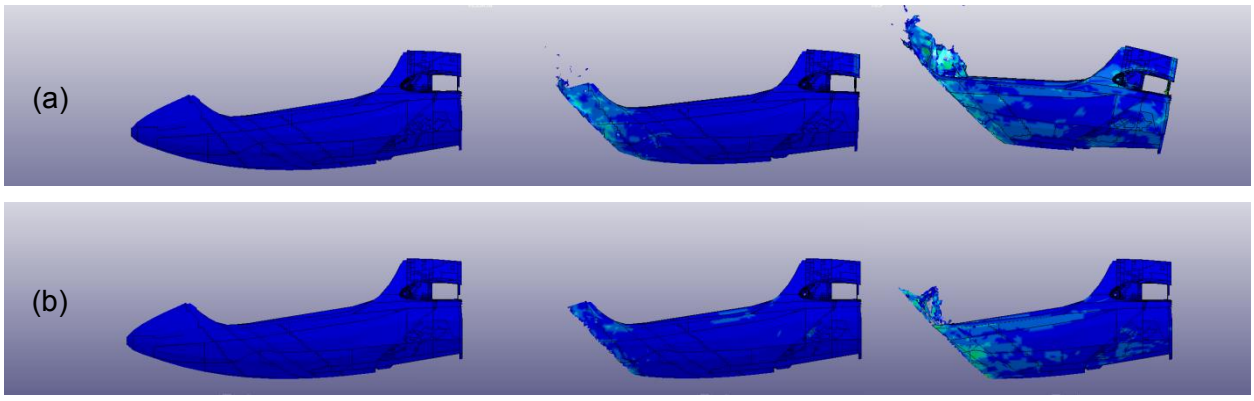

Figure 24: **(a) Timeline of an unconstrained JS1 cockpit crashing into an sloped wall and (b) timeline of a similar crash with nodes at the wing mounting constrained to translate only in the forward direction.**

A wall was initially modelled using finite elements with a shell property and rigid material model. The nodes of the wall were constrained by a fixed constraint. Even though this approach

produced good results in terms of contact, wall reaction forces were cumbersome to obtain. To overcome this problem, the wall was modelled using the planar rigid wall feature in MSC SimXpert. This approach allows the user to define an infinite plane through which specific nodes cannot pass. The applicable nodes are defined in a BCGRID group and wall reaction forces can be obtained from the binary output file.

The orientation of the wall relative to the longitudinal axis of the sailplane was chosen in accordance with paragraph 22.561(b)(2) in EASA CS-22 amendment 2. This paragraph specifies the angle at which a static load of 9 times the maximum weight of the sailplane must be applied without causing the structure to collapse. The load direction is defined as “rearwards and upwards at an angle of 45° to the longitudinal axis of the sailplane and sideward at an angle of 5°...at a suitable point not behind the pedals”.

Contact definition for the rest of the structure was done through a single deformable contact surface containing all parts in the model. This was entered into a BCTABLE, which defined touching contact between all parts. The search algorithm was set to full regular contact and all other contact settings were left on solver defaults.

As discussed in *Chapter 2,* the SOL700 solution sequence uses the LS-DYNA solver for structural analysis. For this reason most of the inputs required to control the solution are LS-DYNA commands. Details of LS-DYNA parameters and their functions are given below.

The DYTIMHS time history output request was used to activate the following outputs:

- GLSTAT at 0.001 ms intervals to capture global energy data such as kinetic energy, internal energy, hourglass energy, sliding interface energy and time step.
- RWFORC at 0.1 ms intervals for rigid wall reaction forces.

DYPARAM LSDYNA DBEXTENT was used to set the following LS-DYNA parameters:

- STRFLG = 1 to dump strain tensors at the innermost and outermost integration points of shell elements.
- CMPFLG = 1 to output material stress and strain data in the local material coordinate system.
- STSSZ = 1 to deactivate the output of individual shell element time step, mass and added mass data. This was done to reduce the size of the output file.
- SHGE = 2 to activate the output of shell hourglass energy density. This is done so that hourglass energy issues (i.e. when hourglass energy is more than 10% of internal

energy) can be diagnosed by creating a fringe plot of the hourglass energy density in LS-PREPOST.

DYPARAM LSDYNA HOURGLAS was used to set the following LS-DYNA parameters:

- IHQ = 1 to activate standard hourglass energy dissipation.
- QH = 0.05 to set the hourglass coefficient.

DYPARAM LSDYNA SHELL was used to set the following LS-DYNA parameters:

- THEORY = 1 to select the Hughes-Liu shell formulation. This formulation is more computationally expensive than the popular Belytschko-Tsai formulation, but is very effective in large deformation problems (DuBois *et al.*, 2013:14).

SOL700 solution parameters were controlled by selecting PATH = 3 as the execution file path and placing the sol700.pth script file in the working directory containing the text given in *Table 5*

Sol700.pth instruction	**Meaning of instruction**
D:\MSC.Software\SimXpert\2012.0.1\dyna\win64/run_dytran.bat	Defines the path to the executable file
intelmpi=yes	Indicates that Intel MPI cluster messaging is activated
nproc=4	Defines the number of processors to be used for solution
memory=800000000	Allocates memory to each processor, measured in words

Table 5: Options used in the sol700.pth file for the JS1 crash simulation.

Finally, in the load case control for the simulation, the ending time was set to 1000 ms and the time increment for outputs was set to 0.1 ms. Since the solution would only terminate automatically at 1000 ms, solutions were monitored until the required results were produced, and then manually terminated.

4.3.2 Enhanced Crash Models

Twelve enhanced variants of the initial crash model were developed. These models were used to determine the effectiveness of various concepts of improvements to the crashworthiness of

the cockpit. All the enhanced models were identical to the initial model, apart from the changes detailed in *Appendix B.*

As opposed to the initial crash model, which contained only shell elements, some of the new models contained 3-dimensional brick elements to model a honeycomb layer in the energy absorber in *Figure 25*. The honeycomb was modelled by applying a PSOLIDD property specification with MATD063 material model to the brick elements. Since this is an isotropic material model, the simulated behaviour was expected to be closer to that of a foam, rather than a true honeycomb. The inputs for the honeycomb model where obtained from *Table 10,* which was extracted from the Guide to Hexcel® Honeycomb Materials (Hexcel, 1999:16).

The first 10 enhancements consisted of various combinations of the frontal energy absorber with aluminium honeycomb core shown below and changes to the stiffness of the remaining cockpit structure. Full details of each of the enhanced models are given in *5.3* and *Appendix B.*

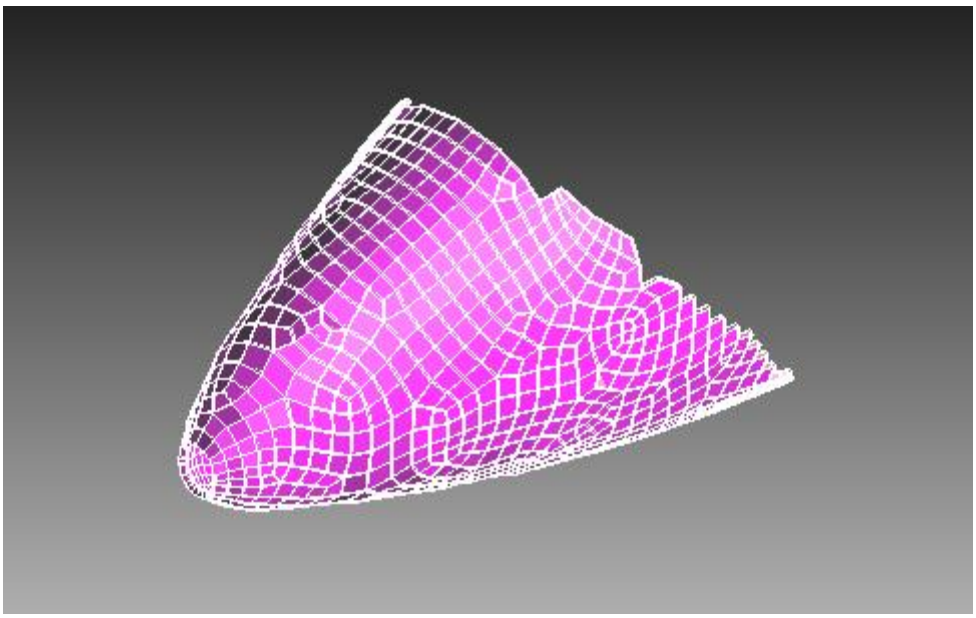

Figure 25: Concept energy absorber with sandwich construction and aluminium honeycomb core.

The initial enhanced models were prone to early termination due to a poorly defined stress strain curve for the honeycomb material model. The user-defined curve was defined such that the material offered no resistance after full compaction was reached. This led to negative volumes due to unphysical deformation of brick elements. The problem was corrected by maintaining the material's crush strength at full compaction.

Two further enhancement models, NC12 and NC13, were constructed using only fibre-composite materials rather than honeycomb. These models were created to compare the performance of fibre-composite concept energy absorbers to honeycomb absorbers. An example of one of the absorbers is shown in *Figure 26.* An analysis of the construction materials used in the JS1 was done to determine the most suitable material for an energy absorber.

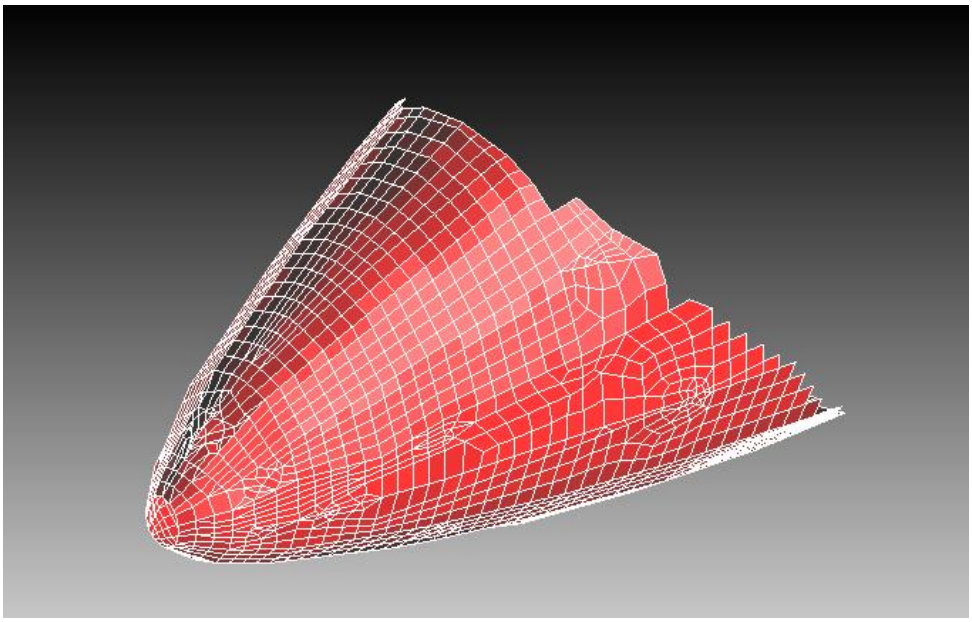

Figure 26: Concept energy absorber with carbon fibre construction.

The first criterion was that the material had to be bidirectional rather than unidirectional due to the random nature of strain direction during crushing. Therefore, carbon BID, aramid BID and glass BID were assessed. Since energy absorption per unit volume is represented by the area under the stress strain curve, *Equation 23* was used to calculate this characteristic. Note that $\boldsymbol{e_{11T}}$ was calculated using *Equation 17*. Since the stress strain curves are linear until failure (refer to *Figures 31 to 42),* the area under the curve is triangular and therefore given by:

$$W_v = \frac{1}{2}(\sigma_{11T} \times e_{11T}) \quad [23]$$

Material	σ_{11T} (MPa)	e_{11T} (m/m)	W_v (MJ/m^3)
Carbon BID	525	0.0095	2.5
Aramid BID	400	0.0105	2.1
Glass BID	223	0.0099	1.1

Table 6: Tensile energy absorption per unit volume of the bidirectional construction materials of the JS1.

Based on this analysis, bidirectional carbon fibre was selected as the preferred material for the construction of the energy absorbers. The absorbers were created by increasing the thickness of existing carbon fibre layers in the nose of the JS1 to increase stiffness. Similar to earlier enhancement models, the remaining structure was stiffened correspondingly to be able to withstand the increased loading during a crash. Details of the enhancements made in NC12 and NC13 are given in *Table 12.*

4.4 Quantifying Crashworthiness

A measure of crashworthiness was formulated to compare the original JS1 structure to enhanced models. The measure was based on the principals of crashworthy design, namely to maintain a safe volume around the occupant (EASA, 2009:5) and to limit accelerations imparted to occupants through energy absorption during a crash (Peng *et al.*, 2011:286). In order to quantify the first principle, a simple pass or fail criteria was used. If the main structure of the cockpit failed during a crash, it failed the collapse test. In such instances, energy absorption results were disallowed since the structure failed to protect the occupant in terms of the first principle of crashworthiness.

An example of a simulation during which the collapse test failed is given in *Figure 27a.* Note the encircled buckling failure of the longitudinal beams on either side of the cockpit. *Figure 27b* shows an example of a simulation that passed the collapse test. In this case the occupied volume remained unaffected while the nose yielded as required in a crashworthy design.

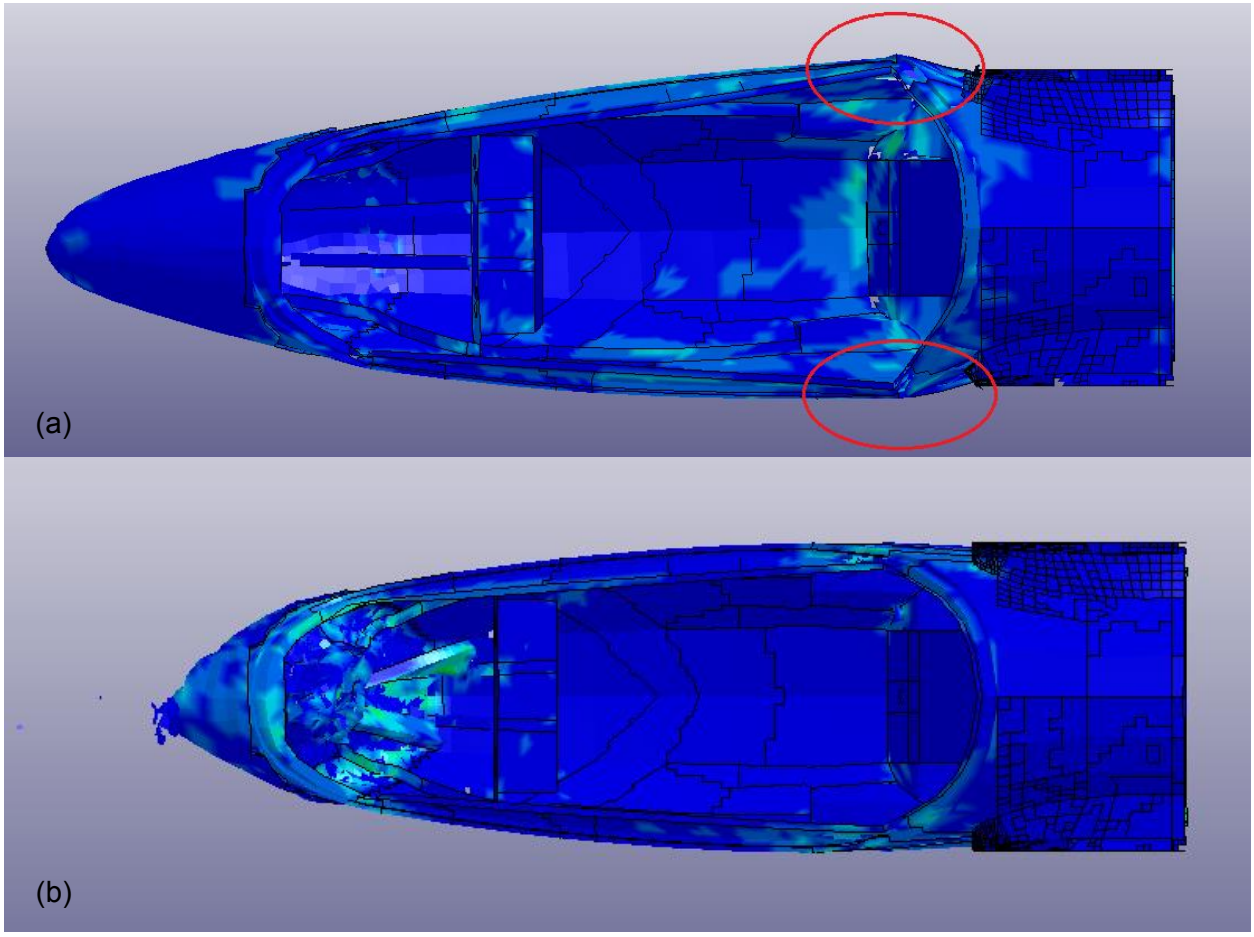

Figure 27: **Top view of the JS1 cockpit model showing examples of (a) a cockpit failing the collapse test and (b) a cockpit passing the collapse test.**

To measure the performance in terms of the second principle, the energy absorption (*W*) during the first 515 mm of crushing was calculated so that specific energy absorption could be calculated (refer to *Equations 24* and *25*). This distance was based on the maximum allowable deformation of the nose without reducing the occupied volume. Note that the occupied volume was determined with the pilot's legs in a retracted position. The allowable distance is shown in *Figure 28.*

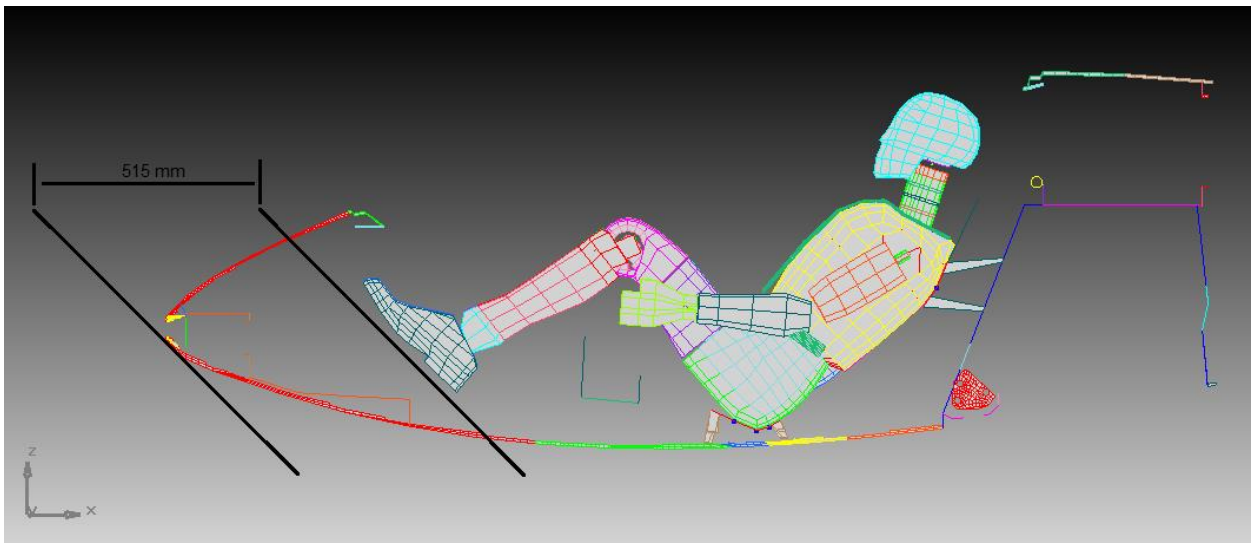

Figure 28: Maximum allowable deformation when the pilot's legs are in a retracted position.

Two different methods were used to calculate the specific energy absorption during each crash. The first, conventional approach was to divide the energy absorption by the mass of the deformed material. This provided valuable insight into the local effectiveness of the material used as an energy absorber, but failed to capture the performance of the system as a whole.

For example, one aluminium honeycomb material performed exceptionally well as an energy absorber in the nose of the JS1 model when the rest of the cockpit was stiffened. The stiffening, however, increased the total weight of the structure. In this case, when the nose of the aircraft was considered as an independent energy absorber, its weight-specific performance was exceptional. On the other hand, when the mass increase due to stiffening of the remaining structure was brought into consideration, the weight-specific performance decreased significantly.

Equations 24 and *25* show the two different methods used to calculate specific energy absorption. To distinguish between the two methods, they have been called specific energy absorption (*SEA*) and system-specific energy absorption (*SSEA*).

If:

W is energy absorption

m is the mass of deformed material

m_o is the mass of the original structure

m_e is the mass of the enhanced structure

Then

$$SEA = \frac{W}{m} \quad [24]$$

and

$$SSEA = \frac{W}{m_e - m_o} \quad [25]$$

It is clear from the calculation that *SEA* can be used to determine the performance of the energy absorber, while *SSEA* can be used to determine the performance of the energy absorption system as a whole.

4.5 Square Crash Box Model

A simulation of a mass drop test was done and compared to experimental results. This was done to determine the degree of accuracy that could be achieved using the modelling methods employed in the JS1 crash model. The simulation is a replication of the experiment described by Albertsen *et al.* (2008). The specimen is a 150mm long tube having a square cross section with 50mm width and 2.4mm wall thickness. A 200kg impactor moving at 10.3m/s crushed the component while crash load and impactor displacement were measured. The specimen dimensions are given in *Figure 29a* and the mass-drop experiment is shown in *Figure 29b.*

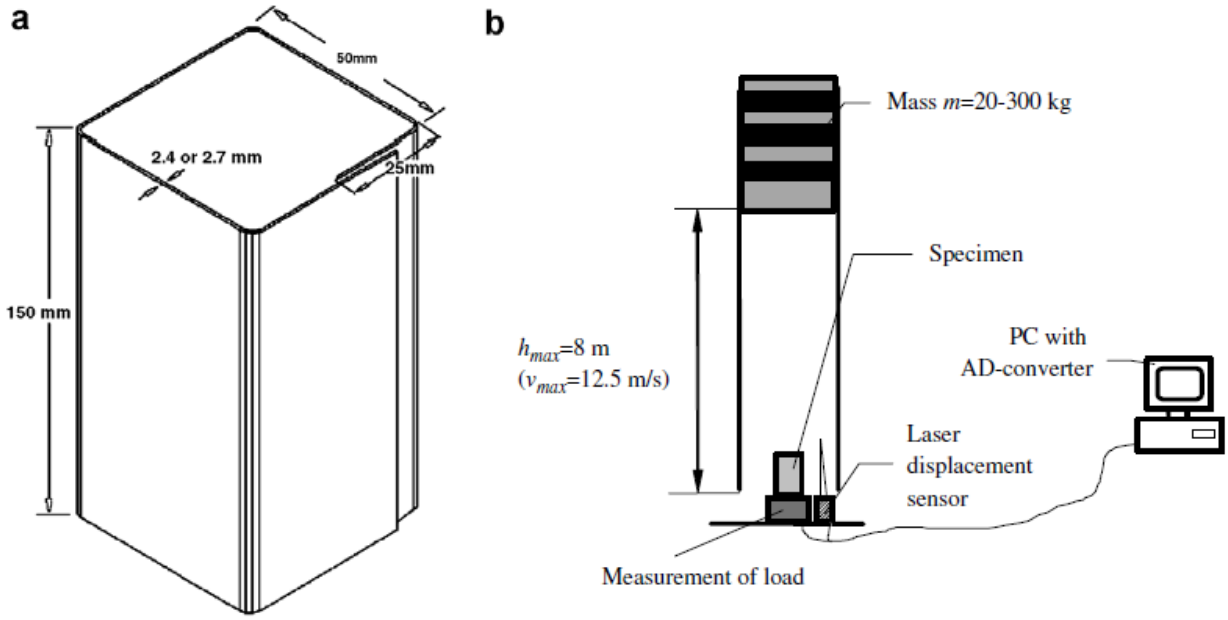

Figure 29: (a) Square crash box and (b) mass-drop test arrangement (Albertsen *et al.,* 2008:247)

A finite element model of the specimen and impactor (shown in *Figure 30*) was built in SimXpert. Similar to the JS1 model, the material was defined in MATD054. All input parameters given in *Table 7* below were derived from mechanical properties using the formulae in *Section 4.1*. Where possible, all other aspects and settings of the model were based on those used in the JS1 crash model described in *Section 4.3*.

Input parameter	Carbon UD
EA*(kN/mm²)*	22.4
EB*(kN/mm²)*	21.5

PRBA	0.17
GAB*(kN/mm^2)*	4.2
GBC*(kN/mm^2)*	4.2
GCA*(kN/mm^2)*	4.2
DFAILM	0.022
DFAILS	0.01429
TFAIL*(ms)*	0
ALPH	0.2
SOFT	1
FBRT	0.5
YCFAC	1.2
DFAILT	0.018036
DFAILC	-0.01456
EFS	0
XC*(kN/mm^2)*	0.325
XT*(kN/mm^2)*	0.4
YC*(kN/mm^2)*	0.315
YT*(kN/mm^2)*	0.39
SC*(kN/mm^2)*	0.06
CRIT	54

Table 7: MATD054 input parameters used in square crash box model.

The accuracy of the results obtained from this model is therefore assumed to be representative of the accuracy of the JS1 crash model. Based on the findings of Albertsen *et al.,* energy absorption is expected to be underestimated by the finite element model due to its inability to model inter- and intra-laminar failure behaviour such as delamination.

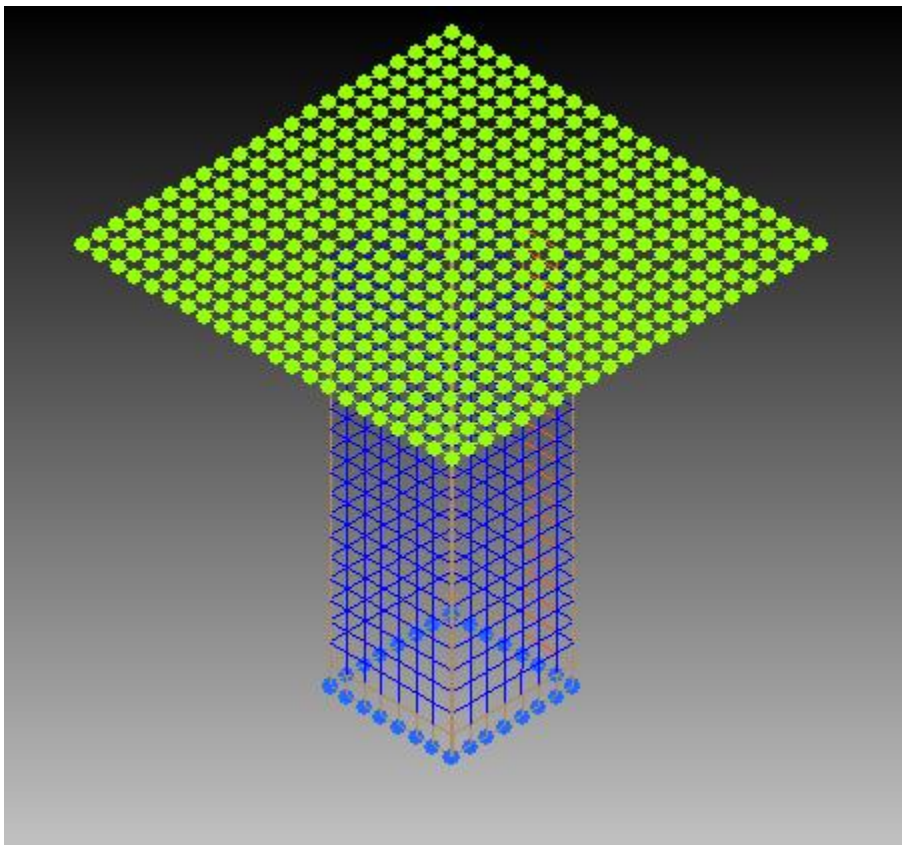

Figure 30: Finite element model of the square crash box experiment.

The corresponding FEM features of the square crash box model and those of the JS1 crash model include:

- Shell element formulation
- Hourglass control type
- Hourglass coefficient
- Layered composite property
- Material model
- Contact definition
- Initial transient condition
- Constraints
- Crash load measurement using planar rigid wall

4.6 Chapter Conclusion

The chapter provided the details of the various finite element models used in the study. Modelling methodology was based on industry best practice where applicable, and conservative

assumptions in some instances. Several steps were included in this phase to control the quality of inputs used in the finite element models and to ensure the accuracy of results.

In order to confirm that material definitions behaved and failed as required in the simulations, single-element models were built to be loaded in pure axial tension and compression. These models were then applied to the full crash model, which was based on an earlier model built for static analysis. Twelve variants of this structure were then modelled. The purpose of these structures was to determine the relative improvement in crashworthiness, which could be attained through the implementation of a simple energy absorber.

A methodology was also developed to enable the consistent comparison of simulation results in terms of crashworthiness. The aim of the methodology is to provide results that can be used to rank the performance of energy absorbers based on finite element simulations or experimental data.

In the final section of the chapter, a model was described that was used to determine the accuracy of simulated results. The major aspects of this model were similar to those of the JS1 model and results are therefore assumed to be representative of the accuracy of the JS1 results. Detailed results and a comparison to experimental results are given in the next two chapters.

Chapter 5 Validation of Modelling Techniques

This chapter contains the results of the single element and square crash box models described in *Chapter 4.* Their simulated results were compared to experimental results recorded by Naude (2008) and Albertsen *et al.* (2008). These comparisons formed part of the model quality control process that is shown in the research methodology in *Appendix A*.

5.1 Single Element Simulations

The stress displacement results for each simulation are given in the following subsections. Compressive and tensile stress in each material are plotted against strain on a single set of axes to represent the behaviour of the material across the entire load spectrum.

5.1.1 Unidirectional Carbon Fibre

A composite shell property with carbon UD material model from *Table 4* was applied to the single element described above. The element was strained to failure in tension in the 0° direction, and again in compression. The stress strain relationships for both simulations are shown in *Figure 31.*

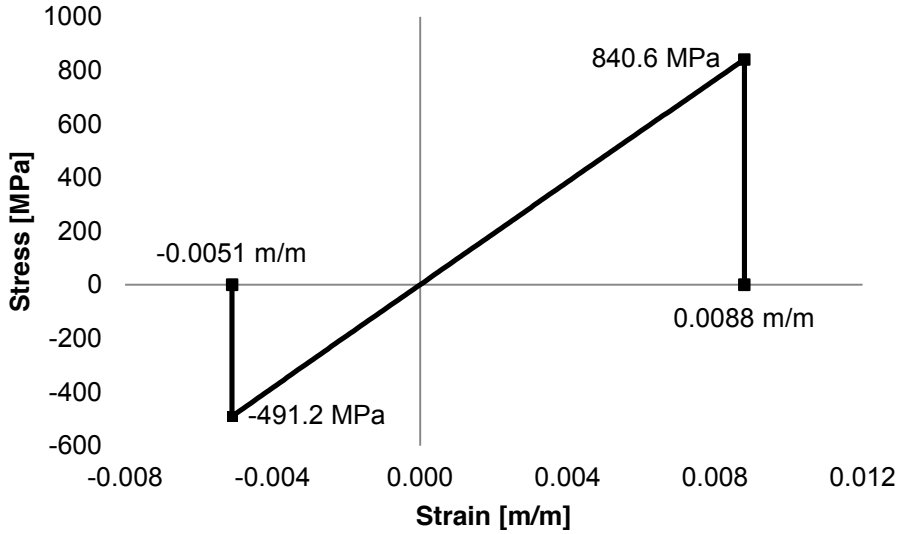

Figure 31: Simulated stress strain behaviour of unidirectional carbon fibre reinforced epoxy loaded in compression and tension in the 0° axis direction.

The element failed in tension at 840.6 MPa and 0.0088 m/m. Since XT was set at 890 MPa (0.89 kN/mm^2), and DFAILT was set at 0.00927 m/m it is clear that either, or both of these criteria caused the element to fail. The results further confirm the correct definition of material stiffness since the ratio of stress to strain at failure is 95.5 x 10^9, which correctly represents the modulus of elasticity defined by EA. In compression, it can be seen that failure was caused by XC, which was set at 500 MPa.

The shell property was modified so that the main material axis was perpendicular to the applied load. The results are shown in *Figure 32.*

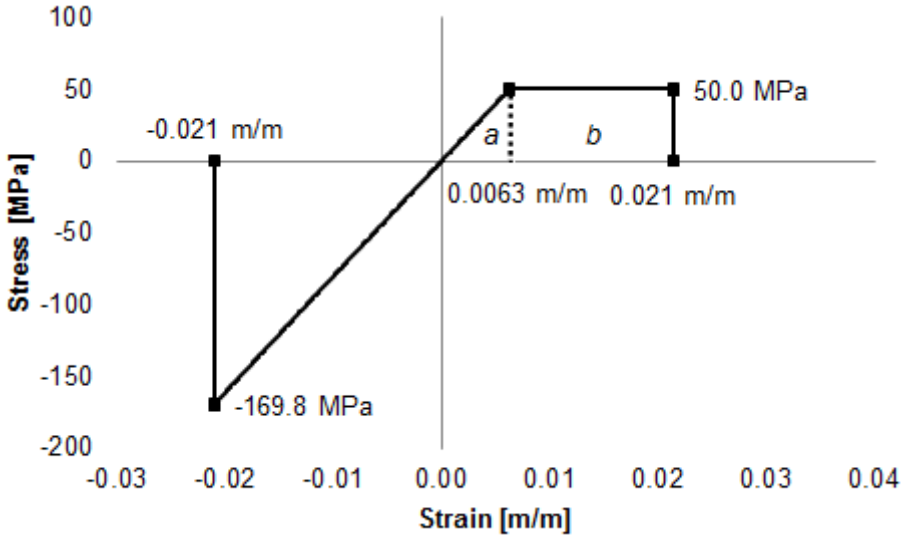

Figure 32: **Simulated stress-strain behaviour of unidirectional carbon fibre reinforced epoxy loaded in compression and tension in the 90° axis direction.**

Stress in tension was limited to 50 MPa by YT and strain was limited by DFAILM. The flattened shape of the curve on the right hand side of *Figure 32* highlights a deficiency of MATD054. Since DFAILM represents the maximum strain in tension or compression in the 90° direction, it is calculated using either YT or YC, whichever is greater. Because YC was greater in this case, it dictated maximum strain in both tension and compression. The element continued to strain until DFAILM was reached, even though YT had been reached. The stress was limited at YT for the remaining strain until it ultimately failed when DFAILM was reached. Since energy absorption is represented by the area under the curve, it is vastly overestimated in such instances.

If *a* and *b* in *Figure 32* represent the area under the curve, the ratio between simulated and expected energy absorption is:

$$\frac{a+b}{a} = 5.7 \quad [26]$$

This means that energy absorption at tensile failure for this material in the 0° direction will be overestimated by a factor of 5.7. A similar error appeared in three more out of twenty-four experiments (see *Figures 34, 38 and 42*). This does not mean that energy absorption in the crash simulation was similarly overestimated. A small proportion of possible material behaviour is represented by this error. It will only occur in an element if the problematic material model is present in one of the layers. Furthermore, load would have to be present in the specific material axis and applied in the specific direction (tensile or compressive), and be large enough to strain the material beyond its initial linear region. Its effect in the simulation is therefore assumed to be negligible. Nevertheless, the failure of random elements containing these erroneous models will be monitored during later simulations as a control measure.

Even though this effect is negligible for the JS1 model, it is still a deficiency in MATD054. Since the parameter DFAILM controls both tensile and compressive failure in the transverse material axis, an error will always be present unless both strains are identical. If the two strains are unique and DFAILM is set to the greater of the two strains, energy absorption will be overestimated. If DFAILM is set to the lesser strain, energy absorption will be underestimated. Alternatively, an average value can be selected to counteract the inaccuracy if the problem at hand is not expected to be biased towards tensile or compressive load.

5.1.2 Bidirectional Carbon Fibre

The experiment explained in 5.2.1 was repeated for an element with a bidirectional carbon fibre material property. Details of the material model are given in *Table 4.*

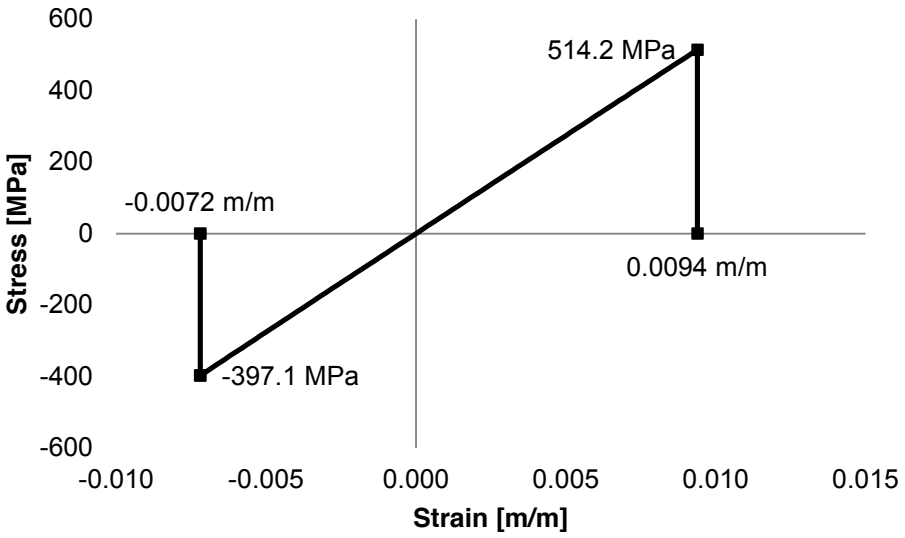

Figure 33: Simulated stress strain behaviour of bidirectional carbon fibre reinforced epoxy loaded in compression and tension in the 0° axis direction.

For compressive strain, DFAILC was set to 0.00727 and XC was set to 400. Both stress and strain at failure were found to occur within 1% of the expected value. Similarly, for tensile strain, DFAILT was set to 0.009545 and XT was set to 525. Both observed values were found to be within 2% of the expected values.

Note here the effect of the ability to define unique values in MATD054 for maximum strain in compression and tension. This is only possible in the 0° material axis and allows the user to accurately model the desired material behaviour. As opposed to the problem explained in 5.2.1, a flattened stress strain curve was not observed in this experiment.

The material orientation was changed so that the main material axis was perpendicular to the applied load. The results are shown in *Figure 34.*

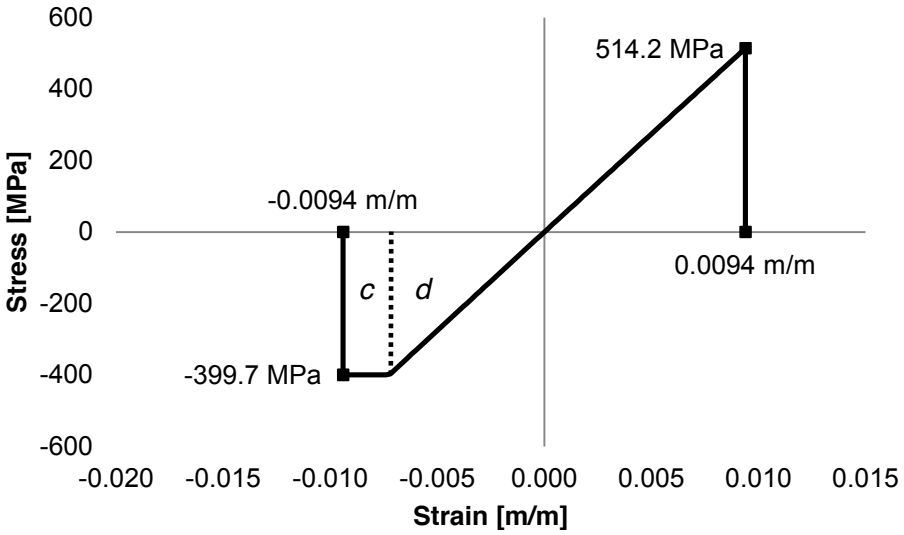

Figure 34: Simulated stress strain behaviour of bidirectional carbon fibre reinforced epoxy loaded in compression and tension in the 90° axis direction.

In this instance, a similar but opposite error to the one shown in *Figure 32* was observed. The reason that it occurred under compressive rather than tensile load, is that DFAILM was calculated from YT, since it was larger than YC. According to the formulation of MATD054, an element will strain in compression until YC is reached and continue to strain if this point does not coincide with DFAILM. The load, however, is limited to YC until failure occurs when DFAILM is reached.

The resulting overestimation of energy absorption is represented by the ratio between the expected and obtained areas under the curve, which is calculated as follows:

$$\frac{c+d}{d} = 2.17 \qquad [27]$$

Similar to the error encountered in the test with unidirectional carbon fibre, this result is not a major concern in terms of model accuracy. It will be monitored and treated in the same way as unidirectional carbon fibre so that the effect of the error is known and can be accounted for if necessary.

5.1.3 Unidirectional Aramid Fibre

Failure for unidirectional aramid fibre loaded in the 0° direction was expected to occur in tension at 600 MPa and 0.01 m/m. In compression, the material model was defined so that failure would occur at 228.4 MPa and 0.0038 m/m. The result from the single element simulations in tension

and compression are shown in *Figure 35.* These results confirm the correct definition of the material model in the 0° direction.

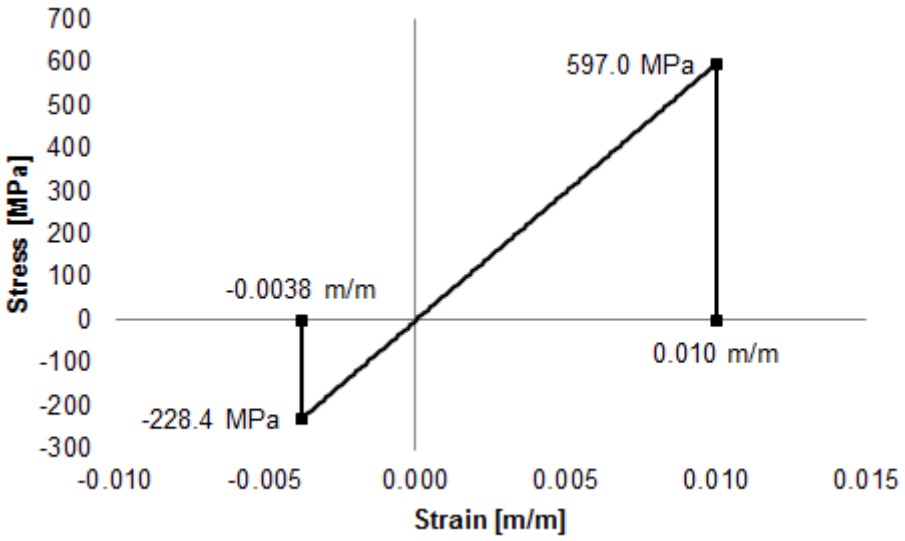

Figure 35: **Simulated stress strain behaviour of unidirectional aramid fibre reinforced epoxy loaded in compression and tension in the 0° axis direction.**

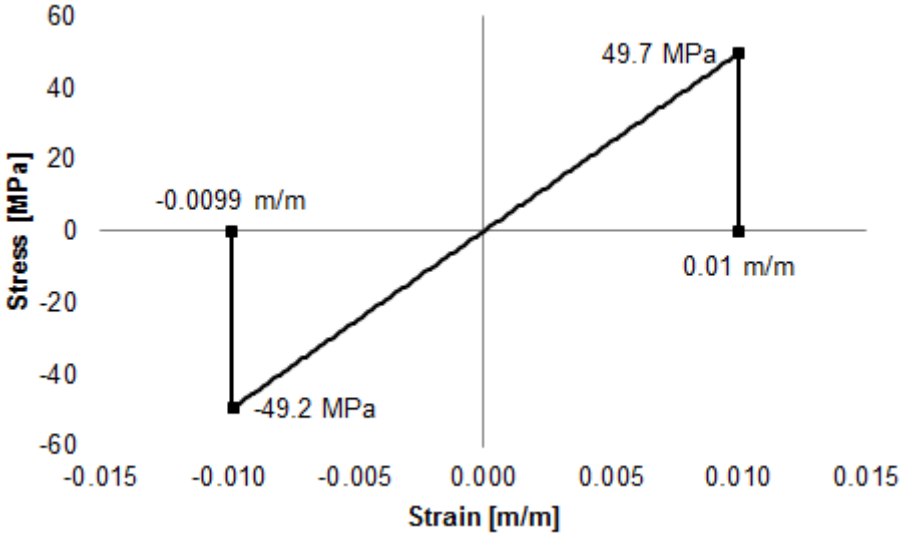

Figure 36: **Simulated stress strain behaviour of unidirectional aramid fibre reinforced epoxy loaded in compression and tension in the 90° axis direction.**

The tests were repeated in the 90° direction and results are shown in *Figure 36.* Failure under tension and compression occurred as intended at 50 MPa and 0.01 m/m.

5.1.4 Bidirectional Aramid Fibre

The next simulation was for bidirectional aramid fibre in the 0° material direction. According to the values in *Table 4,* failure would occur at 400 MPa and 0.0105 m/m in tension, and at 120 MPa and 0.00316 m/m in compression. The results shown in *Figure 37* confirm the correct definition of this material model.

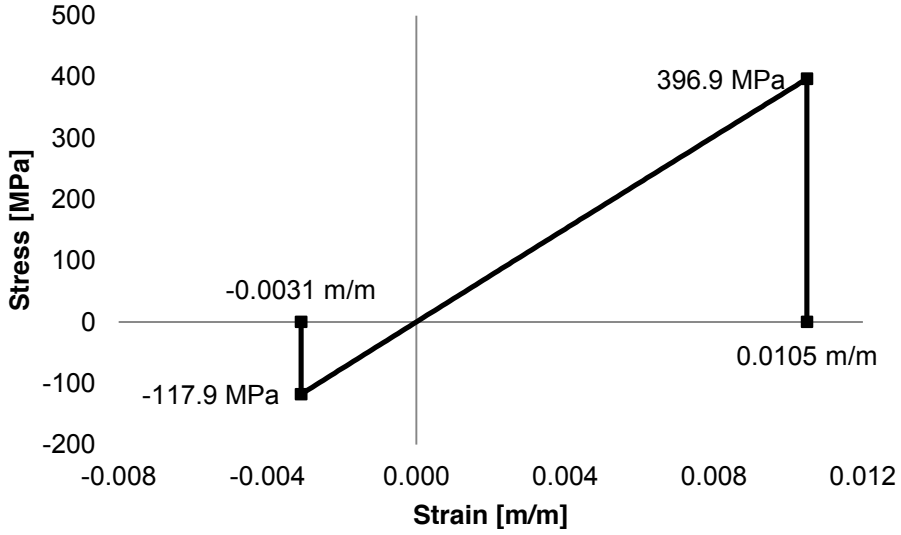

Figure 37: Simulated stress strain behaviour of bidirectional aramid fibre reinforced epoxy loaded in compression and tension in the 0° axis direction.

The results in *Figure 38* show that an error was encountered in the 90° direction for the same material. The error was similar in nature to earlier errors due to DFAILM. Based on the test results of Naude (2008), the material should fail at 0.00316 m/m strain. Due to the lack of separate definitions for failure strain in compression and tension in the 90° direction, only the largest strain could be selected. Therefore, failure in compression occurred at 0.0105 m/m instead of the expected 0.00316 m/m.

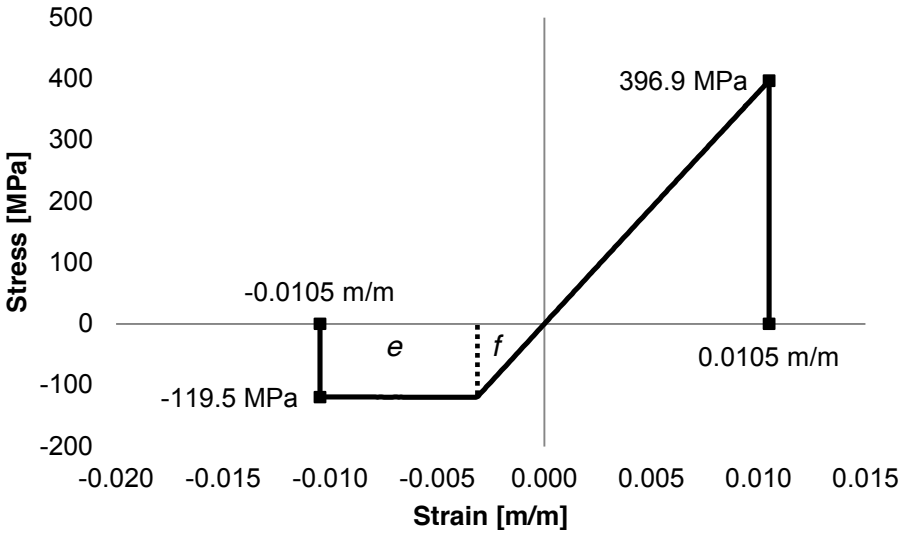

Figure 38: Simulated stress strain behaviour of bidirectional aramid fibre reinforced epoxy loaded in compression and tension in the 90° axis direction.

If the areas under the curve are expressed by *e* and *f,* the resulting error is quantified as follows:

$$\frac{e+f}{f} = 4.65 \qquad [28]$$

Similar to earlier errors, this was of little concern and was monitored during subsequent simulations. In tension in the 90° direction, the material behaved as expected, failing at 400MPa and 0.0105 m/m as defined by YT and DFAILM respectively in *Table 4.*

5.1.5 Unidirectional Glass Fibre

The simulation results for unidirectional glass fibre are shown in *Figure 39.* The material behaved as expected under tensile and compressive load in the 0° direction. As per *Table 4,* the model was defined to fail at 480 MPa and 0.015 m/m in tension, and 300 MPa and 0.0093 m/m in compression.

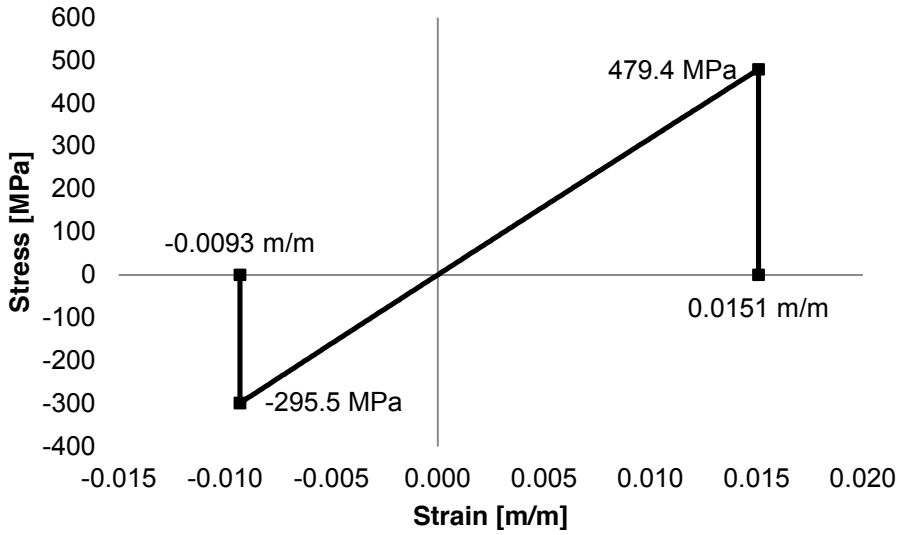

Figure 39: **Simulated stress strain behaviour of unidirectional glass fibre reinforced epoxy loaded in compression and tension in the 0° axis direction.**

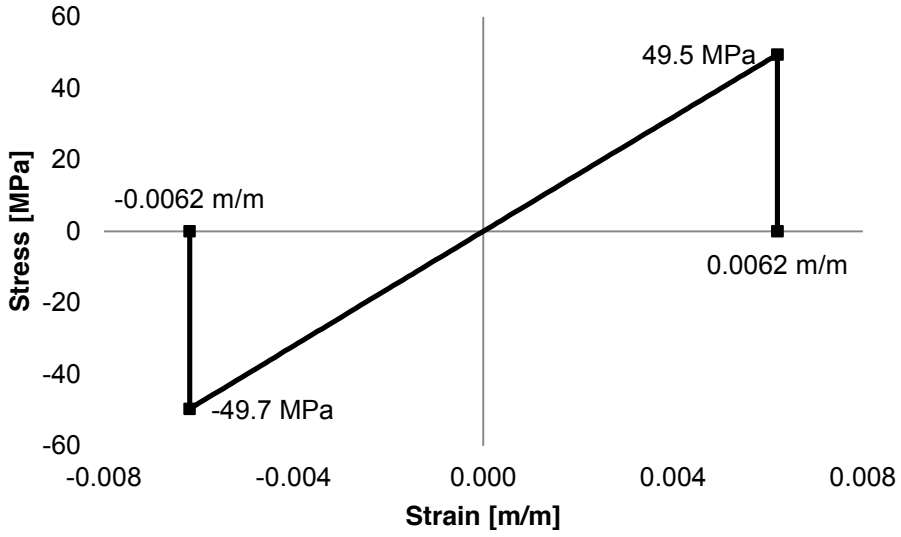

Figure 40: **Simulated stress strain behaviour of unidirectional glass fibre reinforced epoxy loaded in compression and tension in the 90° axis direction.**

Similarly, the correct definition of the material model for unidirectional glass fibre was confirmed in *Figure 40.* The model was defined to fail at 50 MPa and 0.00625 m/m in both tension and compression.

5.1.6 Bidirectional Glass Fibre

The final four experiments were for the bidirectional glass fibre model. Firstly, the single element was strained in tension and compression in the 0° direction. The results in *Figure 41* show that the material behaved as expected according to the values defined in *Table 4.* The expected values at failure in tension were 223 MPa and 0.009911 m/m, while failure in compression was expected at 180 MPa and 0.008 m/m.

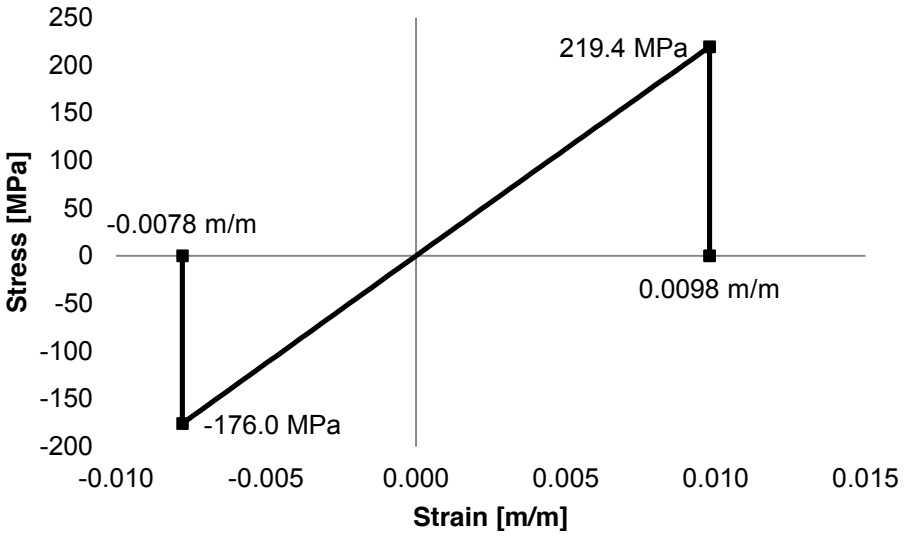

Figure 41: Simulated stress strain behaviour of bidirectional glass fibre reinforced epoxy loaded in compression and tension in the 0° axis direction.

The final manifestation of the error associated with DFAILM occurred in the bidirectional glass fibre test. Once again, rather than failing at the strain determined by Naude (2008), the element strained beyond this value to DFAILM. The results are given in *Figure 42.*

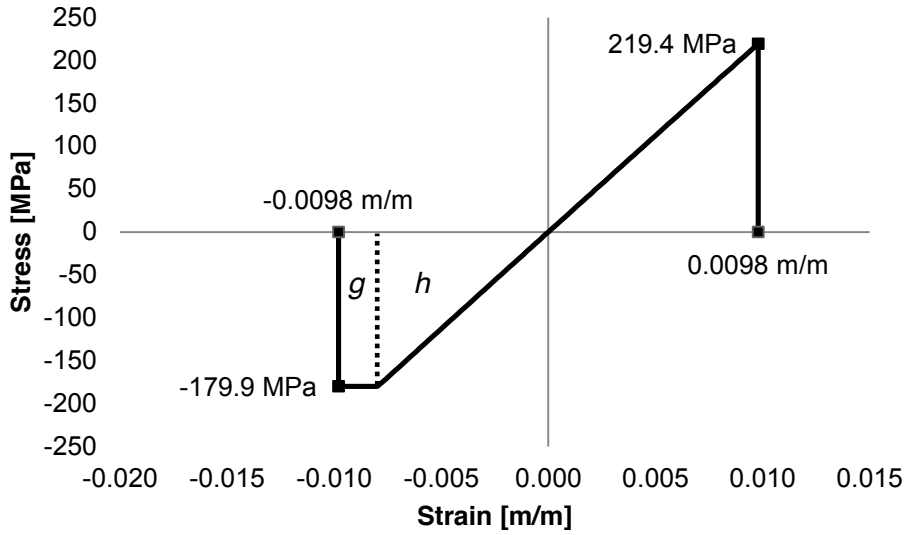

Figure 42: Simulated stress strain behaviour of bidirectional glass fibre reinforced epoxy loaded in compression and tension in the 90° axis direction.

If g and h represent the areas under the curve, the ratio between the simulated and expected energy absorption is:

$$\frac{g+h}{h} = 1.72 \qquad [29]$$

This overestimation is less significant than previous occurrences and is also of low concern. Random elements containing this material model were monitored in subsequent simulations to determine the extent of the effect of the error on overall model accuracy. The material behaviour was otherwise normal and failure in tension occurred near 223 MPa and 0.009911 m/m as defined in *Table 4.*

5.1.7 Summary of Single Element Simulations

A total of 24 simulations were done to check that the 6 material models were correctly defined. Apart from four instances where DFAILM caused an overestimation in energy absorption, all material models behaved as intended by the input parameters defined in *Table 4.* Furthermore, the models closely approximated the properties that were tested by Naude (2008). In each case where an error was observed, the resulting overestimation was quantified. The material models were deemed acceptable to apply to the fuselage model for full scale crash simulations. This behaviour was monitored in those simulations to determine its effect on accuracy. During the course of all the cockpit simulations, no elements were found to exhibit these errors.

5.2 Square Crash Box Simulations

The square glass fibre crash box described in *Section 4.5* was simulated and results compared to experimental results. This step was used to verify the accuracy of the modelling methods used in the JS1 crash models.

The model, named RM1, was able to simulate progressive crushing behaviour comparable to the photographs taken during the experiment by Albertsen *et al.* (2008). A visual comparison between the photographs and the simulation results is shown in *Figure 43*.

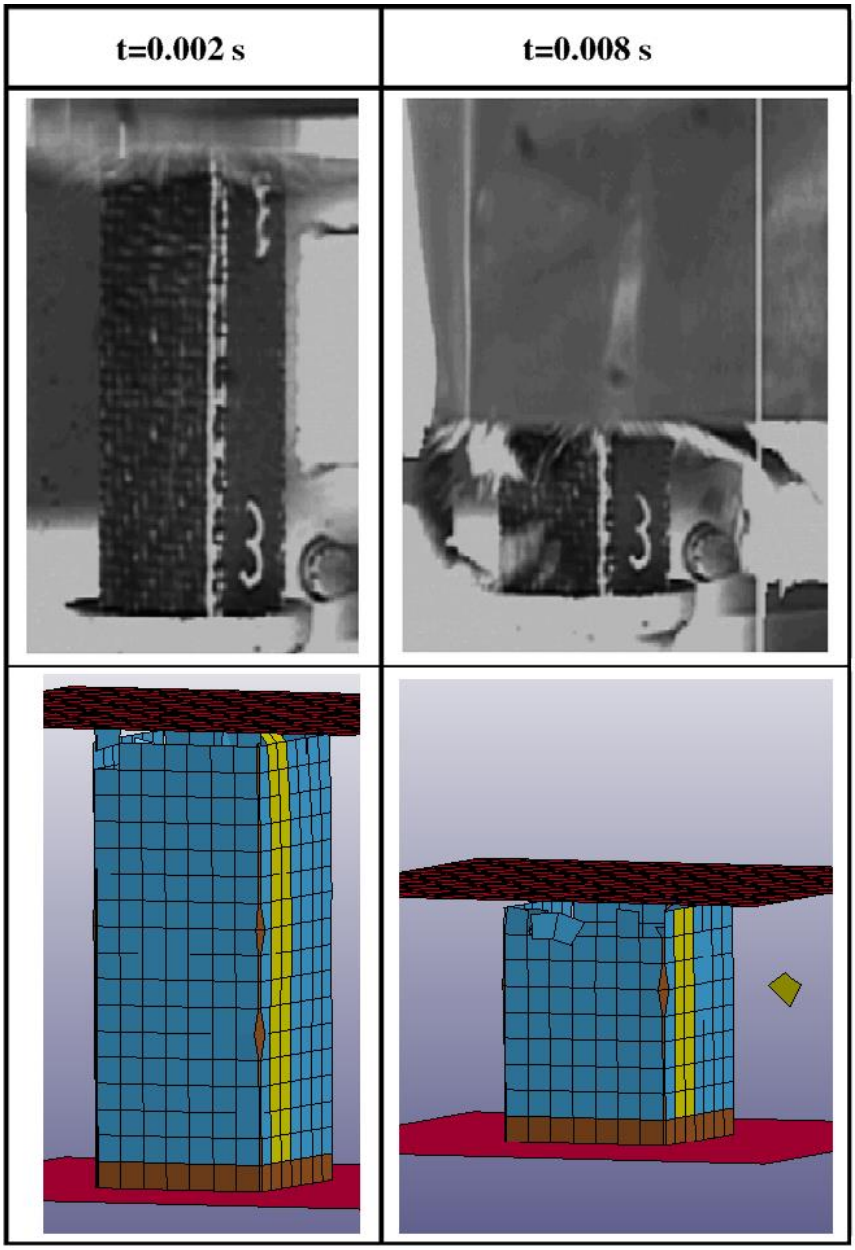

Figure 43: **Visual comparison between experimental and numerical results of a square crash box.**

This comparison shows that the RM1 FE model was able to simulate the progressive crushing behaviour observed in the experiment. However, the model failed to simulate the splitting of the corners accurately, which is evident in the images captured by Albertsen *et al.*

A comparison of the load displacement curves and energy absorption displacement curve is given in *Figure 44* below. Immediately it can be seen that crash load was significantly understated in the simulation. The peak load and average load during the first 80 mm of displacement were found to be underestimated by 28% and 58% respectively, compared to the corresponding average of S-1, S2 and S-3 conducted by Albertsen *et al.* (2008). The corresponding underestimation in energy absorption was found to be 71%.

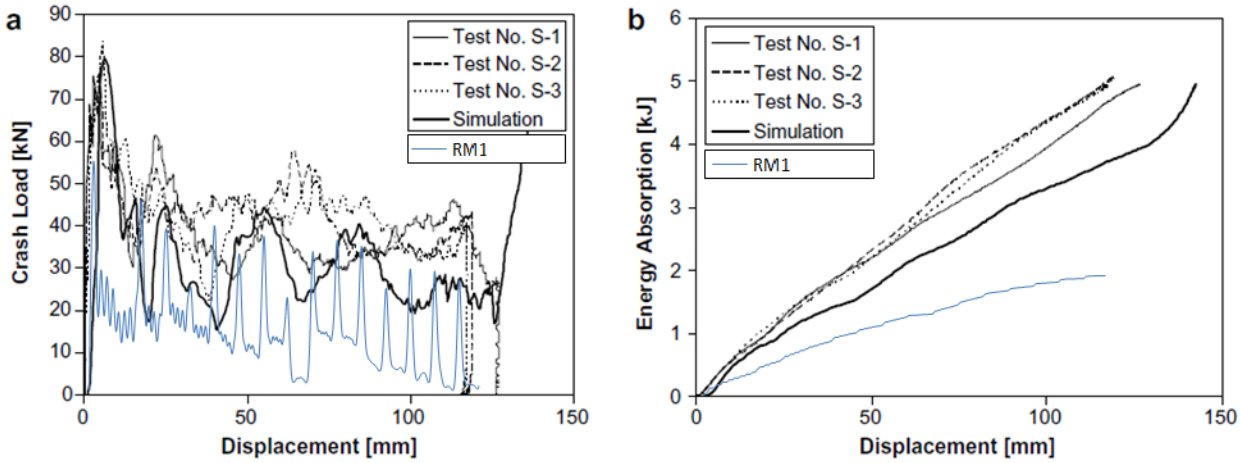

Figure 44: Comparison of simulated results to experimental and simulated results recorded by Albertsen *et al.* (2008).

Based on the comparison in *Chapter 4* between the FEM features of the two FE models, these results are assumed to be an indication of the accuracy of the JS1 crash simulations. The basis of the assumption is that the same modelling methods were used to model the square crash box and the JS1 crash model.

5.3 Chapter Conclusion

The single elements and square crash box model were successfully simulated. Stress strain results were obtained from the single element models and compared with the experimental results recorded by Naude (2008). This step verified that material models were correctly defined and showed that the materials will exhibit the desired failure behaviour in a full scale simulation.

Similarly, the square crash box model was successfully simulated and compared to results recorded by Albertsen *et al.* (2008). The model was able to simulate progressive crushing behaviour, but energy absorption was significantly underestimated. The underestimation can be attributed partly to the inability of the single-element-layered model to simulate failure behaviour such as delamination, which contributes significantly to the energy absorption of composite materials.

Chapter 6 Crash Simulation Results

6.1 Introduction

This chapter contains the results of the various standard and enhanced crash models of the JS1 cockpit described in *Chapter 4.* The chapter begins with the simulated results of high and low impact velocity crashes of the standard JS1 structure. Next, results of 10 enhanced structures, developed progressively using an aluminium-honeycomb energy absorber, are given. Thereafter the chapter concludes with simulated results of two different energy absorbers that are constructed only of fibre-laminate materials.

6.2 Initial Crashworthiness Study

Two crash simulations were done to determine the crashworthiness of the existing JS1 cockpit. The finite element model used in this study is described in detail in *Chapter 4*. Separate simulations at low and high impact velocity were done to determine whether velocity affected the energy absorption characteristics of the structure.

6.2.1 Initial Crashworthiness at Low Velocity

The details of the first simulation are given in *Table 8.* The velocity was selected based on some initial simulations that are not reported here. The lowest velocity that resulted in stable crushing of the structure was selected. The mass was selected as the maximum mass of the heaviest variant of the JS1 sailplane.

Simulation ID	Based on FE model	Modifications	Impact velocity [m/s](KCAS)	Total mass [kg]	Comments
IC0	fuseMod1_hook_ fusechange.db	Refer to *Section 4.3*	2.3(1.24)	720	Mass based on the heaviest variant of the JS1

Table 8: Details of the IC0 simulation.

The deformation during the first 515 mm of displacement is shown in *Figure 45.* The colours in the fringe plot correspond to in-plane stress and were used as a visual aid to identify stress concentrations. Note how the stress and deformation were localised at the impact front, while

the cockpit structure remained intact. Since no failure of the main stiffening structure occurred, this model passed the collapse test.

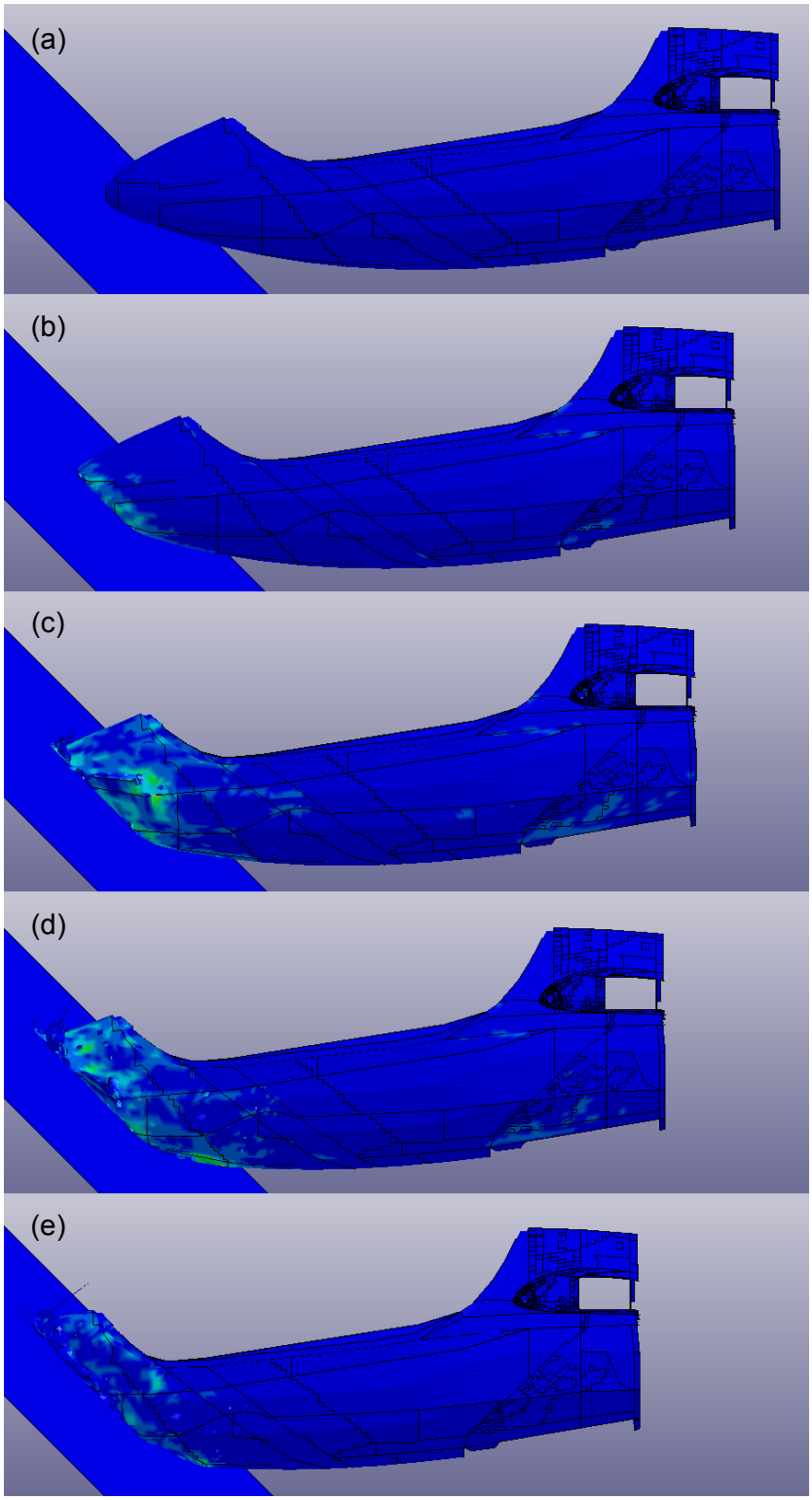

Figure 45: **Deformation of the JS1 cockpit during the IC0 simulation at (a) 0 mm (b) 155 mm (c) 290 mm (d) 410 mm and (2) 515 mm displacements.**

The load displacement results of simulation IC0 are shown in *Figure 46*. The data, sampled at 10 kHz, was filtered at 1 kHz and 60 Hz using a numerical Butterworth filter. This was done to smooth data and to reveal the underlying crash pulse. *Figures 46(b)* and *46(c)* show that filtration reduced the peak crash load initially measured at 7.6 kN in *Figure 46(a)* to 6.9 kN and 4.4 kN respectively. The data also show that the peak crash load shifted to different displacements at different filter frequencies. Since the crash load corresponds to the stiffness of the structure as it deforms, the filtered data can be misleading when trying to eliminate the cause for high peak loads. For this reason peak crash loads were strictly obtained from the unfiltered data.

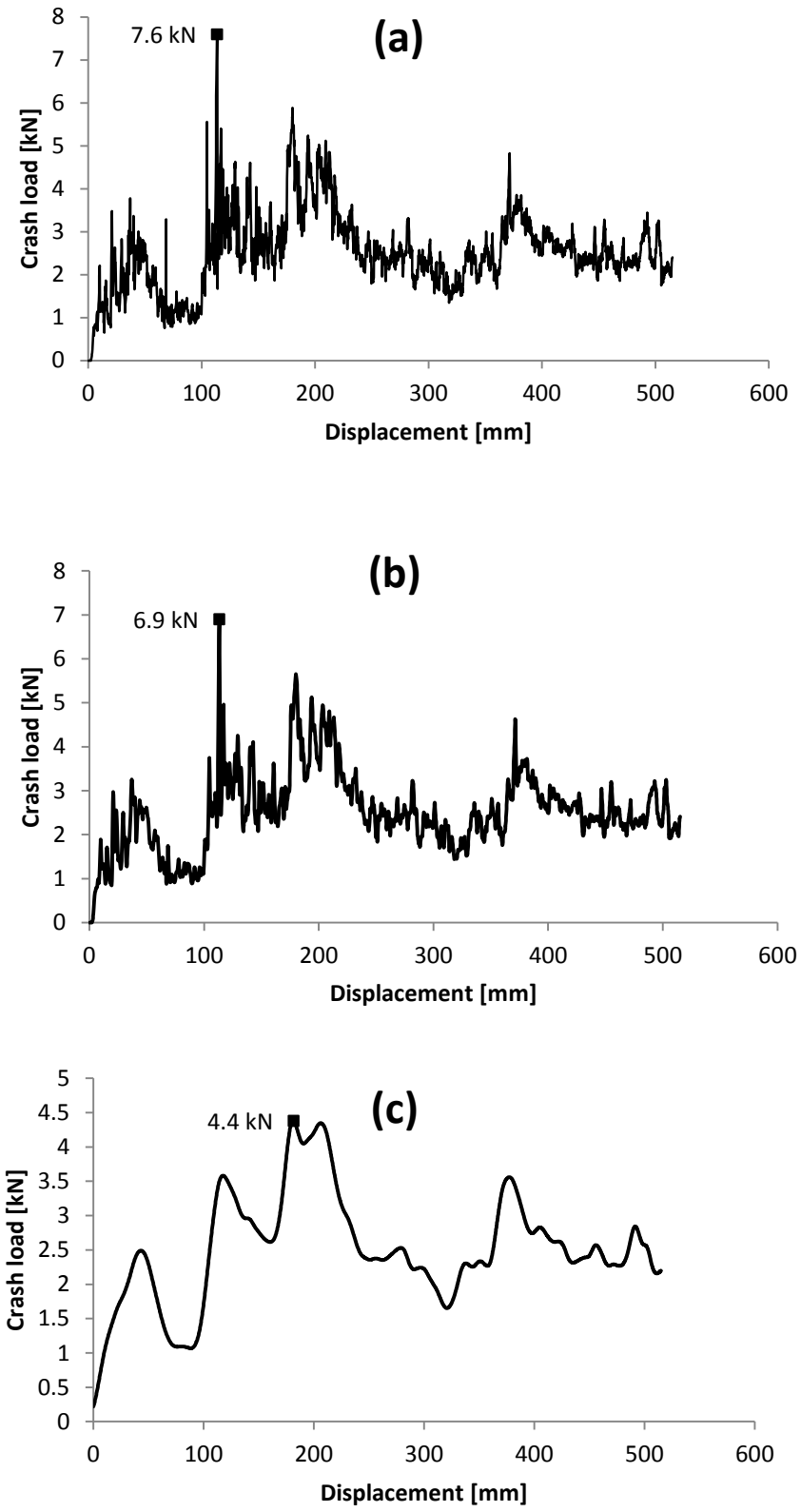

Figure 46: **Crash load plotted against displacement for simulation IC0 filtered at (a) 10 kHz (b) 1 kHz and (c) 60 Hz.**

Since energy absorption is represented by the area under the load displacement curve, this value is given by:

$$W = \int_{S_i}^{S_{i-1}} P dS \quad [30]$$

where P is the crash load and S is the displacement. The integral can be approximated by:

$$W = \bar{P}(S_i - S_{i-1}) \quad [31]$$

Equation 31 was used to calculate the energy absorption during the first 515 mm of displacement for simulation IC0. The resulting energy absorption was:

$$\begin{aligned} W_{IC0} &= \bar{P}(S_i - S_{i-1}) \\ &= 1297.5\, J \end{aligned}$$

Specific energy absorption was calculated by dividing energy absorption by deformed mass as follows:

$$\begin{aligned} SEA_{IC0} &= \frac{W_{IC0}}{m_{IC0}} \\ &= \frac{1297.5}{2.1} \\ &= 617.9\, J/kg \end{aligned}$$

Since this model was considered to be the reference for all subsequent simulations, the system energy absorption was considered to be equal to the specific energy absorption.

$$SSEA_{IC0} = SEA_{IC0} = 617.9\, J/kg$$

6.2.2 Initial Crashworthiness at High Velocity

A high velocity simulation of the unmodified cockpit was done next. Since the MATD054 material model is unable to simulate strain rate sensitivity, the results were expected to be similar to those obtained from the previous simulation. Velocity was increased to 22.22 m/s based on the stall speed of the JS1 and mass was lowered to 500 kg based on a typical landing configuration. *Table 9* provides details about the IC1 simulation.

Simulation ID	Based on FE model	Modifications	Impact velocity [m/s] (KCAS)	Total mass [kg]	Comments
IC1	fuseMod1_hook_ fusechange.db	Refer to *Section 4.3*	22.22(12.00)	500	Mass based on typical landing mass. Velocity based on stall speed.

Table 9: Details of the IC1 simulation.

The cockpit is shown in *Figure 47* at the final displacement of 515 mm. Similar to IC0, the cockpit maintained its integrity during the crash and therefore passed the collapse test.

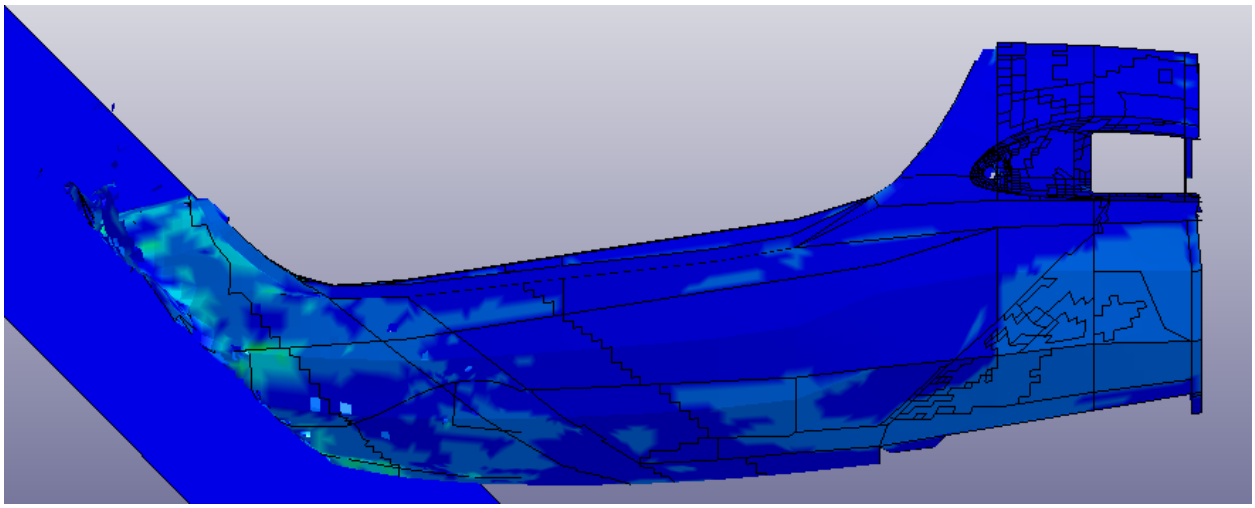

Figure 47: The JS1 cockpit after 515 mm of displacement during the IC1 simulation.

Load displacement results were left unfiltered in this instance due to the issues encountered when the IC0 data was filtered. Peak load during this simulation was significantly higher than during IC0 and was recorded at 16.6 kN at 202 mm displacement. Results were plotted and are shown in *Figure 48.*

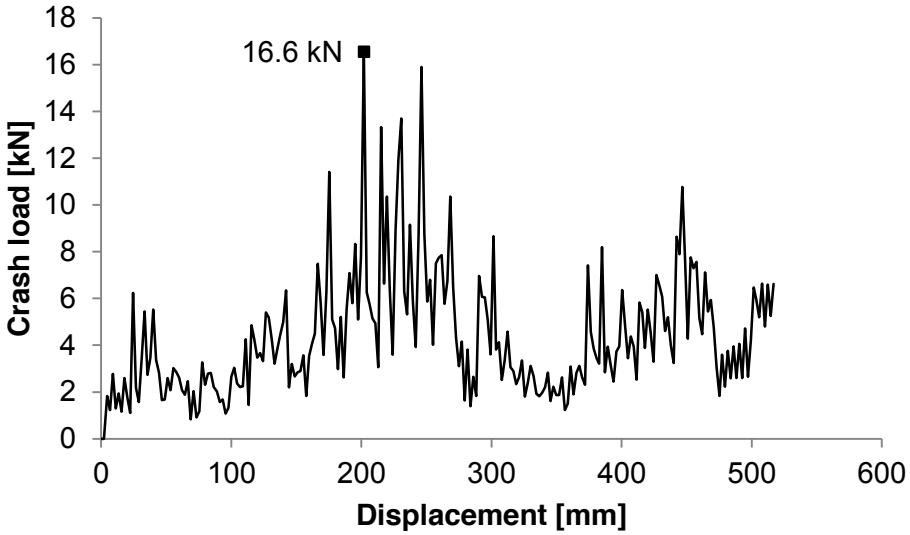

Figure 48: Crash load displacement results for the IC1 simulation with 22.22 m/s impact velocity and 500 kg mass.

This data was used to calculate energy absorption, specific energy absorption and system-specific energy absorption using *Equations 31, 24* and *25* respectively. Results of these calculations are shown below.

$$W_{IC1} = 2231.8\,J$$

$$SEA_{IC1} = 1062.8\,\frac{J}{kg}$$

$$SSEA_{IC1} = 1062.8\,\frac{J}{kg}$$

In the case of simulation IC1, *SEA* and *SSEA* were again equal since no modifications were made to the structure. Counterintuitively, the energy absorption results did not correspond to those obtained from IC0. In total, 444.9 J more energy was absorbed in simulation IC1 compared to IC0. This result was unexpected as the model had not been changed and the material models could not simulate strain rate sensitivity.

The ratio between total energy and initial energy was used to determine which model was likely to be more accurate. Since IC0 achieved 0.93 for this ratio and IC1 achieved 1.0, the latter was taken as the reference against which subsequent simulations would be compared. This is also likely to be the reason for the discrepancy between the results for IC0 and IC1.

6.3 New Crashworthiness

Enhanced models were created to determine the comparative improvements in energy absorption due to various structural changes. Based on the work of Heimbs (2012), aluminium 5052 honeycomb was selected as the preferred material for the initial energy absorbers. More specifically, the HexWeb™ 1/8" Al-5052 honeycomb range produced by Hexcel® was chosen. This range of materials offered excellent weight-specific properties when stabilised in a sandwich configuration. The data in *Table 10* were obtained from the Hexcel® material properties guide for HexWeb™ honeycombs.

Hexcel Honeycomb Designation Cell Size – Alloy – Foil Gauge	Nominal Density pcf	Compressive					Crush Strength psi
		Bare		Stabilized			
		Strength psi		Strength psi		Modulus ksi	
		typ	min	typ	min	typ	typ
1/16 – 5052 – .0007	6.5	950	740	1000	780	275	505x
1/16 – 5052 – .001	9.2	1500	1170	1550	1200	420	750x
1/16 – 5052 – .0015	12.4	2430	1900	2650	2000	650	1200x
1/8 – 5052 – .0007	3.1	285	200	300	215	75	130
1/8 – 5052 – .001	4.5	550	375	570	405	150	260
1/8 – 5052 – .0015	6.1	980	650	1020	680	240	450
1/8 – 5052 – .002	8.1	1500	1000	1560	1100	350	750
1/8 – 5052 – .0025	10.0	2100p	1575p	2250p	1685p	500x	1050x
1/8 – 5052 – .003	12.0	2700	2100	2900	2200	900	1350x

Table 10: Mechanical properties of Hexcel® honeycomb materials (Hexcel, 1999:16).

Since the energy absorber has to function within the existing design of the JS1, limited space prevents the use of large volumes of honeycomb material. The majority of the internal volume of the nose of the aircraft is occupied by other components. Therefore, a sandwich configuration was selected for its versatility and efficient use of space.

In the first enhanced model, a 7 mm layer of 1/8-5052-.003 honeycomb was sandwiched between the skin of the nose and a second similar layer. The second composite layer consisted of [GUD/GBID/GBID/GBID/ABID], each with a thickness of 0.25 mm stacked in the sequence [0°/45°/0°/0°/45°]. The concept energy absorber is shown in *Figure 25* in *Chapter 4.*

Note that for the purpose of simulation, the sandwich layer was applied to the outside of the nose, whereas in practice it should be applied to the inside. Other aspects of the model remained unchanged from the IC1 model, including impact velocity and mass. *Table 11* contains a summary of the details of the NC2 model.

Simulation ID	Based on FE model	Modifications	Impact velocity [m/s] (KCAS)	Total mass [kg]	Comments
NC2	IC1	7 mm aluminium honeycomb layer added to the nose, sandwiched between two composite layers.	22.22(12.00)	500	None

Table 11: Details of the NC2 simulation.

The simulation results revealed that the selected combination of materials was too stiff in relation to the rest of the structure to yield effectively during a crash. Instead, the energy absorber yielded partially until the cockpit structure failed at a stress concentration point, located at the interface between the nose and the cockpit. The resulting failure is shown in *Figure 49.* Due to this failure of the main cockpit structure, it failed the collapse test.

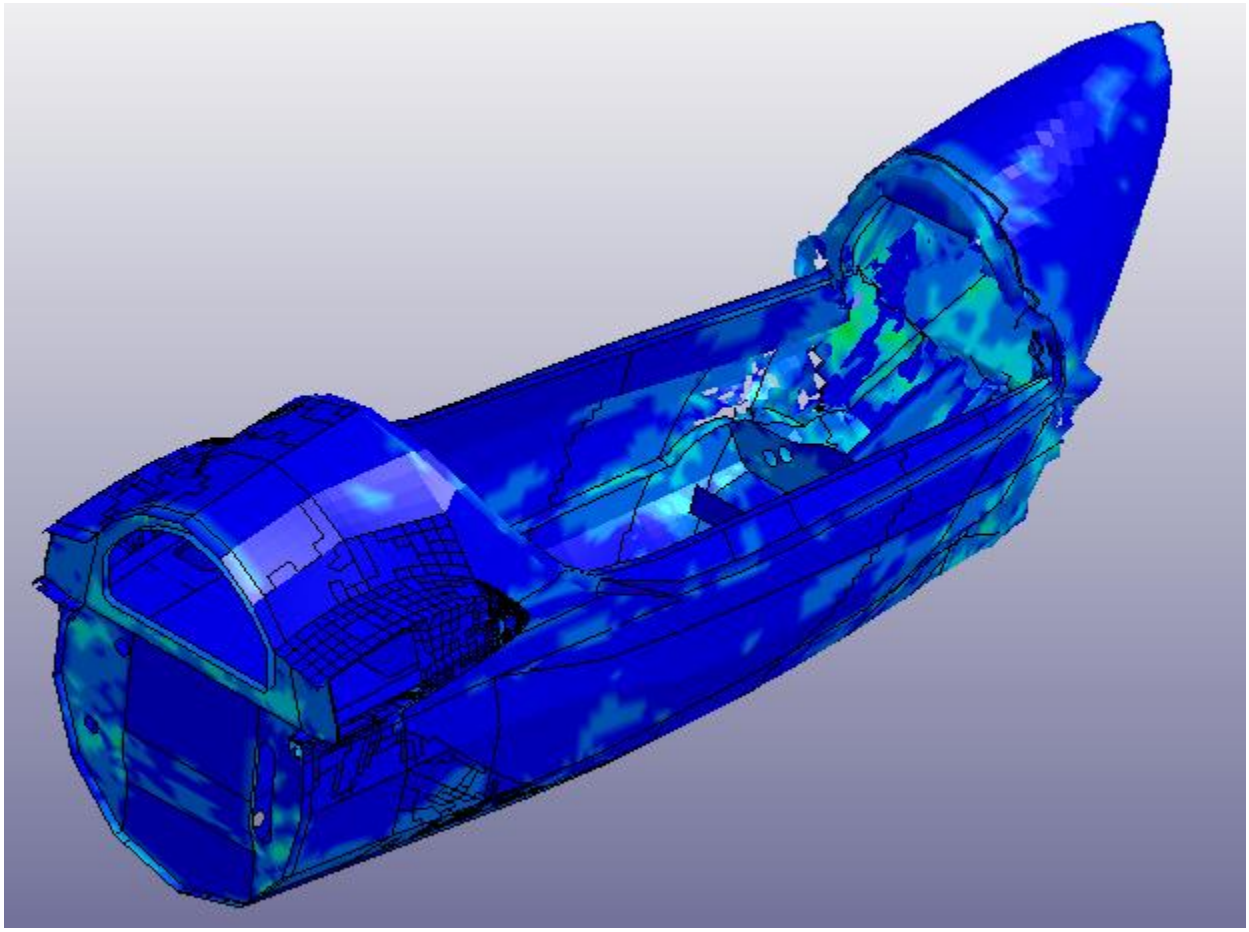

Figure 49: Deformation of the cockpit after 515 mm of displacement during the NC2 simulation.

Energy absorption results are given for reference only, and were disallowed on account of the collapse test criteria. Total energy absorption was calculated as 2440.4 J, so that *SEA* was 647.4 J/kg and *SSEA* was 539 J/kg. The load displacement results for simulation NC2 are shown in *Figure 50.*

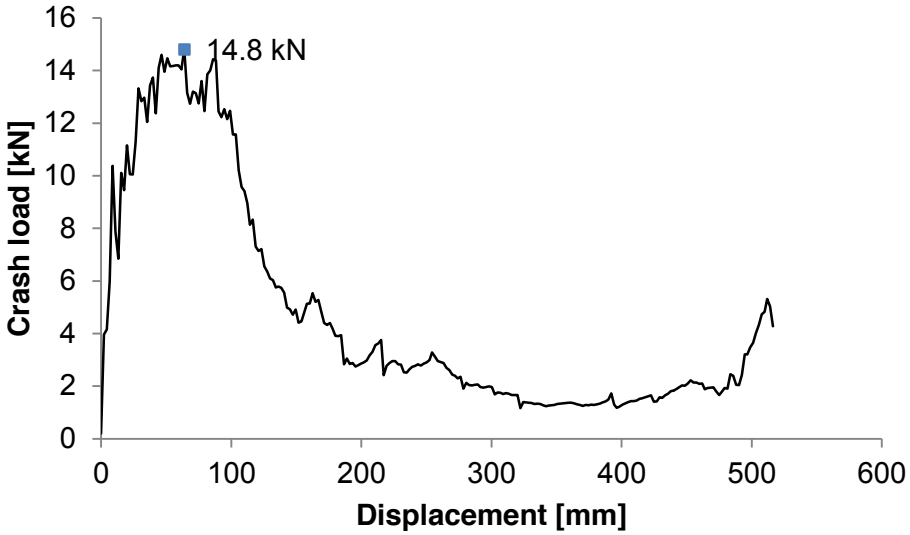

Figure 50: Crash load displacement results from simulation NC2.

The crash load increased rapidly over the first 50 mm of displacement, then reached a plateau. The peak load of 14.8 kN occurred at a displacement of 64 mm, after which the load began to decrease until it reached a minimum value of 1.1 kN at 322 mm of displacement. The curve corresponds to the observation that the energy absorber provided resistance until the remaining structure could no longer carry the load.

Apart from NC2, 11 more variants of this model were created with model IDs NC3 to NC13. For NC3 to NC11, progressive changes were made to the honeycomb material, the sandwich construction and stiffness of the remaining structure. Each change was based on the results and observations from the preceding simulation. If the structure failed the collapse test, the energy absorber was weakened, or the remaining structure strengthened, or both. If the structure passed the collapse test, energy absorption data were collected for analysis. In NC12 and NC13, the honeycomb and outer composite skin was substituted with a carbon fibre laminate for comparison. Further details of the most successful structure are given in *Appendix B*.

A summary of the changes made to each model and the respective collapse test results are given in *Table 12.* Refer to *Appendix B* for further details about structural modifications. In the collapse test column, the term “early termination” indicates that a simulation failed to complete 515 mm of displacement due to negative volume of brick elements. In these instances, the solver terminated automatically and changes were made to material properties and element formulations to correct this behaviour. The progressive modification process was repeated until

5 models passed the collapse test and usable energy absorption data could be collected for them.

Simulation ID	Base model	Modifications	Collapse test result
NC3	NC2	Stiffened the interface between the energy absorber and cockpit.	Fail
NC4	NC3	Reduced energy absorber stiffness by changing to Hexcel 1/8-5052-.002. Stiffened the interface between the cockpit and the rear of the fuselage.	Early termination
NC5	NC4	Redefined stress strain curve for honeycomb to continue to provide resistance to full compaction.	Fail
NC6	NC5	Weakened the energy absorber by changing to Hexcel 1/8-5052-.0007.	Early termination
NC7	NC6	Stiffened the rear of the main longitudinal beam. Weakened the energy absorber by removing material from parts 3 and 4 and shortening the front of the main longitudinal beam by 125 mm.	Pass
NC8	NC6	Stiffened the energy absorber by changing to Hexcel 1/8-5052-.001. Stiffened the rear cockpit structure. Stiffened the rear of the main longitudinal beam.	Early termination
NC9	NC8	Stiffened the energy absorber by changing to Hexcel 1/8-5052-.002. Stiffened the rear of the main longitudinal beam. Stiffened the length the main longitudinal beam.	Fail
NC10	NC8	Stiffened the main longitudinal beam. Stiffened the skin of the sandwich arrangement.	Pass
NC11	NC10	Stiffened energy absorber by substituting glass fibre layers with carbon fibre in parts 3 and 4. Stiffened forward subfloor beams. Stiffened the main longitudinal beam at the interface between the energy absorber and cockpit.	Pass
NC12	NC11	Honeycomb and outer skin removed and substituted with 3 mm bidirectional carbon fibre layer. Stiffness of the remaining structure was left unchanged from NC11.	Pass
NC13	NC12	Increased thickness of the bidirectional carbon fibre layer to 5 mm.	Pass

Table 12: Summary of modifications and collapse test results for simulations NC3 to NC13.

The 5 models that passed the collapse test were NC7, NC10, NC11, NC12 and NC13. During these simulations, the energy absorber was sufficiently weak in relation to the cockpit structure, so that the cockpit did not collapse during the first 515 mm of displacement. In order to compare the energy absorption characteristics of each of the models, the filtered load displacement results were plotted in *Figure 51*. As discussed in preceding paragraphs, load peak information is obtained from unfiltered results, while the filtered results reveal the underlying crash pulse, which is used for graphical comparison. The results of model IC1 were also plotted so that the relative improvement of the enhanced models can be seen.

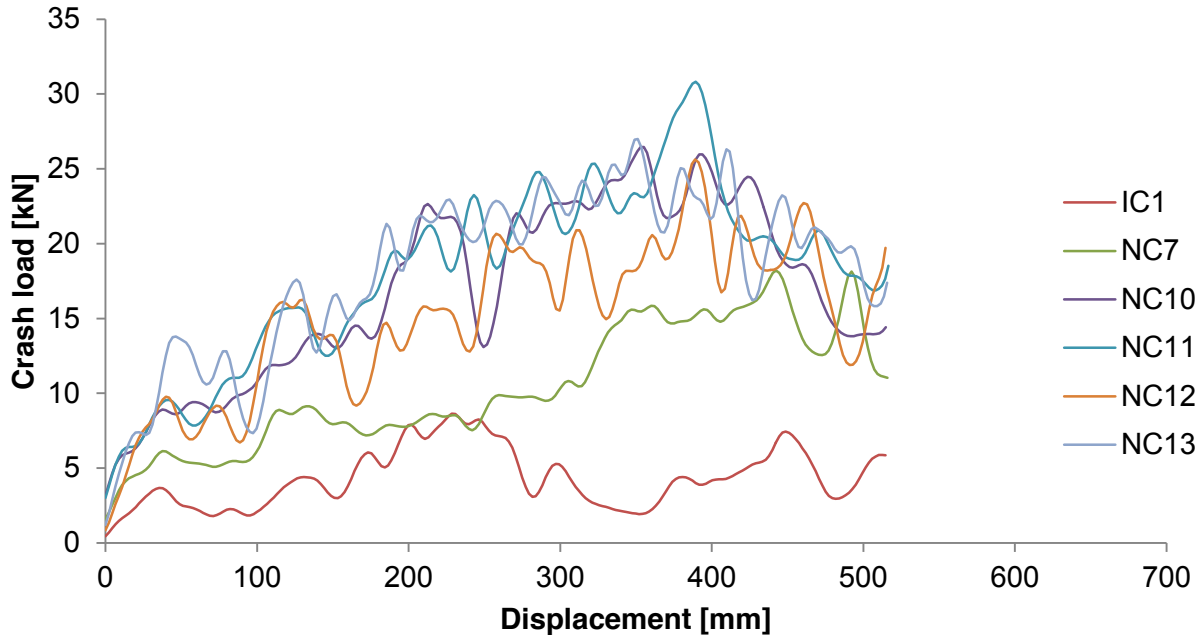

Figure 51: **Crash load displacement results of simulations IC1, NC7, NC10, NC11, NC12 and NC13 filtered with 600 Hz cut-off frequency.**

Table 13 gives a summary of the features of the unfiltered results from NC7, NC10, NC11, NC12 and NC13. The magnitude and location of load peaks are given, as well as energy absorption, *SEA* and *SSEA*. Note the 135 mm difference in displacement between the load peaks of NC7 and NC10, which corresponds closely to the 125 mm of the main longitudinal stiffener that was removed in NC7 and reinstated in NC10.

Simulation ID	Displacement at peak load [mm]	Peak load [kN]	W [J]	SEA [J/kg}	SSEA(ranking) [J/kg]
NC7	492	34.6	5339.0	1841.0	305.0(5)
NC10	357	34.6	8724.7	2029.0	420.4(2)
NC11	387	33.9	9362.8	2035.4	443.7(1)
NC12	415	40.4	7809.3	1440.8	339.5(3)
NC13	288	46.0	9432.5	1381.0	336.9(4)

Table 13: Summary of results of simulations NC7, NC10, NC11, NC12 and NC13.

Note the ranking in terms of *SSEA* given in brackets. These results show that NC11, using Hexcel 1/8-5052-.002 in sandwich configuration, produced the highest *SEA* and *SSEA*.

6.4 Chapter Conclusion

It is clear from the results in this chapter that the modifications in NC10 and NC11 offer the best relative improvement in terms of *W*, *SEA* and *SSEA*. Since both models offer virtually the same *SEA*, the only clear advantage of implementing NC11 over NC10 is a higher value for *W*. Full details of the structural modifications applied to NC11 are given in *Appendix B.*

The performance of the NC12 and NC13, constructed only of fibre-composite materials, was also determined. Compared to the absorbers constructed of honeycomb material, these structures absorbed less energy per unit mass. This can be attributed to the lower specific energy absorption characteristics of carbon fibre (used in NC12 and NC13) compared to aluminium honeycomb. In practical applications, however, this type of absorber may still prove to be superior due to its lower cost and versatility.

Chapter 7 Conclusion

Explicit finite element analysis was successfully applied to produce crash simulations of the JS1 cockpit. Full scale models were analysed on a personal computer and results were produced that were used to compare the crashworthiness of various composite structures.

The ability of the single element models to correctly simulate the physical material behaviour tested by Naude (2008) provided increased confidence in the accuracy of the ultimate results obtained from the various crash models. Even though the vast majority of the materials behaved correctly, the single element simulations revealed some disadvantages of the MATD054 model.

In every instance, the model was able to accurately simulate the strain and stress at failure when loads were applied in the primary material axis. This is a result of the two separate parameters that can be set to determine strain to failure in tension and compression. These parameters are known as DFAILT and DFAILC. On the other hand, only one strain-to-failure parameter can be set when defining the properties for the perpendicular, or 90°, material direction. This means that the element will fail at the same strain when subjected to tension and compression. In reality, this is considered uncommon behaviour. The user is left with the decision to use the greater of the two strains, the smaller, or some intermediate value based on the expected bias between tension and compression failure in the problem.

For the purpose of this study, the greater value was always used. This choice resulted in 4 instances where the energy absorbed by the material was overestimated. A factor of 5.7 was calculated for the largest overestimation. The true effect of this error on the eventual accuracy of the crash simulations could not be determined. It is, however, thought to be insignificant due to the inability to find any examples of the error in the cockpit crash simulation results. The stress strain results from random failed elements that contained the erroneous material models were checked. None were found to have failed under the specific conditions, which are known to cause the error to materialise.

If alternatively, the lower value was used for DFAILM, there would have been 4 instances where energy absorption was underestimated. Still, if an intermediate value was chosen, the single element results would have contained 8 instances where energy absorption was either over- or underestimated.

In order to compare results from the existing and enhanced cockpit models, a useful method was developed to quantify crashworthiness. The method was to test whether the cockpit structure had maintained its integrity during a crash, and if so, to calculate the energy

absorption. If the structure collapsed during the simulation, the energy absorption results were disregarded since the structure failed to maintain a safe volume for the occupant to survive in.

Furthermore, to ensure that results were comparable across all simulations, a set crash displacement was assessed and the model was constrained so that it could not rotate upwards due to the reaction force of the sloped wall. A total crash displacement of 515 mm was selected based on the maximum allowable displacement without reduction of the occupant's safe volume. This did not mean, however, that all energy had been absorbed in 515 mm. In all simulations, initial and enhanced, significant kinetic energy was still present after 515 mm of displacement. It did, however, produce results that could be directly compared between models with different stiffnesses.

The results obtained from IC0 and IC1 indicate that 1297.5 J and 2231.8 J were absorbed by the JS1 during these simulations respectively. Even though the initial kinetic energies in both simulations were different, energy absorption was expected to be equal. The expectation was based on the relationship between structural stiffness and energy absorption, and the fact that both models were identical in all aspects except for initial kinetic energy. Furthermore, since MATD054 cannot simulate strain rate sensitivity, viscoelastic effects could not be blamed for the discrepancy in the two results. Since no concrete reason could be found for the difference, IC1 was selected as the reference for subsequent simulations on account of its energy ratio of 1. This ratio is calculated by the solver as follows:

$$eratio = \frac{E_{total}}{E^0_{total} + W_{ext}} \quad [32]$$

where E_{total} is the sum of kinetic, internal, sliding interface, rigid wall, damping and hourglass energies, and $E^0_{total} + W_{ext}$ is the sum of initial kinetic and internal energies and external work. An energy ratio of 1 indicates a perfect energy balance. In the case IC0, however, this ratio was calculated as 0.93, indicating a significant inaccuracy in the simulation. On this basis, results from the IC0 simulation were disregarded.

Significant increases in energy absorption were achieved in the enhanced models by the addition of an energy absorber. 5 out of 12 simulations were successful to an extent that energy absorption data could be collected. It was found that the problem is firstly to achieve the correct balance between the stiffness of the frontal energy absorber and the rest of the structure, and then to increase the stiffness of both simultaneously. Initially the energy absorber was installed without stiffening the remaining structure. This led to the cockpit structure failing, rather than the

energy absorber. The absorber was then gradually weakened while the cockpit was stiffened until the correct balance was found. Both structures could then be stiffened simultaneously.

Compared to the existing structure of the JS1, energy absorption was increased by approximately 8 000 J by adding a dedicated energy absorber. The absorber was simple in construction and consisted of a sandwich structure with 7 mm thick aluminium honeycomb core and composite outer skins. Since the absorber resulted in crash loads of up to 33.9 kN, a significant weight penalty had to be sacrificed to stiffen the remaining structure sufficiently. The total mass difference between the existing JS1 structure and the structure used in NC11 was 21 kg. Of this mass, 3.7 kg actively absorbed energy through deformation, while the other 17.3 kg consisted of passive stiffening.

From a comparison between the energy absorption performance of the honeycomb-based and fibre-composite-based absorbers, it can be concluded that the specific energy absorption characteristics of the construction materials represent the energy absorption characteristics of the structure. It was found that the honeycomb outperformed the fibre-composite when assessed in terms of weight-specific energy absorption.

A useful quantity called system-specific energy absorption was defined. It is calculated as the energy absorption divided by total mass increase due to the energy absorber and passive stiffening. Its purpose was to quantify the influence of passive mass on the weight-specific energy absorption of the aircraft. Alternatively, when the conventional quantity of specific energy absorption was used to determine weight-specific performance, the passive mass would not be taken into account.

Finally, based on the comparison between the experimental results of Albertsen *et al.* and a finite element model of that experiment, built using the same methods as the JS1 model, it can be deduced that energy absorption in the JS1 simulations is significantly underestimated. Peak and average crash loads were found to be understated in the simulations, leading to underestimation of energy absorption. The findings can be partially accounted for by the inability of the single-element-layered model to simulate inter- and intralaminar failure behaviour, which contribute towards energy absorption in composite materials. Because the strain rate related properties of the JS1 materials are unknown, an assumption was made that the materials do not exhibit strain rate sensitivity. This may have further contributed to the underestimation in energy absorption.

One possible topic for future work based on this study would be to determine a corrective factor, or set of corrective factors to account for these inabilities. Such a study will eventually require

the full-scale crash testing of a JS1 cockpit, which will provide the undisputable data against which these models can be verified and further developed.

Other studies can potentially flow from this initial work. Since the basic crash models have been developed, further work can now focus on the optimisation of a crash energy absorber rather than accurate crash modelling, as was done in this study. Such a study will aim to maximise the equation $W = \bar{P}(S_i - S_{i-1})$. Since displacement in this case is limited by the available space in front of the occupant, the aim will be to optimise $\bar{P}$. The optimisation of $\bar{P}$ will lead to a plateau-shaped force displacement curve with the maximum area under the curve and the lowest possible peak load.

Reference List

Abramowicz, W. 2003. Thin-walled structures as impact energy absorbers. *Thin-Walled Structures*, 41(2–3):91-107.

Albertsen, H., Kröger, M. & Zarei, H. 2008. An experimental and numerical crashworthiness investigation of thermoplastic composite crash boxes. *Composite Structures*, 85(3):245-257.

Alghamdi, A.A.A. 2001. Collapsible impact energy absorbers: an overview. *Thin-Walled Structures*, 39(2):189-213.

Anghileri, M., Castelletti, L.M.L. & Lanzi, L. 2004. Multi-objective optimisation of composite absorber shape under crashworthiness requirements. *Composite Structures*, 65(3–4):433-441.

ANSYS, Inc. 2011. Explicit Dynamics Brochure 14.0. Canonsburg, PA.

Belingardi, G., Boria, S. & Obradovic, J. 2012. Lightweight design and crash analysis of composite frontal impact energy absorbing structures. *Composite Structures*, 94(2):423-430.

Blaurock, J., Heimbs, S., Hoffmann, M., Schmeer, S. & Waimer, M. 2013. Dynamic testing and modelling of composite fuselage frames and fasteners for aircraft crash simulations. *International Journal of Crashworthiness*, 18(4):406-422.

Byar, A., Deleo, F., Feraboli, P., Higgins, M., Rassaian, M. & Wade, B. 2011. *Composites: Part A,* 42:1809-1825.

Cocchetti, G., Pagani, M. & Perego, U. 2013. Selective mass scaling and critical time-step estimate for explicit dynamics analyses with solid-shell elements. *Computers & Structures*, 127:39-52.

EASA *see* European Aviation Safety Agency

Ebert, C., Gude, M. & Hufenbach, W. 2009. Hybrid 3D-textile reinforced composites with tailored property profiles for crash and impact applications. *Composites Science and Technology*, 69(9):1422-1426.

European Aviation Safety Agency. 2009. Certification specifications for sailplanes and powered sailplanes. CS-22 Amendment 2, book 2: Acceptable means of compliance. (Annex to ED decision 2009/009/R) Available from

http://easa.europa.eu/system/files/dfu/Consolidated%20version%20CS-22%20Amdt%202.pdf Date of access: 17 Jul. 2012.

FAA *see* Federal Aviation Administration

Fasanella, E.L. & Jackson, K.E. 2002. Best practices for crash modelling and simulation. Available from http://ntrs.nasa.gov/archive/nasa/casi.ntrs.nasa.gov/20020085101.pdf Date of access: 13 Aug. 2012.

Fasanella, E.L., Frings, G., Jackson, K.E., Jones, Y.T. & Vu, T. 2001. Crash Simulation of a Boeing 737 Fuselage Section Vertical Drop Test. Available from http://ntrs.nasa.gov/archive/nasa/casi.ntrs.nasa.gov/20040086069.pdf Date of access: 23 Sep. 2013.

Fasanella, E.L., Jackson, K.E. & Lyle, K.H. 2006. Crash Certification by Analysis – Are We There Yet? Paper presented at the 62nd Annual International Forum and Technology Display of the American Helicopter Society, Phoenix, AZ, 9-11 May. Available from http://ntrs.nasa.gov/archive/nasa/casi.ntrs.nasa.gov/20060020751.pdf Date of access: 29 Aug. 2012.

Federal Aviation Administration. 2003. Advisory Circular on the Methodology for Dynamic Seat Certification by Analysis for Use in Parts 23, 25, 27, and 29 Airplanes and Rotorcraft. Available from http://www.faa.gov/documentLibrary/media/Advisory_Circular/ac20-146.pdf Date of access: 9 Oct. 2012.

Federal Aviation Administration. 2013. Estimated active glider pilots by class of certificate 2004-2013. Available from http://www.faa.gov/data_research/aviation_data_statistics/civil_airmen_statistics/2013/ Date of access: 3 Feb. 2013.

Federation Internationale de l'Automobile. 2013. Formula One technical regulations. Available from http://www.fia.com/sites/default/files/regulation/file/2013%20F1TECHNICAL%20REGULATIONS%20-%20PUBLISHED%20ON%2004.07.2013.pdf Date of access: 23 Feb. 2013.

Peng, H., Tianchun, Z. & Zhenyu, F. 2011. Research Development of Crashworthiness Simulation Evaluation on Civil Aircraft. *Procedia Engineering*, 17:286-291.

Feraboli, P., Osborne, M. & Wade, B. 2010. Simulating laminated composites using LS-DYNA material model MAT54 part I: [0] and [90] ply single-element investigation. (Unpublished paper).

FIA *see* Federation Internationale de l'Automobile

Fritzsche, P., Hörmann, M., Müller, J., Weder, M. & Wyss, I. 2008. A procedure for the simulation of failure in thermoplastic composites. *Composite Structures*, 85(4):337-349.

Heimbs, S. 2008. Virtual Testing of Sandwich Core Structures with LS-DYNA. Paper presented at ANSYS Conference & 26th CADFEM Users' Meeting, Darmstadt, Germany, 22 October. Available from http://www.heimbs-online.de/Heimbs_2008_Virtual_Testing.pdf Date of Access: 18 Jul. 2014.

Heimbs, S. 2012. Energy absorption in Aircraft Structures. Paper presented at the International Workshop on Hydraulic Equipment and Support Systems for Mining, Huludao, China, 17-18 August. Available from http://www.heimbs-online.de/Heimbs_2012_IWHEM.pdf Date of access: 23 Jun. 2014.

Heimbs, S., Maier, M., Middendorf, P. & Schmeer, S. 2007. Strain rate effects in phenolic composites and phenolic-impregnated honeycomb structures. *Composites Science and Technology,* 67:2827-2837.

Hexcel Corporation. 2009. HexWeb™ Honeycomb Attributes and Properties. Pleasanton, California.

Jonker, A.S. 2012. JS1 Structural Design [personal interview]. Potchefstroom.

Kröger, M. & Zarei, H. 2008. Optimum honeycomb filled crash absorber design. *Materials & Design*, 29:193-204.

Livermore Software Technology Corporation. 2012. About LS-Dyna. Available from http://www.lstc.com/products/ls-dyna Date of access: 11 Mar. 2013.

Livermore Software Technology Corporation. 2013. LS-DYNA® Keyword User's Manual (Version R7.0), Livermore, CA.

LSTC *see* Livermore Software Technology Company

MSC Software Corporation. 2011. MSC Nastran 2012 Explicit Nonlinear (SOL 700) User's Guide, Santa Ana, CA.

MSC *see* MSC Software Corporation

Naude, S. 2008. Composite material test report NW-M-001. 1 Dec. 2008.

Plugge, E. 2005. Integrating LSTC and MSC,Software Technology for Explicit Dynamics and Fluid-Structure Interaction. Paper presented at the 5th European LS-Dyna Users Conference, Birmingham, UK, 25 May. Available from http://www.dynalook.com/european-conf-2005/Plugge.pdf Date of access: 17 Jul. 2014.

Röger, W. 2007. Safe and crashworthy cockpit. (Unpublished paper).

Savage, G. 2010. Development of penetration resistance in the survival cell of a Formula 1 racing car. *Engineering Failure Analysis,* 17:116-127.

Segal, T. 1998. Designing a sailplane safety cockpit. *Sailplane & Gliding*, 6:12-14.

Soaring Safety Foundation. 2013. Nov 1, 2011 – Oct 31, 2012 Safety Report. Available from http://www.soaringsafety.org/prevention/ssf_2012_annual_report.pdf Date of Access: 9 Oct. 2013.

SSF *see* Soaring Safety Foundation

Zhou, G. 1995. Damage mechanisms in composite laminates impacted by a flat-ended impactor. *Composites Science and Technology*, 54:267-273.

Appendix A: Research Design

This research design is divided into three subsections dedicated to the phases in the development of the experimental design. In the first subsection, a generic logical model for the treatment of known and unknown information in the study is developed. This model describes the generic pathway between the research problem and its solution. In the second subsection, the information and methods required to achieve each objective are identified in the context of the emerging research design. In the final subsection, the complete research design is presented visually in the form of a process flow diagram.

Research Framework

A generic framework for the JS1 crashworthiness study is developed in this section. This process is a means of visualising the flow of information and represents the first step towards the development of a unique research design. Since the research problem and objectives have been defined in *Chapter 1*, a framework of a possible solution can already be foreseen.

In light of the objectives, the known information required to produce a solution must be identified to become inputs to initial experiments. Simultaneously, information that is unknown at the start of the study and potential sources are identified. This process was initiated in the literature study from which some of the unknown information has been sourced. Information that cannot be sourced from literature is calculated if possible or conservatively assumed based on the findings in the literature study.

This information will become the input parameters to the early experiments. Outputs from these experiments will be inputs required for subsequent experiments and potentially solve certain research objectives or subproblems.

For each subsequent objective, the experimental process, including the sourcing of information, will be repeated. Required inputs will continuously be sought from earlier experiments and substituted by literature, calculations and assumptions, where necessary. The process is iterative until the final objective is achieved. The generic process linking the research problem and the objective is shown in *Figure 52.*

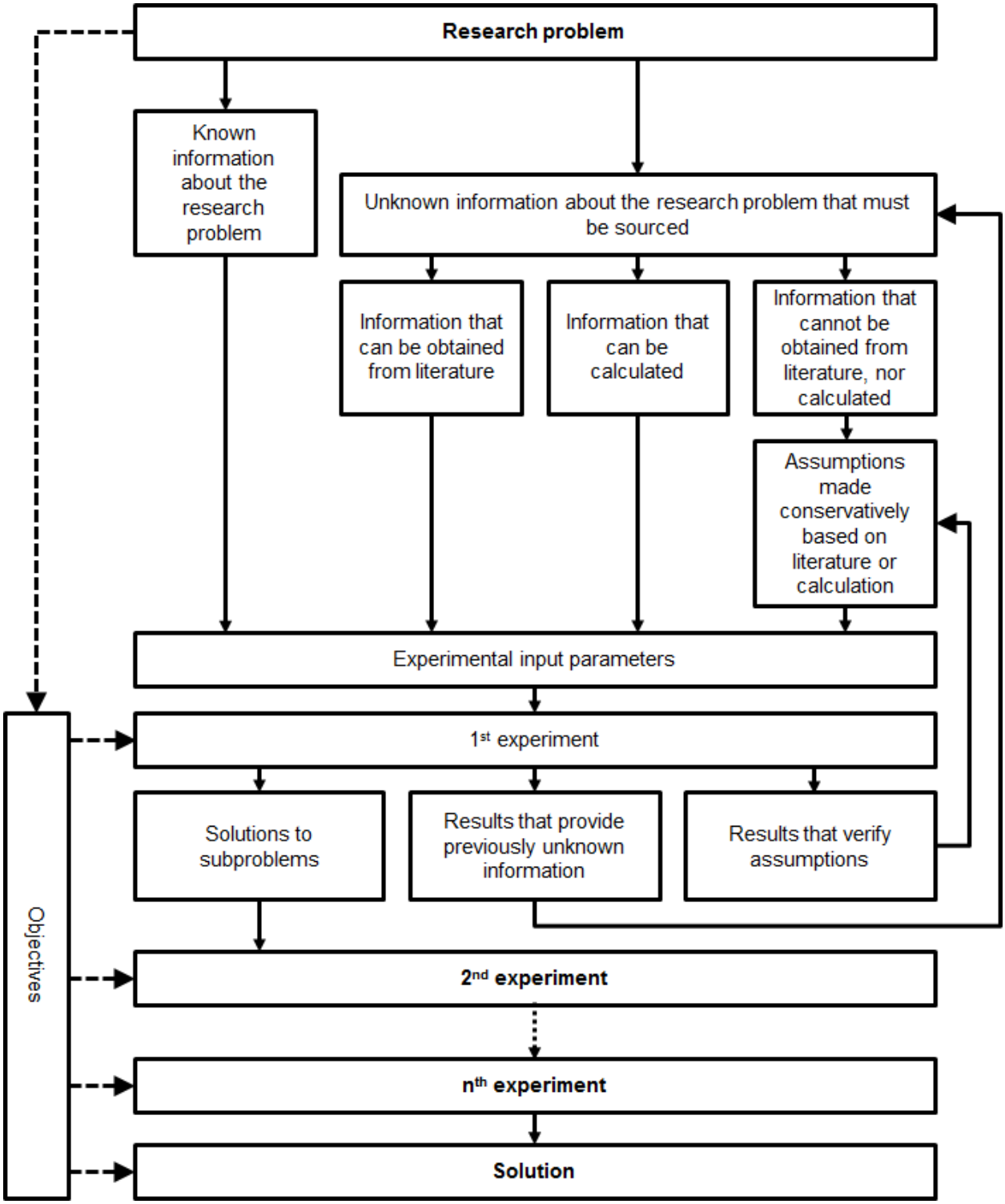

Figure 52: Generic logical framework for the JS1 crashworthiness study.

Evaluation of Information

Each objective in the study represents a major phase or experiment in the research design. The known and unknown information required to achieve each objective, and their sources, are discussed in each subsection. Note that each objective is given a concise name for reference in subsequent paragraphs:

Objective:	**Objective name:**
Determine numerically the crash response of the JS1 with loading direction as specified in CS-22.561(b)(2).	Initial crash response
Use the obtained data to determine the crashworthiness of the cockpit.	Initial crashworthiness
Formulate and implement structural improvements based on the initial results.	Improved structure
Determine the new crash responses of various enhanced structures under the same conditions as the initial test.	New crash response
Use the obtained data of the new structures to determine their comparative crashworthiness.	New crashworthiness

Initial Crash Response

In order to determine the initial crashworthiness of the JS1, the following information is required:

Required information:	**Source:**
A numerical method for crash simulation	Literature
Fuselage geometry for finite element mesh	Patran database fuseMod1_hook_fusechange.db
Fuselage laminate properties	Patran database fuseMod1_hook_fusechange.db
Material properties	Composite material test report NW-M-001

Aircraft gross weight	JS1 technical specifications
Impact angle	EASA CS22.561
Impact velocity	Adapted from static load in EASA CS22.561
Fuselage integrity under dynamic crash load	Finite element simulation
Crash acceleration response	Finite element simulation

Initial Crashworthiness

Required information:	**Source:**
Crash acceleration response	Initial crash response
Energy absorption	Initial crash response

Structural Improvement

Required information:	**Source:**
Original finite element model	Initial crashworthiness
Structural changes to improve integrity of the safety cell	Literature
Structural changes to improve crash energy absorption	Literature

New Crash Response

Required information:	**Source:**
Finite element model of the enhanced structure	Structural improvement
Fuselage integrity under dynamic crash load	Finite element simulation
Crash acceleration response	Finite element simulation

Initial Crashworthiness

Required information:	**Source:**
Crash acceleration response	New crash response
Energy absorption	New crash response

Experimental design

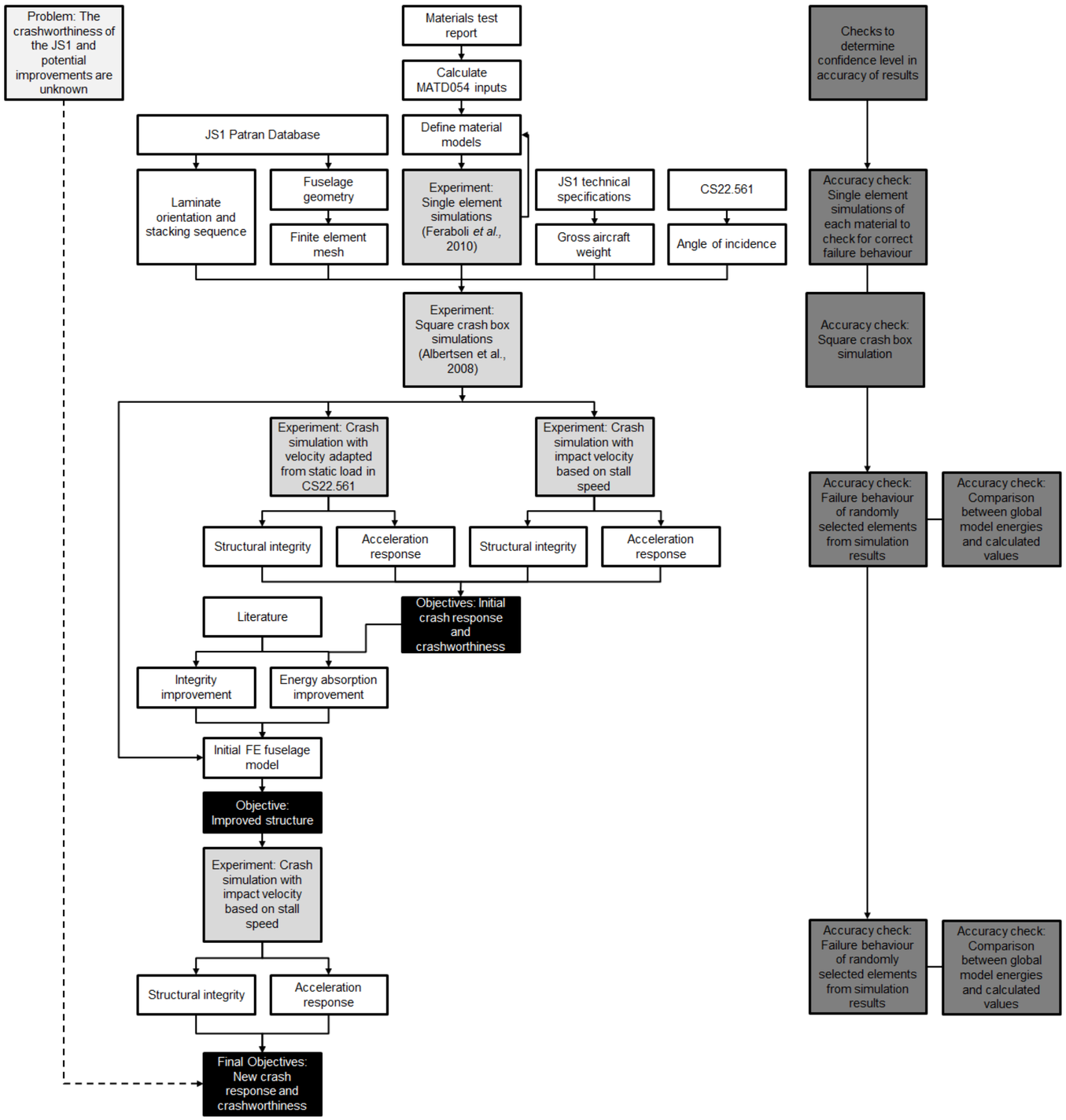

Figure 53: Flow diagram of research design.

Appendix B: Details of the NC11 Finite Element Model

The progressive development of the NC11 model started from IC1, which was the finite element model of the existing structure of the JS1. Changes included all modifications done in stages NC2, NC3, NC4, NC5, NC6, NC8, NC10 and some unique changes that were applied only to NC11. The locations of modified components are shown in *Figure 54.* Note that parts 1822, 1823 and 1825 are not shown due to their small size. Details of the modifications applied in each of the stages are given in subsequent paragraphs.

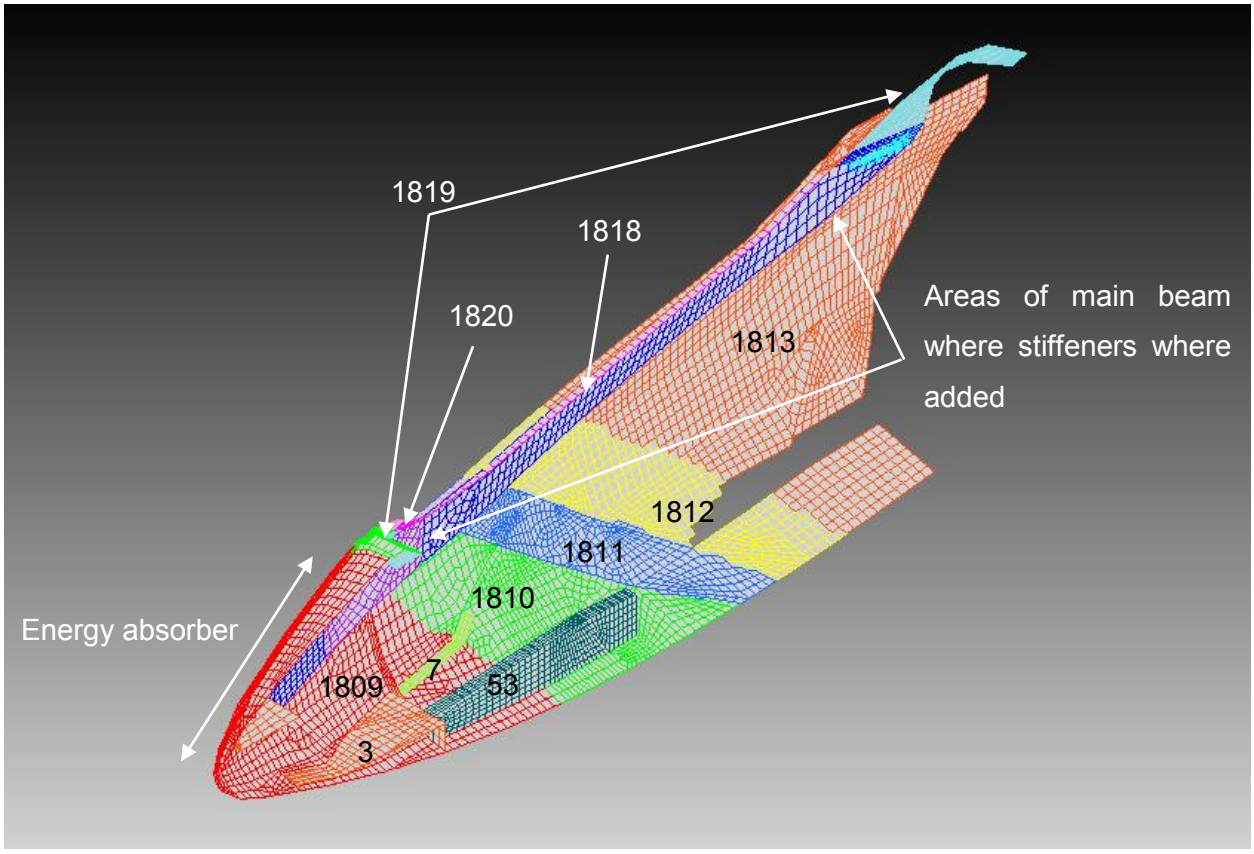

Figure 54: **Section view of the JS1 cockpit showing parts that were modified to improve crashworthiness.**

NC2

A 7 mm layer of 3-dimensional brick elements were applied to the outside of part 1809. A PSOLIDD property was applied to the brick elements with a MATD063 material model based on Hexcel 1/8-5052-0.003. The composite lay-up of part 1809 was duplicated and applied to the outside of the brick elements to form a sandwich configuration. Contact between all layers was modelled using glued contact with option JGLUE set to option 6.

NC3

Table 14 is a summary of all changes made to laminae in NC3.

Part	Layer number	Material ID	Thickness increase [mm]
1810	1	GUD	0.5
1810	2	GBID	0.5
1810	3	CUD	0.5
1810	4	GBID	0.5
1810	5	AUD	0.7
1810	6	GBID	0.5
1810	7	ABID	0.7
1811	1	GUD	0.5
1811	2	GBID	0.5
1811	3	CUD	0.25
1811	4	AUD	0.7
1811	5	AUD	0.7
1811	6	CUD	0.25
1811	7	ABID	0.7
1819	4	ABID	2
1820	5	ABID	6
1822	1	GUD	0.5
1822	2	GBID	0.5
1822	3	CUD	1
1822	4	AUD	0.7
1822	5	AUD	0.7
1822	6	CUD	1
1822	7	ABID	0.7
1822	8	GBID	2.7
1822	9	GBID	0.2
1822	10	ABID	0.3
1822	11	CUD	1.2
1822	12	CUD	0.8
1822	13	ABID	0.6
1823	1	GUD	0.5
1823	2	GBID	0.5
1823	3	CUD	0.8
1823	4	AUD	0.7
1823	5	AUD	0.7
1823	6	CUD	0.8
1823	7	ABID	0.7

Table 14: Summary of changes made to laminae in NC3.

NC4

In NC4 the honeycomb material model was changed from Hexcel 1/8-5052-.003 to 1/8-5052-.002. The following changes were made to laminates.

Part	Layer number	Material ID	Thickness increase [mm]
1812	1	GUD	0.5
1812	2	GBID	0.5
1812	3	CUD	0.25
1812	4	AUD	0.7
1812	5	AUD	0.7
1812	6	AUD	0.7
1812	7	CUD	0.25
1812	8	ABID	0.6
1813	1	GUD	0.5
1813	2	CBID	1
1813	3	CUD	0.25
1813	4	AUD	0.7
1813	5	AUD	0.7
1813	6	AUD	0.7
1813	7	AUD	0.7
1813	8	CUD	0.25
1813	9	ABID	0.7
1821	1	ABID	0.7
1821	2	CUD	1.8
1821	3	ABID	0.7
1821	4	CUD	1.8
1821	5	ABID	0.7

Table 15: Summary of changes made to laminae in NC4.

NC5

Two layers of GBID with a thickness of 0.25 mm were removed from part 1809.

NC6

In NC6, the honeycomb material model was changed to Hexcel® 1/8-5052-.0007.

NC8

The honeycomb material model was changed to Hexcel® 1/8-5052-.001. A beam stiffener consisting of two layers of CUD [0°/45°] with a thickness of 1 mm each was attached to the

main longitudinal beam. It was used to stiffen the beam at the interface between the cockpit and the fuselage. Other changes to laminae are summarised in *Table 16.*

Part	Layer number	Material ID	Thickness increase [mm]
1810	2	CBID	1
1813	4	CBID	1

Table 16: Summary of changes made to laminae in NC8.

NC10

Two new layers of CBID were added to parts 1818 and 1820. The thickness of layers 1, 2 and 3 in the outer skin of the energy absorber were increased to 0.75 mm, 0.75 mm and 1 mm respectively. A 0.25 mm layer of CBID was added to the same component.

NC11

In part 3, two GBID layers with thicknesses of 0.3 mm were substituted with 0.6 mm CBID layers. In part 7 one GBID layer with a thickness of 0.3 mm was substituted with a 0.6 mm CBID layer. A beam stiffener, similar to the stiffener described in NC8, was applied to the main longitudinal beam at the interface between the energy absorber and the cockpit. Other modifications to laminae are shown in *Table 17.*

Part	Layer number	Material ID	Thickness increase [mm]
53	1	GBID	0.2
53	2	ABID	0.35
53	3	ABID	0.35
53	4	GBID	0.2
1825	1	CBID	0.3
1825	2	CUD	0.6
1825	3	CBID	0.3

Table 17: Summary of changes made to laminae in NC11.